Dissertation

submitted to the

Combined Faculties of the Natural Sciences and Mathematics

of the Ruperto-Carola-University of Heidelberg, Germany

for the degree of

Doctor of Natural Sciences

Put forward by

Leo Pöttinger

born in Freiburg im Breisgau, Germany

Oral examination: Heidelberg, 15th January 2014

Spectroscopic characterization of dye sensitized TiO_2 with CO_2 co-adsorption and visible light excitation

Referees:

Prof. Dr. Thomas Bürgi

Department of Physical Chemistry, University of Geneva

Prof. Dr. Annemarie Pucci

Department of Physics, University of Heidelberg

Spektroskopische Charakterisierung von farbstoffsensibilisertem TiO_2 mit CO_2 Co-adsorption und Lichtbestrahlung im sichtbaren Bereich

Der Reduktionsprozess von Kohlenstoffdioxid (CO_2) zu Kohlenwasserstoffen ist ein aussichtsreicher Weg hin zu Kraftstoffen aus regenerativer Energie. Die grundlegenden Prozesse und Anforderungen des Reduktionsprozesses werden an einem neuen Katalysatorsystem aufgezeigt. Der Katalysator besteht aus organischen Molekülen auf Titandioxid-(TiO_2)-Nanopartikeln, die im sichtbaren Wellenlängenbereich absorbieren. Die angeregten Elektronen im Farbstoff werden zum TiO_2 transferiert, wo sie den Reduktionsprozess einleiten. Die Anbindung der Farbstoffe spielt deshalb eine besondere Rolle für die Elektroneninjektion und deren Stabilität auf dem Katalysator. Drei verschiedenen Ankergruppen wurden verglichen. Farbstoffe mit Carbonsäureanker und Hydroxamsäureanker formen bidentate Chelate, wohingegen die Anhydridankergruppe über zwei verbrückte Bidentate koordiniert. Das führt zu einer durchschnittlichen Belegungsdichte von $3.8{\cdot}10^{-18}\,\mathrm{m}^2$ pro Anhydridanker-Farbstoffmolekül gegenüber $1.9{\cdot}10^{-18}\,\mathrm{m}^2$ pro Carbonsäure- oder Hydroxamsäure-Farbstoffmolekül. Das Anhydrid unterliegt dem größten Strukturwechsel bei der Adsorption, woraus sich eine Absorptionswellenlängenänderung von $\emptyset\Delta\lambda_{\mathrm{anhydride}} = -80\,\mathrm{nm}$ ergibt und damit die stabilste Anbindung. Die höchsten Photoströme wurden für den Farbstoff mit Hyroxamsäureanker gemessen.

Die in-situ ATR-IR-Spektroskopie von CO_2-gesättigtem Wasser auf dem farbstoffsensibilisierten TiO_2 zeigt eine verminderte Carbonatadsorption mit veränderter Koordination gegenüber unbelegtem TiO_2 aber keine Verdrängung der angebundenen Farbstoffe. Die Imprägnierung von TiO_2-Nanopartikeln mit Metallcokatalysatoren beeinflusst die Carbonatkoordination nicht. Insgesamt ist die Stabilität und Elektroneninjektion von Farbstoff zu TiO_2 vielversprechend, trotzdem sind die adsorbierten Carbonate demgegenüber chemisch stabil.

Spectroscopic characterization of dye sensitized TiO_2 with CO_2 co-adsorption and visible light excitation

The carbon dioxide (CO_2) reduction to hydrocarbons is a promising route to renewable fuels. Mechanistic studies on a new catalyst for visible light absorption and CO_2 conversion reveal the structural and chemical challenges of the CO_2 reduction. Organic dyes are bound to Titania (TiO_2) nanoparticles for visible light absorption. The excited electrons are transferred to the catalyst where they provide energy for the catalytic process. The coordination and coverage of three selected anchoring groups reveals the efficiency of electron injection into the TiO_2 and their stability on the catalyst. Dyes with carboxylic acid and hydroxamic acid anchors bind via a bidentate chelating coordination, whereas dyes with an anhydride group mostly bind in a two bidentate bridging coordinated pattern. This leads to an average surface occupancy of $3.8{\cdot}10^{-18}\,\mathrm{m}^2$ per anhydride dye molecule and $1.9{\cdot}10^{-18}\,\mathrm{m}^2$ per carboxylic or hydroxamic acid dye molecules. The anhydride anchor shows the

biggest structural change which leads to the highest observed hypsochromic shift upon adsorption of $\varnothing\Delta\lambda_{\mathrm{anhydride}} = -80\,\mathrm{nm}$ and is most stable when adsorbed. The highest electron injection efficiency is observed for the dye with a hydroxamic acid anchoring group.

The in-situ ATR IR spectroscopy of CO_2 saturated water adsorbed on dye sensitized TiO_2 shows a reduced carbonate formation with different adsorption coordination compared to pure TiO_2, but no displacement of preadsorbed dyes. The addition of metal co-catalysts on TiO_2 does not influence the carbonate coordination. The photon absorption and electron injection show promising results, whereas the carbonates are still chemically stable.

Table of Contents

Symbols and Abbreviations

ϵ	extinction coefficient
$\lambda_{\mathrm{DUG11x}}$	Bandpass filter for UV
λ_{GG435}	Cutoff filter below 435 nm
Θ	Incident angle
Θ_{c}	Critical angle
c	Speed of light constant
E_{gap}	Band gap energy
h	Planck constant
K	reaction constant
k_{H}	Henry constant
$k_{\mathrm{H}}^{\ominus}$	Henry constant at standard temperatur (298 K)
N_0	Quantity of dye molecules
N_{1-3}	Quantity of not adsorbed dye molecules
n_1, n_2	refractive indices
p	pressure
AFM	Atomic Force Microscopy
ATR	Attenuated total reflection
DSSC	Dye sensitized solar cell
BET	Brunauer–Emmett–Teller
$\mathrm{C_H}$	Henry coefficient
CB	Conduction band

EDX	Energy dispersive X-ray spectroscopy
FID	Flame ionization detector
HOMO	highest occupied molecular orbital
IR	infra red
IRE	Internal reflection element
LUMO	lowest unoccupied molecular orbital
SE2	Secondary electron detector
SEM	Scanning electron microscopy
SFG	Sum frequency generation
TCD	Thermal conductivity detector
THF	Tetrahydrofuran
THF	Tetrahydrofuran
UV	ultraviolet
VB	Valence band
XPS	X-ray photoelectron spectroscopy

1 Introduction

1.1 Motivation

The increase of greenhouse gases carbon dioxide (CO_2), nitrous oxide (N_2O) and methane (CH_4) in the atmosphere from fossil fuel combustion will lead to a global temperature warming due to back scattering of earth´s thermal radiation [1]. The consequences differ regionally and are summarized by the Intergovernmental Panel on Climate Change (IPCC). Ecological changes like rising sea level, melting glaciers, extreme weather, floods and droughts have negative economic and political impact [2]. The reduction of greenhouse gas emissions is implemented by various conventions, including the United Nations Framework Convention on Climate Change. The tools include emissions trading, energy efficiency, energy savings and implementation of renewable energy sources. One of the greatest technological challenges is the storage and transportation of the fluctuating nature of wind and solar energy. There is a considerable interest in large scale electrolysis of water to create hydrogen (H_2) which is a high density energy carrier (electrochemical power-to-gas). Due to handling issues a further reduction with CO_2 to methane via water-gas shift reaction and Fischer-Tropsch process is considered [3]. Alternative routes without the intermediate step losses of electricity or hydrogen generation are thermochemical and photocatalytic reduction of CO_2 to hydrocarbons [4]. The present work presents first in-situ infrared (IR) spectroscopic studies on the photocatalytic properties of new designed dye sensitized and metal impregnated TiO_2catalyst.

1.2 Photocatalytic CO_2 reduction

Photo-generated catalysis combines light harvesting agents, electron and hole splitting and catalytic active material. In 1872, FUJISHIMA and HONDA discovered the photocatalytic reaction of water splitting with ultraviolet (UV) illuminated TiO_2 in aqueous suspension [5]. Surface processes of UV irradiated TiO_2 are summarized by LINSEBIGLER, LU and YATES [6]. The first photocatalytic CO_2 reduction to hydrocarbons and the proposed reaction mechanism came from INOUE and co-workers in 1978 [7].

So far, various systems have been investigated to reach high order hydrocarbons with sunlight optimized absorption. Heterogeneous systems with semiconductors like TiO_2, ZnO, ZrO_2, CdS, Fe_2O_3, WO_3, GaP and SiC modified with doping, impregnation, dye sensitization and enzyme attachment were considered. Another field of research are homogeneous systems based solely on transition metal complexes[8].

Due to advances in the stability of dye sensitized solar cells, including dyes resistant to acidic environment [9, 10] and the promising work of OZCAN [11] and NGUJEN [12] in the field of dye sensitized TiO_2 photocatalysis the BASF SE initiated the Solar2Fuel project with university collaborations within the Leading-Edge Cluster *Forum Organic Electronics*.

1.3 Solar2Fuel project: Dye sensitized TiO_2 with metal co-catalyst

The aim of the project was the photocatalytic conversion of CO_2 to hydrocarbons over dye sensitized and metal impregnated TiO_2 nanoparticles. Project partners are BASF SE - Division of Dyes for Electronics for materials, Energie Baden-Württemberg (EnBW) AG in collaboration with Forschungszentrum Jülich for CO_2 sequestration and economic analysis, Karlsruhe Institute of Technology - BOCKHORN group for reactor design, Ludwig Maximilian University of Munich (LMU) - SCHMIDT-MENDE group for test reactor and University of Heidelberg - BÜRGI group and working team GRUNZE subdivided by KOELSCH and ZHARNIKOV for mechanistic studies.

The mechanistic studies presented in this work are designed to bridge fundamental research on model systems with real reaction conditions. In-situ attenuated total reflection (ATR) infrared (IR) spectroscopy is combined with gas chromatography for the analysis of surface reactions. Further surface characterization methods employed are scanning electron microscopy (SEM), atomic force microscopy (AFM) for structural analysis and photometry (UV/VIS spectroscopy) for the determination of electronic transitions.

The obtained results are complemented by ex-situ infrared, Raman and in-situ sum-frequency generation (SFG) spectroscopy measurements by Anna Keese on the same samples. They determine binding modes, binding kinetics and coordination of the dyes in more detail.

Furthermore, the interpretation of results is extended by X-ray photoelectron spectroscopy (XPS) for the oxidation states of the TiO_2 and metal co-catalysts and the photocurrents showing the driving force of electrons into the TiO_2 acquired by Florian Staier. The objectives and analytic approach of this work are defined in the following section.

1.4 Central questions and research methods

The anchoring groups determine the **stability and efficiency of the photoconversion process**. Therefore a set of dyes with distinct anchoring groups are bound to TiO_2 to correlate the binding coordination and photon absorption frequency with the existing results of photocurrent measurements by Florian Staier.

Binding modes are determined by in-situ by ATR IR spectroscopy measurements. The results are complemented by Raman and SFG spectroscopy on the same catalyst provided by Anna Keese. The coverage of dye molecules on TiO_2 surface is measured by UV/VIS absorption in a suspenstion experiment.

The stability of **CO_2 co-adsorbed on dye sensitized TiO_2 with metal impregnation in aqueous environment** determines the catalyst viability under reaction condition. Adsorbed CO_2 is considered as the first reaction step of the catalytic reduction. The adsorption coordination of CO_2, its stability and influence on the adsorbed dye mimic the real reaction conditions.

Model surfaces of dye sensitized metal impregnated TiO_2 nanoparticles are prepared by spin coating and analyzed by in-situ ATR IR spectroscopy in a flow through cell for solvents.

Irradiation of CO_2 co-adsorbed on the catalyst in aqueous environment with visible light. The influence of absorbed light by the photocatalyst onto co-adsorbed species and possible reaction products is measured by ATR IR spectroscopy combined with gas chromatography.

1.5 Thesis outline

Chapter 2 shows the current state of research in the fields of dye adsorption of dye sensitized solar cells and their charge separation concept as well as photocatalytic CO_2 reduction on various heterogeneous catalysts. The basic concepts are explained with a focus on the mechanistic and spectroscopic analysis necessary for the interpretation of acquired data.

Chapter 3 describes the used raw materials, preparation processes and research methods with detailed parameter explanation. The physical principles underlying methods and their application in this work is shown.

Chapter 4 starts with a characterization of the prepared samples followed by ex-situ dye adsorption experiments. A set of dyes is selected to show adsorption coordination and kinetics of different anchor groups followed by an interpretation and correlation to photoconversion efficiency. Spectroscopic analysis of CO_2 (co)-adsorption on TiO_2 and visible light catalyst excitation are presented.

Chapter 5 summarizes the conclusions drawn from the results, brings them in perspective of expectations and offers suggestions for future works.

2 Theoretical background

The basis of photocatalysis is photoabsorption, exciton generation, charge separation and surface reactions. This chapter contains the fundamental mechanisms of charge generation in dye sensitized solar cells as it is used in this work and bridges the gap to CO_2 reduction photocatalysis on TiO_2. The dye sensitization as well as the CO_2 reduction needs a fundamental understanding of the sorption processes at the TiO_2 surface. Therefore the current state of research of the binding configurations of the dye anchoring moieties on TiO_2 is discussed with focus on their spectroscopic analysis. Furthermore, the mechanisms of co-adsorption of CO_2 in aqueous solution on the dye sensitized TiO_2 and the possible photochemical reaction pathways upon visible light excitation are shown.

2.1 Dye sensitized TiO_2

The following chapter shows the basic function of a dye sensitized TiO_2 solar cell (DSSC) . It covers the initial step of photoabsorption and charge separation. The efficiency of this process is an important feature of dye sensitized solar cells. The same photoabsorption concept is used in this work, therefore the working principle of a DSSC is shown in the following sections.

2.1.1 Concept of dye sensitized solar cells

The first prototype of dye sensitized solar cells was published by GRÄTZEL and O´REGAN in 1991 [13]. The new concept of energy conversion from electromagnetic waves to electric current is based on the charge transfer of an excited dye electron to TiO_2 particle film on a transparent conducting anode. The cathode provides electrons to the dyes via a redox mediator. The maximum voltage is the difference between the Fermi level of the TiO_2 conduction band and the redox potential of the mediator. Figure 2.1 shows a scheme and a picture of a self assembled dye sensitized solar cell. Light is absorbed by a dye bound to the TiO_2 and an electron is excited from ground state S to S*. The electron is transferred to the conduction band of the TiO_2 where it propagates to the anode. The dye is regenerated by a redox system e.g. I_{3^-}/I^-. The output voltage is the energy difference of redox and TiO_2 conduction band potential (Figure 2.1).

The efficiency furthermore depends on various parameters as highest occupied molecular orbital (HOMO) and lowest unoccupied molecular orbital (LUMO) level of the dye, dye coverage and dye anchor moiety [14] which are discussed in the following sections.

2.1.2 Electron and hole separation

Conventional metal oxide semiconductor solar cells separate the excited electrons and holes (excitons) by a high inner electric field due to a doping of the semiconductor. In contrast the charge separation of electrons and holes in DSSCs is achieved by pushing the excited electron to the anchoring moiety of the dye and with a HOMO level S* higher than the conduction band energy E_{CB} of the TiO_2 particle (Figure 2.1). The electron is injected into the conduction band of the TiO_2. The spacial separation of the charges leads to a slow recombination rate and a lifetime of micro seconds [14] compared to piko seconds in pure semiconductor material [15].

Important parameters when selecting or developing new dyes are the tuning of HOMO and LUMO levels, enhancing the stability and varying the visible light absorption frequency. The aim is to increase interfacial electron transfer between the dye and semiconductor.

2.2 Surface structure of TiO_2

The main studies are performed on TiO_2 P25 nanoparticles [16]. Whenever reasonable studies on the TiO_2 P25 nanoparticles are complemented with TiO_2 B1 (smaller grain size) or TiO_2 P25 with metal impregnation to draw consistent conclusions. The material composition and characterization can be found in Section 3.4 and 4.1. The TiO_2 P25 surface structure is the starting point for catalytic reactions. The material has suitable valence band (VB) and conduction band (CB) potentials for CO_2 reduction and water oxidation and is chemically stable, non-toxic and inexpensive [17]. The rutile and anatase structures are Ti^{4+} surrounded by six O^{2-} atoms forming an octahedron [18]. The octahedron structures are linked differently for those pure modifications leading to different physical and chemical properties. Rutile has a band gap of 3.0 eV and anatase 3.2 eV. The anatase modification exhibits a lower surface energy compared to the rutile and brookite modification (thermal transformation above 700 °C).

The most stable crystal surface for anatase is the (110) plane and for rutile the (101) plane and should therefore be predominant in TiO_2 P25 nanoparticles. In UHV conditions the surface exhibits highly reactive undercoordinated Ti_{5c} facets (in Figure 2.2 the Ti connected to non bridging oxygen) and oxygen vacancies. The addition of water leads to a hydration layer on the Ti_{5c} sites and hydroxylated O_{2c}

sites [19]. These terminal hydroxyls are the main adsorption sites for carboxylic acid anchoring groups [20]

At ambient conditions the surface is partially hydroxylated. In contrast to the rutile(100) the anatase(101) surface adsorbs water non dissociative. This adsorbed water has slightly different properties than bulk water [21].

2.3 Adsorption kinetics and mechanisms

Photocatalysis bridges a gap between light absorption e.g. a semiconductor and using the absorbed energy in a catalytic process. Reactant adsorption on the catalyst is usually the first step in a catalytic reaction. In this work TiO_2 nanoparticles are used and the reactants are in liquid phase. This is by definition a heterogeneous catalytic process. The first part of this work addresses the dye adsorption on TiO_2 from organic solvents. The second part studies the co-adsorption of CO_2 on TiO_2 in aqueous solvent. An ATR IR flow through cell is used to do spectroscopy on the surface during the adsorption process. Therefore the adsorption experiments contain adsorption of the solvent on the catalyst (as reference spectrum) followed by addition of the adsorptive to the solvent. This leads to an exchange of adsorbed solvent with the adsorbate depending on the adsorptive concentration.

The concentration dependence of adsorbate on the adsorptive is described by isotherms. Linear isotherms describe the sorption of gases in solvents, where there is no competition in adsorption sites (Henry´s Law). Exponential isotherms include the fact that adsorption sites exist and a higher consumption of these sites leads to a decrease in loading (Freundlich isotherm). When the maximum loading is set to a monolayer or the complete consumption of surface sites, the Langmuir isotherm (Eq.: 2.1) is the best description. Additionally an increase of adsorbate higher than the first monolayer to form multiple layers is described by the BET isotherm.

To simulate the dye adsorption from liquid phase in a porous TiO_2 structure a Langmuir adsorption model was used by WOELZL [23]. The Langmuir model was extended to diffusion of adsorbate into the porous material because of its thickness (10 µm). The porous surfaces used in this work are only 350 nm thick where diffusion effect is two orders of magnitude lower. The coverage θ is defined as covered adsorption sites divided by the total amount of adsorption sites. With the equilibrium reaction constant K and the partial pressure p the equilibrium coverage can be determined to:

$$\theta = \frac{K \cdot p}{1 + K \cdot p} \,. \tag{2.1}$$

The equilibrium coverage is independent of the reaction mechanism. In all dye adsorption experiments the adsorptive concentration is kept constant (0.5 mmol/L).

The ex-situ experiments and in-situ spectroscopic measurements give comparable information about the coverage (for the initial concentration), adsorption coordination and reaction rates. All experiments contain a purging cycle with pure solvent. In a complete reversible adsorption reaction all adsorbed dye would desorb. If the first monolayer is chemisorbed and additional layers are physisorbed different reaction speeds must also be visible in the in-situ IR measurements. If the chemisorbed species are strongly bound it can lead to an irreversible adsorption.

2.4 Dye adsorption on TiO_2

The most efficient sensitizing structures used in DSSCs are perovskite pigments with to 14.1 % of energy conversion efficiency [24]. The search for suitable metal free (low cost) dye structures showed a huge variety of accessible structures like perylene, coumarin, porphyrin, cyanin and merocyanine dyes [25].

The dyes themselves are usually divided in an anchoring group, a body, an electron donor group and a tail or side group as shown in Figure 2.3. In this work the anchoring mechanism and performance of two different types of dyes (triphenylamine-perylene and carbazole-rhodanine) with two different anchoring groups each is investigated. The dyes used in this work are shown in Figure 2.4. Two Rhodanine dyes with either carboxylic acid anchoring group (SF2) or hydroxamic acid anchoring group (SF3) and two perylene dyes with anhydride anchoring group (SF5) or carboxylic anchoring group (SF15) are composed from a wide range of dyes and provided by the BASF SE.

The perylene dyes exhibit a high molar extinction coefficient [26] and its modifications are widely employed in industry [27]. The carbazole-rhodanine dyes are donor acceptor dyes with shorter absorption wavelength and higher HOMO and LUMO levels compared to the perylene dyes (see Section 3.4.2).

Starting from a well known and highly efficient carboxylic anchoring group two modified anchoring groups were synthesized by BASF SE in respect to favor stability for the ambient reaction environment.

The proposed anchoring mechanism of the different anchoring groups is shown in the following sections with the focus on their spectroscopic analysis.

2.4.1 Carboxylic acid anchoring group

The search for higher photoconversion rates of DSSCs and efficient charge injection lead to an increasing interest in the binding configuration of the dyes. The first highly efficient ruthenium dyes contained carboxylic anchoring groups. To study the adsorption surface or interface sensitive techniques as IR, Raman [28], PES and NEXAFS [29] were reported.

The carboxylic acid forms bonds with the surface hydroxyl groups (see Fig: 2.5). The adsorption type is either via covalent bonding or hydrogen bonding. For the covalent bonding ester-type bidentate carboxylate to one (chelating) or two (bridging) surface-Ti [30, 31] is possible. For the hydrogen bonding either one or two hydrogen bonds are possible.

Depending on the dye structure different binding modes are possible [32]. A summary for ruthenium based dyes can be found e.g. in [33]. The typical IR bands of monodetate ester-type ν(C=O) are at 1720 cm^{-1} - 1750 cm^{-1}, bidentate carboxylate $\nu_{as}(CO_2^-)$ at 1550 cm^{-1} to 1750 cm^{-1} and $\nu_s(CO_2^-)$ at 1350 cm^{-1} to 1450 cm^{-1}. The chelating and bridging coordination are distinguished empirical by the difference of the frequencies of the adsorbed species compared to their salts (bridging coordination when $\triangle\nu_{ads} \leq \triangle\nu_{salt}$ and chelating when $\triangle\nu_{ads} \ll \triangle\nu_{salt}$) [34].

The surface hydroxyl groups (ν(-OH) 3500 cm^{-1} - 3800 cm^{-1}) are consumed by the dissociative binding configuration and stable for the hydrogen bonding configuration [35][36].

2.4.2 Anhydride anchoring group

The implementation of an anhydride anchoring group is based on the idea of a more stable anchoring and a higher LUMO electron density in the vicinity of the TiO_2 to enhance electron injection into the TiO_2. The most recent literature describes the anchoring process via carboxylate formation by a surface hydroxyl attacking the C-O single bond [36]. The process is shown schematically in Figure 2.6. Another indication for this structural change during adsorption is the color shift upon lowering the effective conjugation length of the molecule (blue shift of adsorption frequency) [37].

After the formation of one carboxylate bond there is a carboxylic acid left which could form another bond (dissociative or non-dissociative). The complexity of this two step reaction in combination with complex dye structures makes if difficult for ex-situ spectroscopic coordination determination. Therefore model substances like maleic acid [38, 39] and naphtalic anhydride and its cleaved form were reported with ATR IR and Raman spectroscopy. The ν_s(C=O) anhydride at 1769 cm^{-1} and ν_{as}(C=O) anhydride at 1734 cm^{-1}react to surface bound carboxylate bands at $\nu_s(CO_2^-)$ 1350 cm^{-1} and $\nu_{as}(CO_2^-)$ 1551 cm^{-1}. With the same empirical rule by DEACON et al. determined the binding coordination is most likely in bridging coordination [33].

2.4.3 Hydroxamic acid anchoring group

Hydroxamic acids act as metal ion capturing in many biological systems [40]. Their adsorption strength towards metal oxides was investigated by FOLKERS et al. for self assembled monolayers (SAM) [41]. They found a higher affinity of hydroxamic acid towards TiO_2 than carboxylic acid. Infra red spectroscopic studies of aceto-hydroxamic acid adsorption on Geothite ($Fe^{3+}O(OH)$) was performed by HOLMEN et al. [42] showing a chelating adsorption via the two oxygen atoms and stability in aqueous solvents. Infrared spectroscopic studies of acetohydroxamic acid, N-methylformohydroxamicacid, N-methylacetohydroxamicacid, and 1-hydroxy-2-piperidone acids on TiO_2 were performed by YANG et al. [10]. They observed and calculated the vibrational modes and concluded a binding via hydroxamate ions which form bidentate surface complexes. Figure: 2.7 shows a schematic representation of the proposed binding coordination.

The interfacial electron transfer was studied with far IR spectroscopy by MCNAMARA et al. showing similar electron transfer times as carboxylic anchors [9]. The improved performance of hydroxamic acids compared to phosponate and carboxylic anchoring groups for DSSCs by BREWSTER et al. was shown for a metal complex dye [43].

2.5 CO_2 adsorption at TiO_2 water interface

The initial step of a catalytic process is the interaction between catalyst and reactant. The here investigated catalysts, the modified TiO_2, is mixed with CO_2 saturated water. The CO_2 saturation leads to a variety of species and is discussed in the following section. The coordination of these species adsorbed on TiO_2 and modified TiO_2 is discussed subsequently.

2.5.1 CO_2 in water

The concentration of carbon dioxide dissolved in water is described by Henry´s law. At given temperature T the concentration c is determined by $c(T) = p/k_{\mathrm{H}}(T)$ where k_{H} is the temperature dependent Henrys constant and p the partial pressure of the gas. This constant is calculated from two empirical values $k_{\mathrm{H}}^{\ominus} = 3.4 \cdot 10^{-2}\,\mathrm{mol/(L \cdot atm)}$ and $C_{\mathrm{H}} = 2400$ for CO_2 in water by $k_{\mathrm{H}}(T) = k_{\mathrm{H}}^{\ominus} \exp(C_{\mathrm{H}}(1/T) - (1/T^{\ominus}))$.

The saturation was performed under atmospheric pressure of 99.9995 % CO_2 at 35 °C. The elevated temperature is chosen to prevent unwanted degassing in the flow through cell during the experiments. The solubility of CO_2 reduced to $2.6 \cdot 10^{-2}$ mol/L which is 77 % of the concentration at $T^{\ominus} = 25\,°\mathrm{C}$.

The addition of CO_2 to water leads to a chemical equilibrium with carbonic acid (Eq.: 2.2) depending on the temperature. The hydration constant of H_2CO_3/CO_2 is $1.7 \cdot 10^{-3}$ at 25 °C and insignificantly temperature dependent [44]. This results in a total concentration of $5 \cdot 10^{-5}$mol/L carbonic acid.

$$\mathrm{CO_2 + H_2O \rightleftharpoons H_2CO_3} \tag{2.2}$$

$$\mathrm{H_2CO_3 \rightleftharpoons HC}O_3^- + H_3\mathrm{O}^+ \tag{2.3}$$

$$HCO_3^- \rightleftharpoons CO_3^{2-} + H_3O^+ \tag{2.4}$$

Further dissociation to bicarbonate (HCO_3-) and carbonate (CO_3^{2-}) with oxonium ions (H_3O^+) is shown by a change of pH value (Eq.: 2.3 and 2.4). The pH of the used MilliQ water is measured pH(MilliQ) = 6 and of the CO_2 saturated water at 35 °C pH(CO_2,H_2O, 35 °C) = 4.5. The difference of the pH shows the concentration of oxonium as well: $c_{H_3O^+} = (10^{-4.5}) - (10^{-6}) = 3 \cdot 10^{-5}$. The Hägg diagram of CO_2 in water shows the bicarbonate/carbonic acid ratio at pH = 4.5 is 10^{-3} ($c_{\text{bicarb.}} = 5 \cdot 10^{-8}$ mol/L in total) and carbonate/carbonic acid ratio of 10^{-7}($c_{\text{carb.}} = 5 \cdot 10^{-13}$ mol/L in total) [45].

2.5.2 CO$_2$ and H$_2$O adsorption on TiO$_2$

The binding configurations of CO_2 on TiO_2 in the presence of H_2O are reported in a mixed gas phase only. The proposed binding coordination of CO_2 on TiO_2 include bridging, bidentate, monodentate and free carbonate (CO_3^{2-}) as shown in Figure 2.8. The corresponding IR bands taken from literature are summarized in Table: 2.1. In the presence of water Baltruaitis et. al. could show a decrease of bicarbonate species but an increase in carbonic acid species [46].

Similar to the dye adsorption described in the previous sections the adsorption of carbonates is consuming surface hydroxyl groups [48]. The spectral range of surface hydroxyl groups are 3500 cm^{-1} to 3800 cm^{-1}. This leads to the question weather the consumption of surface hydroxyl of preadsorbed dye competes with the adsorption of carbonates on the surface.

2.6 Photochemical reduction of CO$_2$ on TiO$_2$

The first proposed reaction mechanism of photocatalytic CO_2 reduction to hydrocarbons with TiO_2 catalyst suspension was introduced by INUE et. al. 1979 [7]. The proposed mechanism is an excitation of electrons in the conduction band of the TiO_2 and electron vacancy in the valence band (h+). At the surface H_2O is oxidized and dissociated to O_2 and H^+. The electrons can reduce the adsorbed CO_2 in a multistep process to hydrocarbons (Eq.: 2.5-2.10). But in the same process H_2O can be reduced to $^\bullet$OH radicals which are highly reactive and known for decomposition of organic compounds [6, 15, 49].

To use this process in terms of an environmental application of CO_2 capturing and processing using renewable energy several approaches were developed [4].Three elemental functions of such a photocatalyst are: Photoabsorption, electron hole splitting (with metal electron traps) and active catalyst surface. In this project

TiO_2 nanoparticles with metal impregnation (Pd, Pt, Cu) were used. For the photoabsorption in the visible range dyes are bound to the catalyst surface.

An important part of this work is the adsorption of the organic dyes used to shift the absorption wavelength of photocatalyst to the visible range. The goal is to maximize the absorbed photons of the solar spectrum. An energy scheme determining the nescessary reduction energy is shown in Figure 2.9: Equations 2.5-2.10 show the multiple electron transfer process necessary to reduce CO_2 and their reduction potential versus normal hydrogen electrode (NHE, pH = 0, at 25 °C) [50].

$$\mathrm{CO_2 + e^- \rightarrow CO_2^{\bullet -}} \qquad \mathrm{E^0 = -1.90\,V} \tag{2.5}$$

$$\mathrm{CO_2 + 2\,H^+ + 2\ e^- \rightarrow HCOOH} \qquad \mathrm{E^0 = -0.61\,V} \tag{2.6}$$

$$\mathrm{CO_2 + 2\,H^+ + 2\ e^- \rightarrow CO{+}H_2O} \qquad \mathrm{E^0 = -0.53\,V} \tag{2.7}$$

$$\mathrm{CO_2 + 4\,H^+ + 4\ e^- \rightarrow HCHO{+}H_2O} \qquad \mathrm{E^0 = -0.48\,V} \tag{2.8}$$

$$\mathrm{CO_2 + 6\,H^+ + 6\ e^- \rightarrow CH_3OH{+}H_2O} \qquad \mathrm{E^0{=}\text{-}0.38\,V} \tag{2.9}$$

$$\mathrm{CO_2 + 8\,H^+ + 8\ e^- \rightarrow CH_4{+}2\ H_2O} \qquad \mathrm{E^0 = -0.24\,V} \tag{2.10}$$

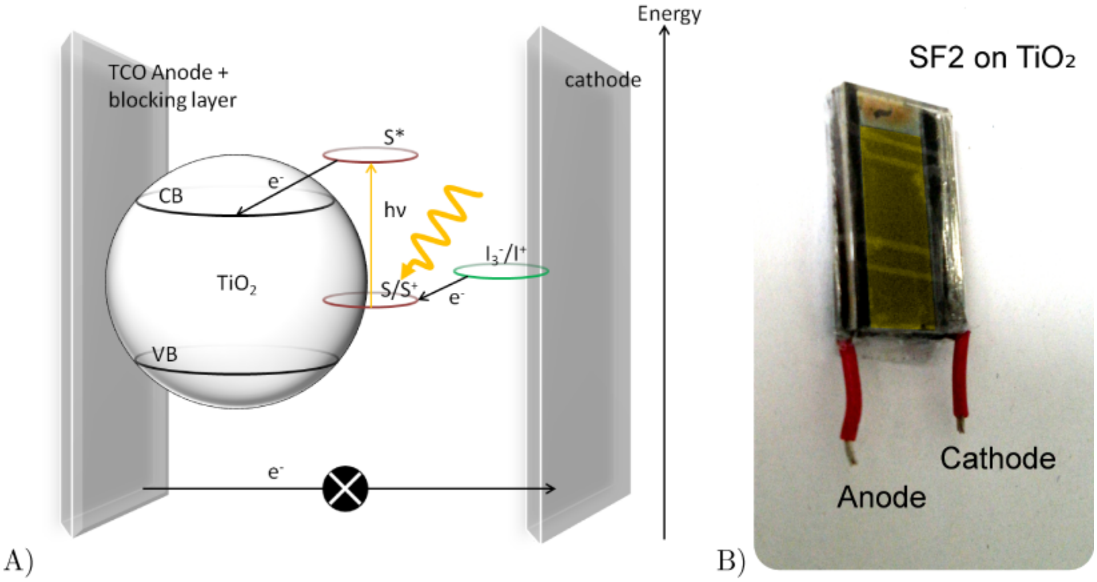

Figure 2.1: Comparison of A) Operation scheme of a DSSC and B) self-made test sample of a DSSC with 350 mV output voltage (Dyesol TiO_2 and dye SF2 and I^-/I_3^- electrolyte). A closed layer of TiO_2 is sputtered on the anode glass (blocking layer) to prevent a short circuit.

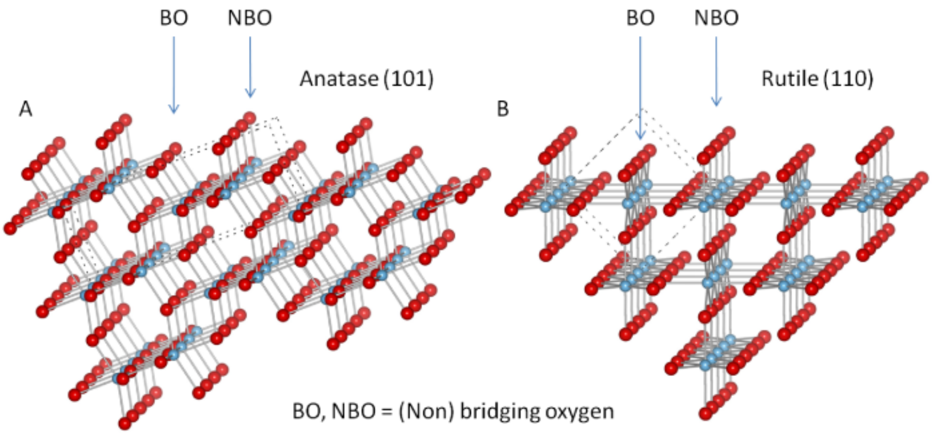

Figure 2.2: Ball-and-stick models of the (A) anatase(101) and (B) rutile(110) crystal faces. Blue colored balls represent Titanium atoms, the red ones are oxygen atoms. The sketch is drawn with VESTSA[22]. Dotted lines show a unit cell.

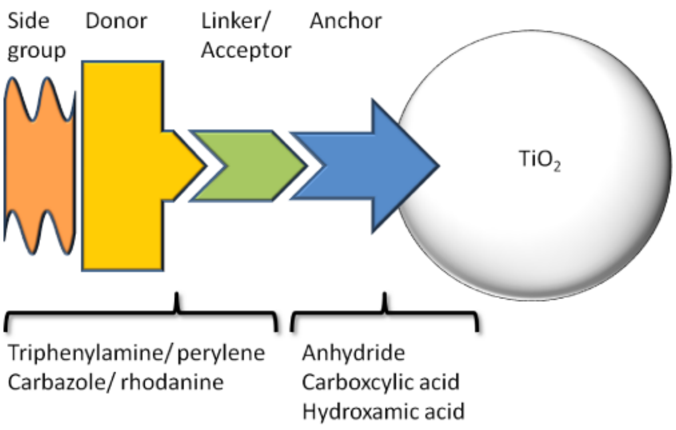

Figure 2.3: Scheme of donor acceptor dye structures. A donor acceptor mechanism enforces charge separation and a high electron drive towards the anchoring moiety and determines the absorption frequency. Attached side groups can influence solubility and wetting properties. Two classes of dyes are investigated in this work: Triphenylamine perylene and carbazol/rhodanine dyes. The aim is the correlation between the binding mechanism of different anchoring groups (anhydride, carboxylic acid and hydroxamic acid) with chemical stability, coverage and electron transfer.

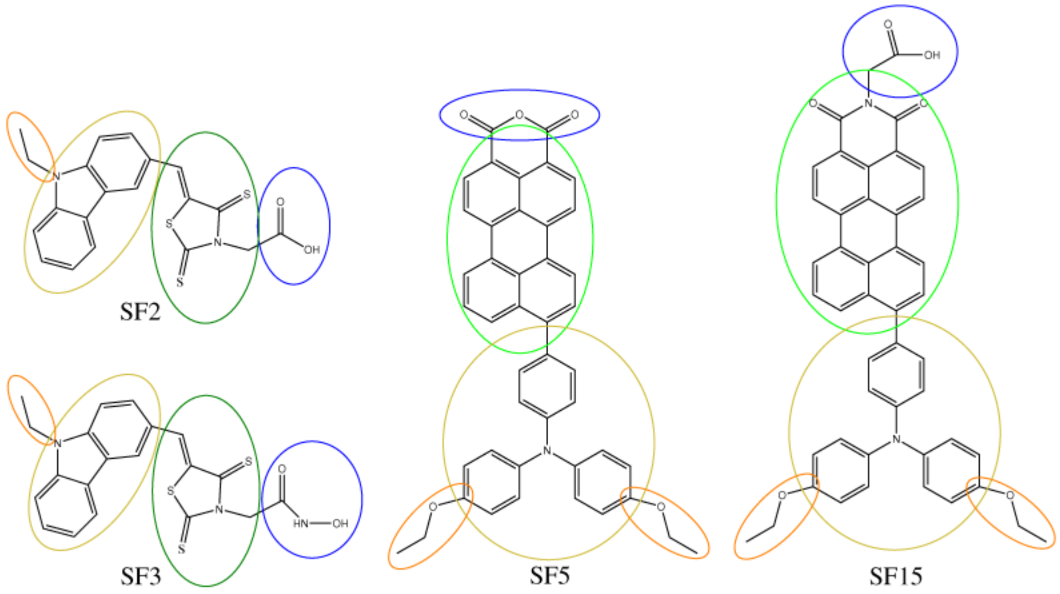

Figure 2.4: Chemical structure of the dyes for TiO$_2$ sensitization. SF2 and SF3 are carbazole/ rhodanine dyes with carboxylic acid and hydroxamic acid anchoring group respectively. SF5 and SF15 are triphenylamine/ perylene dyes with anhydride and carboxylic acid anchoring group, respectively. The anchoring moiety is highlighted blue, donor and acceptor in yellow and green and the tail group in orange.

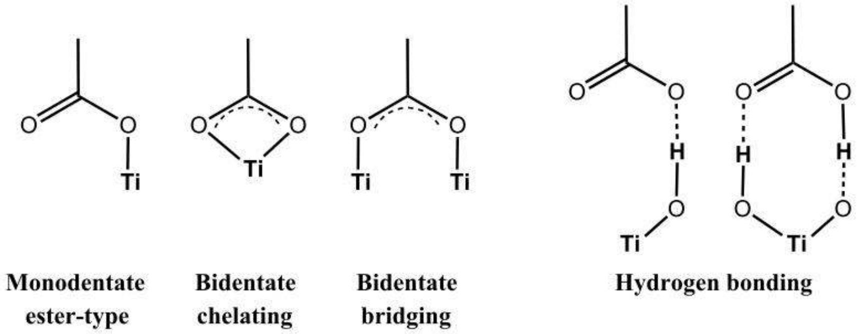

Figure 2.5: Binding modes of carboxylic acid via ester, carboxylate or hydrogen bonding.

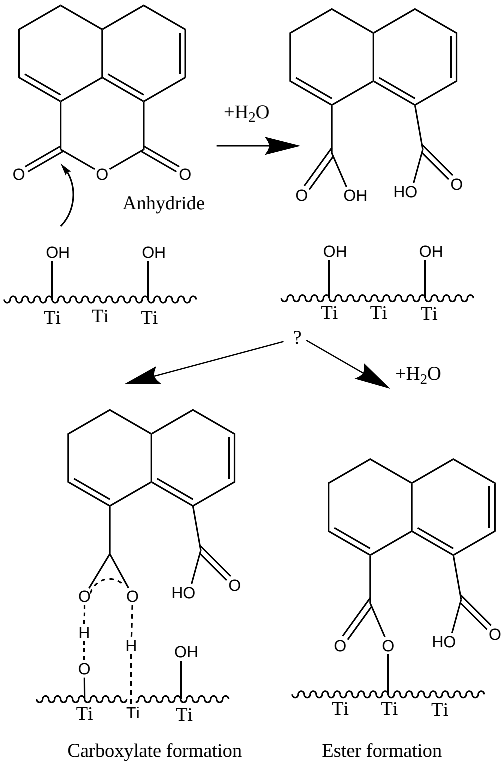

Figure 2.6: Scheme of the possible binding coordination of anhydride. The surface hydroxyl groups attacks the anhydride group are causing a ring opening. The acid groups can form either a carboxylate or an esther type coordination.

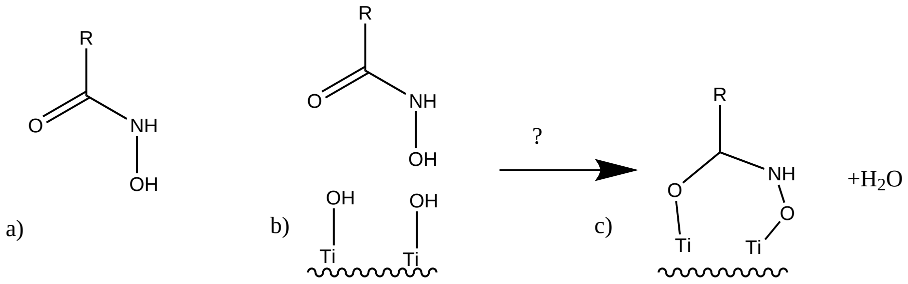

Figure 2.7: Possible binding coordination of a hydroxam anchor taken from[10]. The OH group of the hydroxamic acid shown in scheme a) reacts with hydroxyl groups of the TiO_2 surface in scheme b) to a bidentate chelating coordination upon H_2O release in c).

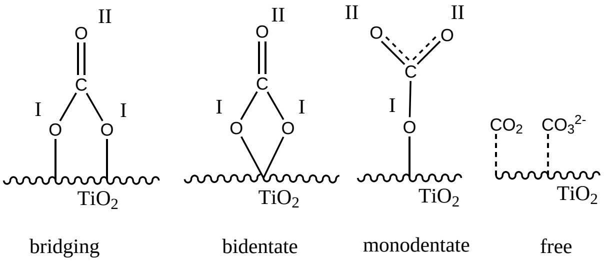

Figure 2.8: Binding coordination of CO_2 on TiO_2 surface.

Table 2.1: Vibrational frequencies of CO_2 on TiO_2 nanoparticles taken from [47].

Coordination	**Wavenumber [cm^{-1}]**
	TiO_2
Bridging $\nu(CO_{II})$	1725
Bidentate $\nu_{as}(CO_IO_I)$	1330
$\nu(CO_{II})$	1560
Monodentate $\nu_s(CO_{II}O_{II})$	1370
$\nu_{as}(CO_{II}O_{II})$	1465
Free CO_3^{2-}	1454
CO_2 molecular dissolved	2343

Legend: ν, stretching; s, symmetric; as, asymmetric;

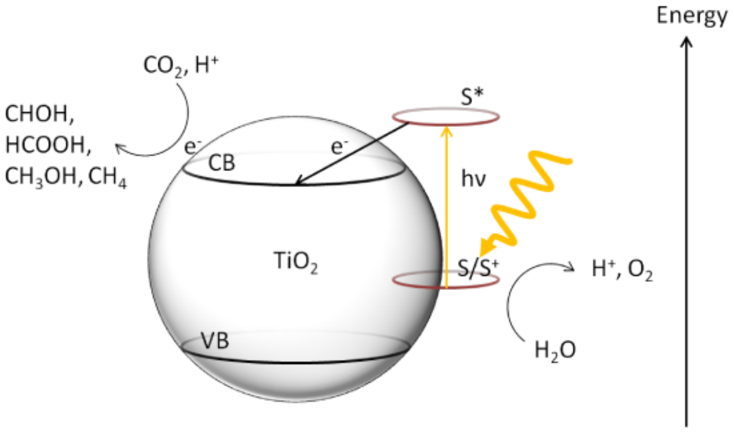

Figure 2.9: Energy scheme of photocatalytic CO_2 reduction with a lower band gap due to dye adsorption (red).

3 Materials & Methods

This chapter shows the experimental setup, the work principle and the physical principles of the used devices. Figure 3.1 gives an schematic overview of the used devices and setups. The main device is a FT-IR spectrometer with an ATR flow through cell including a quartz window for in-situ irradiation experiments. This flow through cell is purged with solvents by a peristaltic pump from a temperature stabilized reservoir. The outlet or analyte can be analyzed by gas chromatography. The dye binding is additionaly investigated with two photometry techniques.

Furthermore, this chapter contains basic information of the raw materials and prepared samples. Morphological information are gained by microscopy techniques, whereas structural and kinetic information is deduced from various spectroscopy methods.

3.1 Surface microscopy

The morphology and elementary anaysis of the TiO_2 nanoparticles is analysed by scanning electron microscopy with energy dispersive X-ray spectroscopy (EDX). For the determination of the perpared nanoparticle films atomic force microscopy is used. The techniques are explained in the following sections.

3.1.1 Atomic force and scanning electron microscopy

The atomic force microscopy is a type of scanning probe microscopy in which the Van der Waals force between a scanning tip and the sample is utilized. In this work the tapping mode is used. The tip is forced to oscillate while scanning close to the surface. The frequency of the oscillation and the tip height over the surface are in a feedback loop. When the oscillating tip is approaching the surface the utmost atoms interact due to induced dipole interaction. A slight change in oscillating frequency is detected. The feedback system regulates the detected frequency back to the exciting frequency by regulating the distance from the surface. The tip follows the surface morphology and the motion is plotted.

A Digital Instruments Dimension 3100 AFM was used with an electronic damping system and Nanoscope 5.30r2 software for evaluation.

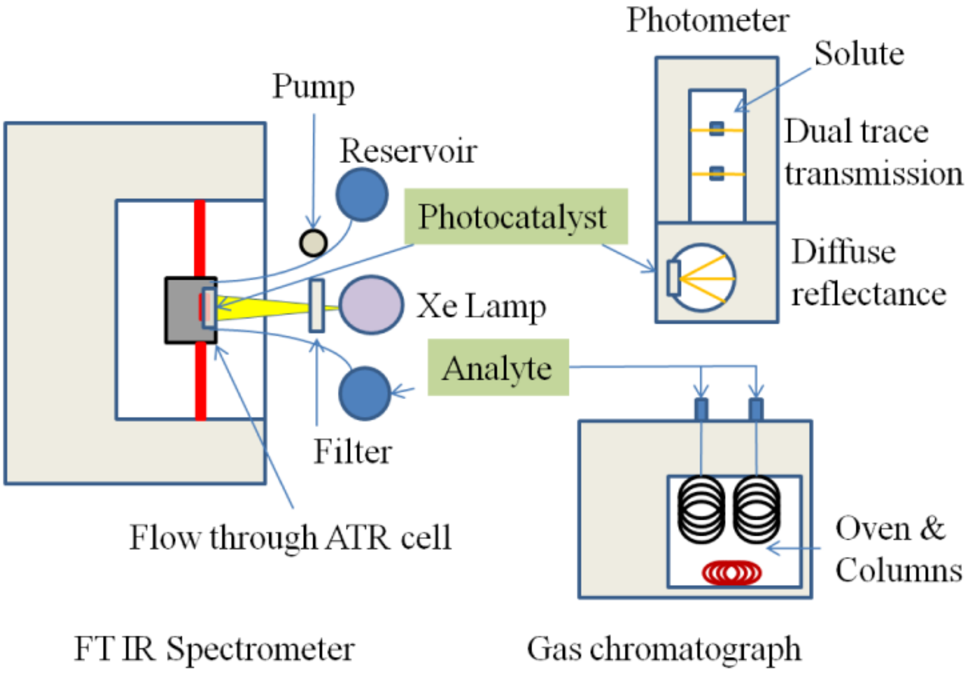

Figure 3.1: Schematic overview of the experimental setup for photocatalytic reaction measurements. The combination used is in-situ ATR IR spectroscopy and gas chromatography. The photocatalyst is characterized by a photometer and various microscopy techniques.

The scanning electron microscopy is based on electron and photon analysis upon electron-electron interaction. The incident electron beam creates secondary electrons (elastic scattering), back-scattered electrons (inelastic scattering) and x-rays. The three types of radiation are detected respectively by an in lens detector, secondary electron detector located in a tilt angle to the incident beam and a micro-calorimeter for x-rays (EDX). The secondary electrons and the characteristic x-rays are nucleus size dependent and give information about the composition. The back-scattered electrons with the tilted detector gives topographic information.

The SEM measurements in this work are performed with a Zeiss Leo 1530 electron microscope and a Zeiss Ultra 55 with EDX at Max Planck Institute for Intelligent Systems, Stuttgart in the group of PROF. DR. J. SPATZ by FERDINAND BELZ.

3.2 Surface spectroscopy

A wide range of spectroscopy techniques provide insight in the physical and chemical properties of substances. The IR spectroscopy uses the characteristic absorption of infrared radiation of molecules. The absorbed energy correspond to excited vibrations of molecules or functional groups. A chemical change of a substance (e.g. chemisorption) can therefore change the IR absorption spectra. To reveal the dynamic process of adsorption a flow through cell inset was used in a Fourier transform spectrometer. The IR spectroscopy on the catalyst was performed in attenuated total reflection geometry due the surface sensitivity and for highly absorbing materials and solvents.

The results are compared to Raman spectroscopy which is a complementary method to IR spectroscopy due to the difference in selection rules. In addition sum-frequency-generation spectroscopy is applied, a surface sensitive non-linear optical method. These measurements were performed by Anna Keese at Institute of Toxicology and Genetics at Karlsruher Institute of Technology, Germany. These methods are employed to reveal the binding meachnisms of dyes and CO_2 to the TiO_2 surface.

X-Ray photoelectron spectroscopy is performed to reveal the elemental composition of the nanoparticles, the chemical state of the metal impregnated nanoparticles and unwanted contamination. These measurements were performed by Florian Staier, Institute of Physical Chemistry, University Heidelberg, Germany.

The ultraviolet and visible light spectroscopy is used for quantitative determination of dye solutions and electronic transitions within the dyes and dye sensitized TiO_2.

3.2.1 Infrared spectroscopy

Infrared spectroscopy describes the interaction of matter with electromagnetic waves from 0.8 µm to 1000 µm wavelength or converted to wavenumbers 12500 cm^{-1} to

10 cm^{-1}. The wavelength of the absorbed wave can be detected and attributed to known molecular structures. The interaction or absorption of the far infrared excites rotation of molecules. The mid-IR excites vibrations of molecules or functional groups.

There are several models to describe the electronic potential of two atoms bound to each other. The most simple is the harmonic potential but is very limited. In 1929 PHILIP MCCORD MORSE proposed an exponential potential [51] which accounts for the dissociation energy D_e

$$V(R) = D_\mathrm{e} \cdot \left(1 - e^{-a\cdot(R-R_\mathrm{e})}\right)^2 \tag{3.1}$$

with r_e as the potential minimum radius and a the “stiffness” of the potential.

This approach still allows an analytical solution of the vibration energies E_ν of the Schrödinger equation:

$$E_\nu = h\nu_0 \cdot \left(\nu + \frac{1}{2}\right) - \frac{h^2\nu_0^2}{4D_\mathrm{e}} \cdot \left(\nu + \frac{1}{2}\right)^2 \tag{3.2}$$

with the Planck constant h and vibrational quantum number ν. Furthermore, the vibration frequency is calculated to

$$\nu_0 = \frac{a}{2\pi}\sqrt{\frac{2D_\mathrm{e}}{m}} \tag{3.3}$$

where m is the reduced mass. A graphical illustration is shown in Figure 3.2.

The most interesting spectral range for organic molecules as used in this work is the mid-IR spectral range between 4000 and 400 cm^{-1}.

The IR spectra are obtained with a Bruker IFS 66v Fourier transformation IR spectrometer operated ina 1 mbar evacuated chamber and equipped with liquid nitrogen cooled MCT detector. The spectrometer is operated with Opus 3.1 software.

3.2.2 Attenuated total reflection (ATR) spectroscopy

Attenuated total reflection is a surface sensitive spectroscopy method which can be applied to optical dense matter. It was first introduced by HARRICK and FAHRENFORT in 1960 [52]. The method is based on total reflection and evanescent waves. Total reflection occurs when the incident angle Θ is higher than the critical angle Θ_c. From Snell´s law the critical angle is derived as $\Theta_\mathrm{c} = \arcsin\left(\frac{n_2}{n_1}\right)$ with refractive indices n_1 and n_2. A scheme of the total reflection and the resulting evanescent field is shown in Figure 3.3. If the beam hits the wall of the internal reflection element

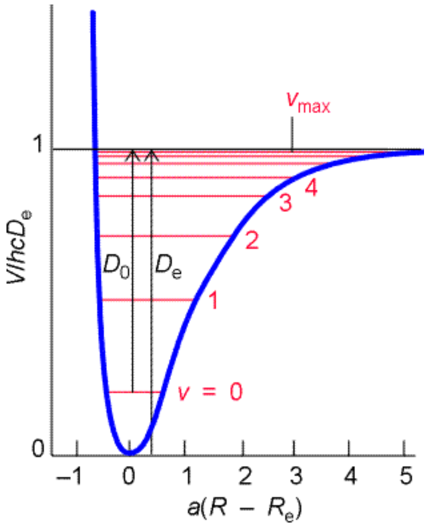

Figure 3.2: Morse potential shows the potential energy and energy levels of a diatomic molecule.

with an angle greater than the critical angle total reflection occurs. In the point of total reflection an evanescent wave is created due to the boundary condition of the electromagnetic field. If a sample is brought into the evanescent field, the reflected beam is attenuated by the probe which can be detected. The penetration depth d_p is where the amplitude of the field decreases to 1/e.

$$d_\mathrm{p} = \frac{\lambda}{2\pi\sqrt{n_1^2 \sin^2(\Theta) - n_2^2}} \tag{3.4}$$

where n_1 is the refractive index of the internal reflection element and n_2 of the sample. Θ is the angle of incidence versus the vertical axis. The refractive index of germanium is $n_\mathrm{Ge} = 4.00$ and for $\mathrm{TiO_2}$ $n_{\mathrm{TiO_2}} = 2.61$ [53]. For an estimated incident angle of $\Theta = 60°$ and a IR beam with of $400\,\mathrm{cm^{-1}} < \lambda < 4000\,\mathrm{cm^{-1}}$ the penetration depth is $170\,\mathrm{nm} < d_\mathrm{p} < 1750\,\mathrm{nm}$ which is well suited for the films prepared in this work.

Germanium reflection elements with 1 mm thickness are used. The thickness is a crucial parameter for the number of interneal reflections in the reflection element. The beam is reflected between 10 and 15 times on each side. The IRE is 5 cm in lenght and 2 cm in width.

The investigation of adsorption processes is performed with a flow through cell (Figure 3.4) with an embedded reflection element. A quartz glass with rubber sealing and holes for inlet and outlet is pressed on the reflection element.

The cell was rebuilt by Florian Wölzl for the use in reduced pressure [36].

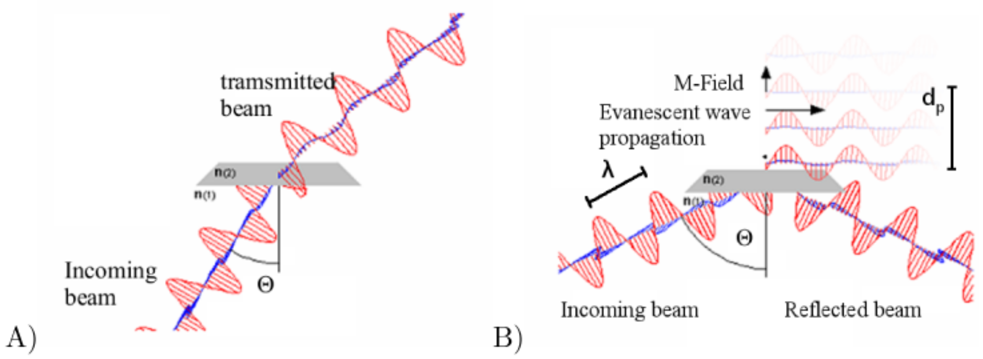

Figure 3.3: A) Diffraction of an electromagnetic wave at a phase boundary. B) For $\Theta > \Theta_c$the total reflection occurs with an exponential decaying electromagnetic field into the adjacent phase [54].

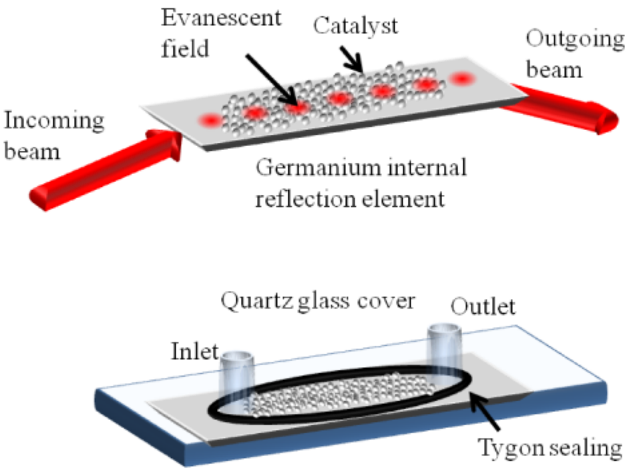

Figure 3.4: Top: Internal reflection element (IRE) with in and out going beam. The red spots represent the evanescent wave positions. Bottom: Sealing with a rubber ring and quartz glass window with inlet and outlet for flow through experiments.

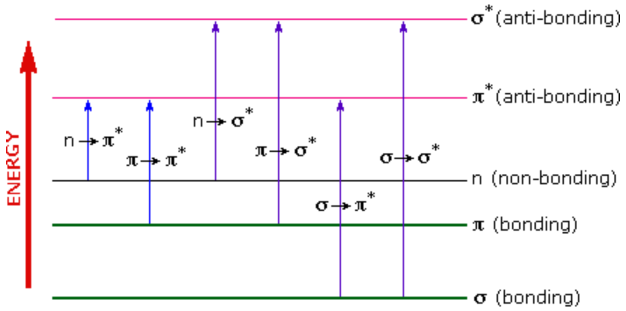

Figure 3.5: Energy diagram of electronic transitions in molecules. An electron can be excited when the incoming photon energy matches the transition energy and the excited state is empty.

3.2.3 Ultraviolet and visible light (UV/VIS) spectroscopy

The near UV and visible part of the electromagnetic spectrum is between 0.1 µm and 0.8 µm. Absorption or reflection in the visible range directly affects the perceived color of a substance. The underlying effect is electronic transitions of valence electrons to higher energy states.

The materials used in this work show UV and visible light absorption. TiO_2P25 has a band gap of $E_{\mathrm{gap}} = 3{,}14\,\mathrm{eV}$ [55] which corresponds to $\lambda = \frac{h\cdot c}{E_{\mathrm{gap}}}$=395 nm which is in the UV region. The absorption can be explained by the nearly-free electron model (NFE) proposed by Felix Bloch which uses a free electron approach in a static potential of a positive charged lattice [51].

Organic dyes are synthesized to absorb in the visible range. A model to describe the electronic states of molecules is the molecular orbital (MO) theory introduced by Friedrich, Hund and Mulliken. With this theory electron transitions of the highest occupied molecular orbital (HOMO) to the lowest unoccupied molecular orbital (LUMO) in simple molecules can be explained. The most common transitions in the near UV and visible region are from bonding π and free non-bonding electrons into $\pi*$ or $\sigma*$ orbitals (Figure 3.5).

A quantitative description of the transmitted light was stated by Johann H. Lambert and August Beer. The absorbance A is written as $A = -\log(\frac{I}{I_0}) = \epsilon \cdot c \cdot d$ where I_0 is the incident light intensity and I the transmitted intensity, ϵ the extinction coefficient (in units of L/(mol·cm)), c the concentration of absorbing species (in mol/L) and d the thickness (in cm) of the absorber.

Modern UV/VIS spectrometer consist of a light source, a grating for wavelength separation, a chopper and beam splitter for sample and reference pathway and photomultiplier with detector. A common extension for intransparent samples are reflection units and Ulbricht spheres for samples with diffuse scattered light Figure 3.6.

In this work a Jasco V-650 spectrometer with reflection unit was used for transmission

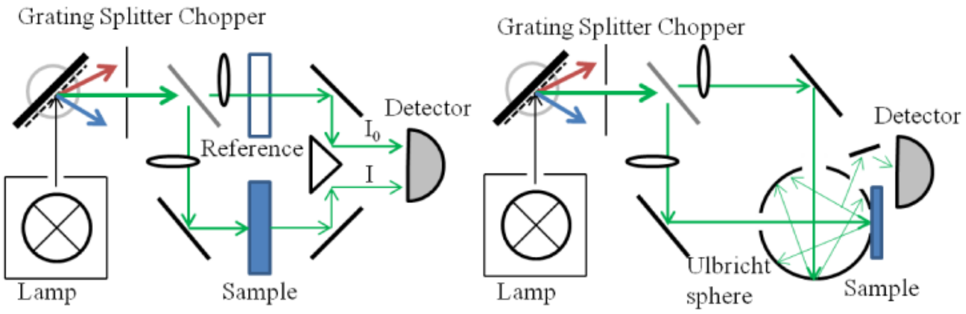

Figure 3.6: Scheme of a two beam UV/VIS spectrometer in transmission and diffuse reflection geometry.

and diffuse reflection measurements.

3.2.4 Raman, sum-frequency-generation (SFG) and X-ray photoelectron spectroscopy

In the following section a brief summary of Raman, sum-frequency-generation (SFG) and X-ray photoelectron spectroscopy is given since the results provided by the collaboration partners is frequently used.

- Raman spectroscopy uses the inelastic scattering of photons by atoms or molecules. Few photons are absorbed and re-emitted with a lower energy (Stokes scattering) and higher energy (anti-Stokes scattering). The energy difference inside scattered light corresponds to energy differences between stationary energy states e.g. vibrational or rotational states. In contrast to IR spectroscopy where a changing dipole moment is nescessary, Raman needs a change in polarizability. Thus these methods are complementary.
- In sum frequency generation spectroscopy two photons are mixed and absorbed by a molecule which emits a photon of the sum of the frequencies. Usually one of the incoming beam frequencies is in the visible range and the other is tunable in the infrared (for vibrational spectroscopy). The sum frequency is in the UV range which has several advantages. High field strength lead to a high dislocation of the electrons of the atom. The relation between electric field and polarization becomes non-linear. Only if this second order susceptibility exists in a sample, two photons can be absorbed simultaneously. This is the case on phase boundaries such as surfaces. SFG can therefore be used as a surface sensitive vibrational spectroscopy technique.
- X-ray photoelectron spectroscopy (XPS) is based on the photoelectric effect. When light with a higher energy than the binding energy of an electron is absorbed it is excited and gains enough energy to leave the atom. It is

accelerated (with a known energy) towards a detector, which measures the kinetic energy of the electron. The difference of the incident photon energy and the kinetic energy must be the binding energy of the electron. An atom specific pattern of binding energies can be measured and quantified. Also small energy deviations of the different electrons like spin-orbit coupling or chemical state can be observed.

3.3 Gas chromatography

For the quantitative analysis of samples in gas or liquid phase gas chromatography is used. With its high sensitivity it is possible to detect low concentrations of an analyte. The method uses the difference in polarity and vapor pressure to separate the analytes. If the analyte is not in the gas phase it is evaporated in an injector and mixed with a carrier gas which is pressed through a column and interacts with its packing material. The column material is selected to change the speed at which different molecules pass the column. The molecules are now split by spatially in the stream and can be detected one at a time. The absolute time of a type of molecules is called retention time. Standard flame ionization detectors (FID) and thermal conductivity detectors (TCD) for hydrocarbons are used for the respective columns. The detector signal is acquired over time which gives a peak for each type of molecule and is proportional to the concentration of the analyte. Via calibration the absolute concentration can be determined.

The setup scheme is shown in Figure 3.7. The temperature set points and carrier pressures are described in the following section.

- The H_2 channel uses Argon as carrier gas. The injector temperature is 150 °C and the column oven is at a fixed temperature of 50°C. A Hayesep Q (Divinylbenzene) 1m 1/8" is removing the moisture which can damage the molsieve and is set to retain all components slower than oxygen. A Molsieve 5A (pore size 5 Angstrom) 1m 1/8" separates different molecules by their size. The thermal conductivity detector is set to 200 °C.
- For the CO_2 channel Helium is used as a carrier gas and the injector is set to 150 °C and a back flush cycle is installed to remove moisture (Hayesep R 80-100 2,6 m). Between minute 3 and 8 the oven temperature changes constantly from 40 to 100 °C to desorb all analytes from the column material (Haysep R 80-100 1 m, Divinylbenzene and 4-vinyl-pyridine). Since the flame ionization detectors (FID) have the best sensitivity towards hydrocarbons, the remaining analytes as CO and CO_2 are hydrogenated via a copper catalyst (methanation). The FID ionizes the methanized analytes and the amount of emerging electrons is detected.
- The methanol (CH_3OH) channel carrier gas is Helium and uses a split injector. The split injection is used for liquid samples which create a high vapor volume

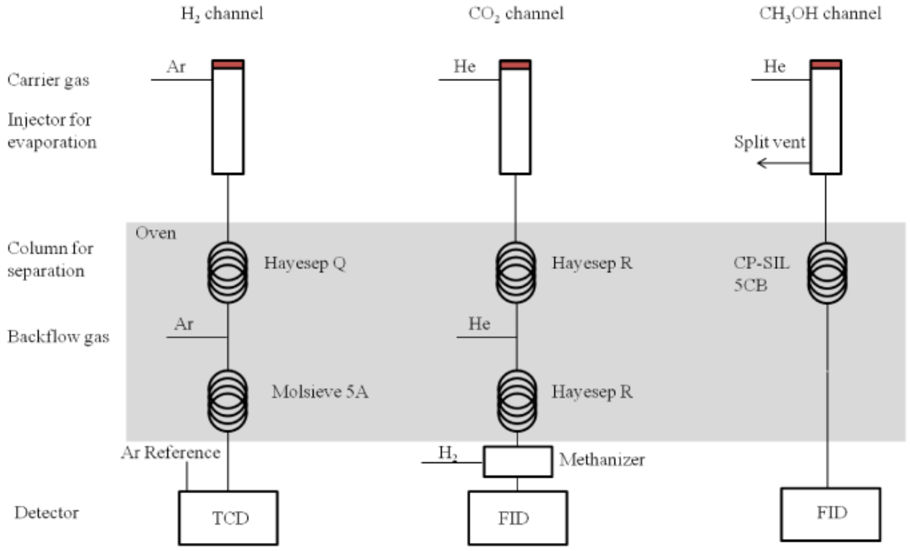

Figure 3.7: Setup scheme of the gas chromatography for hydrogen, carbon monoxide, carbon dioxide and hydrocarbons detection from water saturated gas phase or liquid phase on three different channels.

upon vaporization. To limit the pressure wave only a fraction of the evaporated sample is put on the column, the rest splits to a vent. For gases the injector temperature is set to 80 °C for liquid injection 150 °C. The CP-SIL 5CB column (60 m x 0.32 mm) is sensitive towards hydrocarbons and run up to 210 °C. The result is a separation of methanol, ethanol and formic acid.

The acquisition and evaluation of the data is performed on a Bruker GC-450 with Galaxy Chromatography Data System 1.9 software.

3.4 Materials

In this section a summary of properties of the used materials is presented. The BASF SE provided TiO_2 nanoparticles in different sizes (commercially available by EVONIK) and added co-catalysts by an impregnation method as well as selected and modified organic dyes. The analysis of these materials in their pure form is a basic need for an understanding of physical and chemical processes involving these materials.

3.4.1 TiO_2 nanoparticles and metal impregnated TiO_2 P25

The choice of the semiconductor and metal co-catalysts presented in this section is based on catalytic activity reported in literature on TiO_2 photocatalysis and is

Figure 3.8: TiO_2 nanoparticles: A) EVONIK P25 B) “B1” similar to P25 with smaller particle size. With metal impregnation in weight %: C) 0.1 % Pd D) 0.5 % Cu E) 0.1 % Pt F) 1 % Pt.

Method	Analyte	P25	B1
Elementary analysis	Ti	58,5%	54.5%
	C	0.025%	0.096%
	Cl	0.012%	0.0002%
	S	$< 0.01\%$	0.084%
BET	surface in [m^2/g]	55	333
XRD	particle size [nm]	23.5 (anatase), 31 (rutile)	7.5
composition		anatase 80 %, rutile 20 %	anatas 100 %

Table 3.1: Analysis of chemical composition, particle size and surface area of the pure TiO_2 nanoparticles[56].

described in chapter 2. Figure 3.8 shows a picture of the provided nanoparticles.

The specifications of P25 can be found in Reference [16]. Analysis of chemical composition, particle size and surface area of the pure TiO_2 nanoparticles was performed at BASF SE. The results are shown in table 3.1:

The TiO_2 supported Pt nanoparticles were prepared using the incipient wetness impregnation method. P25 was used as TiO_2, H_2PtCl_6 was used as Pt precursor. In a typical preparation, certain amount of H_2PtCl_6 aqueous solution corresponding to the pore volume of the support was added to TiO_2 powder under stirring. Afterwards the mixture was dried at 80 °C overnight followed by calcination at 400 °C for 3 hours in air [57] . The same procedure was repeated with Pd and Cu.

3.4.2 Organic dyes

Section 2.4 has already shown the classification and structure of the four selected dyes for binding mode identification. All dyes used in this work are an alternation of

Table 3.2: Functional groups of the investigated organic dyes.

Dye	Anchor	Body	Donor	Side group
SF1	Anhydrid	Perylene	Diphenylamine	TMB
SF2	Carboxyl	Rhodanine	Diphenylamine	None
SF3	Hydroxam	Rhodanine	Carbazole	None
SF4	Anhydrid	Perylene	Diphenylamine	TMB
SF5	Anhydrid	Perylene	Triphenylamine	PEG
SF15	Carboxyl	Perylene	Triphenylamine	PEG
SF16	Anhydrid	Perylene	Diphenylamine	PEG
SF17	Anhydrid	Perylene	Diphenylamine	PEG
SF18	Carboxyl	Perylene	Diphenylamine	PEG

Legend: TMB, 1,1,4,4-Tetramethylbutyl group; PEG, Polyethylene glycol.

Figure 3.9: Powder samples of the provided dyes (from left to right SF1-SF5 and SF15-SF18). The structural formulas can be found in Figure 3.10.

anchor, donor and acceptor functionalities. This enables the analysis and evaluation of one functionality but within their complex structure. The solid powder forms are shown in Figure 3.9 and their structural formulas with a picture of dyes in solution in Figure 3.10. The functional groups are summarized in Table 3.2. The side groups are used for solubility of the unbound dyes and for the wetting of the bound dyes. The tetramethylbutyl side group enables an good solubility in solvents and is water repelling when adsorbed. The polyethylene glycol leads to a weak solubility in water (a lot of agglomerations observed) and a is hydrophilic.

The intramolecular charge transfer in perylene dye SF2 (publication name ID28) is shown by Edvinsson et al. [37].

Again, for the analysis of the influence of the anchoring groups a comparison of SF5 with SF15 and SF2 with SF3 is used since they only differ in their anchoring moiety.

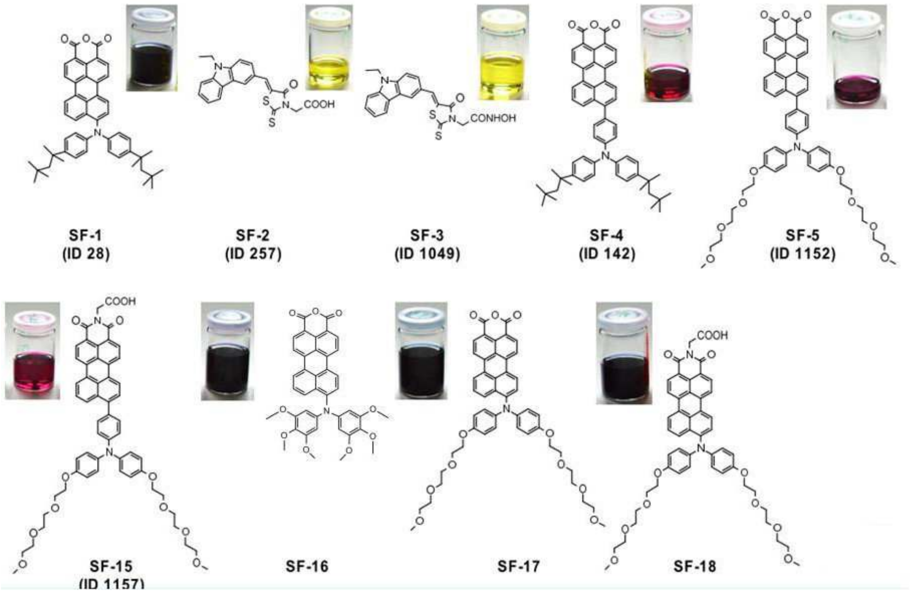

Figure 3.10: Structural formula and pictures of dye solutions in tetrahydrofuran (THF). Pictures were taken by Florian Staier.

3.4.3 Gases and solvents

Pure gases and gas mixtures were purchased from AIR Liquide. The N_2 and CO_2 are of 99.995 % purity. Purified water is produced in a Millipore device. This so called MilliQ water is filtered through a 0.22 µm membrane and is deionized to a resistivity above 18 MΩ·cm [58]. The pH value is measured regularly and in the range of 5 to 6.

3.5 Sample preparation

A surface measured in ATR geometry with IR spectroscopy needs to have certain properties as described in Section 3.2.2. These properties include sample thickness because of the beams penetration depth, film stability upon purging solvents and cleaning of starting material. To fulfill these requirements a routine of sonification, heating and spin coating of catalyst suspensions onto the ATR substrate was developed.

For visible light spectroscopy samples (thick layers) and gas chromatography samples (reactants in catalyst suspensions), a series of centrifugations and sonifications was used and is described in the following section.

All TiO_2 catalyst powders were pretreated by heating up to 300 °C to remove organic contamination. Before mixing with solvents they were cooled down to room temperature in ambient air.

No.	Step	Parameter
1	Suspension	100 mg TiO_2 in 10 ml MilliQ water
2	Sonication	20 min (avoid settle down of particles)
3	Surface wetting	500 µL covering the whole surface
4	Spinning	25 s ramp to 1000 rpm for 60 s, 500 rpm 100 s
5	Repetition	10 times
6	Drying	1 h at 80 °C

Table 3.3: Preparation routine for the thin homogeneous films.

3.5.1 Substrates for TiO_2 films

For the internal reflection spectroscopy various substrate materials and shapes can be used and are commercially available. The basic principle and physical aspects are discussed in Section 3.2.2. In this work Germanium single crystals are used because of their high refractive index of $n_{Ge} = 4$ [59], stability against solvents and relatively low cost. The initial cleaning procedure is wiping with ethanol and exposure to air plasma with Gala Instruments PlasmaPrep2 for several minutes. For severe impurities in the crystal´s surface diamond polishing paste is applied. The polishing procedure is done manually with different graded particle sizes from 3 µm to 250 nm. The cleaning process is evaluated by SEM and AFM techniques. The results can be found in Section 4.1.

3.5.2 Porous thins films by spin coating

A common way of preparing thin TiO_2 films for dyes sensitized solar cells is doctor blading of Dyesol paste [60]. After calcination a homogeneous film of anatase TiO_2 particles with a thickness of 5 - 7 µm is formed and can be seen in Figure 4.4. The aim of the preparation with the received TiO_2 nanoparticles was to establish a procedure with similar homogeneity but with a film thickness below 1 µm. As stated in Section 3.2.2 this thickness is well within the penetration depth of the evanescent field. Additionally this leads to a lower diffusion barrier for dyes and reactants [36].

The preparations of such homogeneous layers from the TiO_2 powders was achieved by spin coating of a aqueous TiO_2 suspension onto the substrate as shown in Figure 3.11. The parameters of suspension density, spin coating speed and duration are determined experimentally. Table 3.3 shows the preparation routine for the thin homogeneous films.

Figure 3.11: Preparation methods for thin film preparation: Ultra sonic bath (left), spin coater with substrate (middle) and preparation routine (right). A fast spin coating reduces the attachment of particle agglomerations. With multiple spin cycles a closed, homogenious film is achieved.

3.5.3 Suspensions of dye sensitized TiO_2

A different sample form is preferred when addressing total amount analysis of dye and reactant adsorption as well as conversion rates. More surface area can be provided when using catalyst suspensions instead of thin films. The preparation of dye sensitized TiO_2 is done in six steps as shown in Figure 3.12. Mix the solvent and dye in a defined concentration and immerse the TiO_2 nanoparticles in the dye solution. Centrifuge and remove the supernatant dye and resuspend the aggregated nanoparticles. Additionally the washing procedure can be repeated. Figure 3.13 shows the centrifuged dye sensitized nanoparticles in the bottom of the tubes and the supernatant after the second washing cycle.

3.6 Quantitative IR band analysis

The quantitative analysis of a single IR band intensity can be done with the integration of its peak area. When bands are overlapping a fit function which corresponds to the underlying line shape has to be applied. The line shape for gas phase measurements are Lorentzian, for solids Gaussian and for liquids a mixture between the two which is a Voigt profile [61].

In this work IR spectra are taken at the solid liquid interface with a focus on the adsorbed species so a Gaussian fit profile was applied. The band position is taken from the tentative band assignment and set as a fixed value. Before the peak analysis

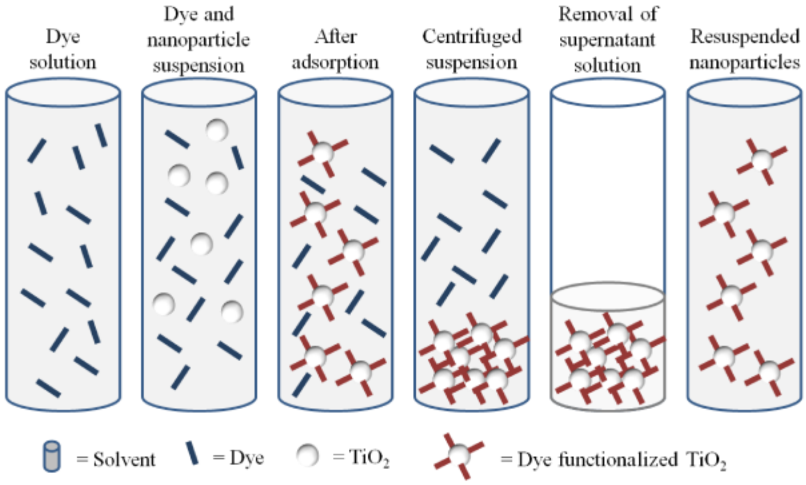

Figure 3.12: Schematic overview of the preparation of dye sensitized TiO_2 suspensions.

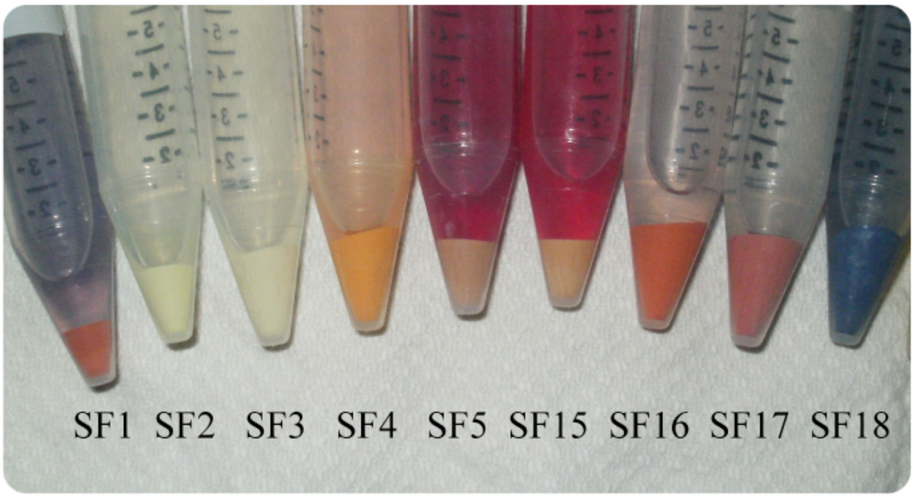

Figure 3.13: Centrifuged and washed suspension of dyes with TiO_2

a baseline correction is performed with anchoring points on wavenumber without band movement. The implementation of the fits and graphical evaluation is done with OriginPro 9.0G.

4 Results & Discussion

The focus of this work is the interaction of dyes and reactants on TiO_2 and metal impregnated TiO_2 nanoparticles and their photocatalytic potential. The sample preparation is controlled by microscopic methods and its results are shown in the first section of material characterization. Furthermore, optical properties of the TiO_2 and dye sensitized TiO_2 reveal the photo absorption range of the material. The binding mechanism of the dyes to the TiO_2 is probed by time-resolved ATR IR spectroscopy and compared to complementary SFG spectroscopy in Section 4.3. Following the dye adsorption, reactants are brought to the catalyst. Concentration controlled ATR IR experiments of water saturated CO_2 with irradiation in the UV or visible range are shown in Section 4.4.

4.1 Material & sample characterization

The raw material and preparation methods described in Section 3.5.2 are controlled by surface microscopy and energy dispersive X-ray spectroscopy.

4.1.1 Morphology and structure of TiO_2 and TiO_2 impregnated with co-catalysts

The TiO_2 P25 nanoparticles are already well characterized. A summary of properties is given in Section 3.4.1. The TiO_2 nanoparticle powders with co-catalysts are prepared by a wet chemical procedure described in Section 3.4.1 and are therefore investigated by EDX-SEM to determine the metal distribution on the nanoparticles.

Figure 4.1 shows scanning electron micrographs of two TiO_2 and two metal impregnated TiO_2 powder samples. The particle size and distribution is measured with a secondary electron detector (SE2). The metal distribution on TiO_2 particles is best measured by an in-lens detector due to their difference in atomic number. The nanoparticles are spin coated on a germanium substrate from an aqueous suspension. Sample A is TiO_2 P25 and shows well separated TiO_2 nanoparticles with a size distribution as specified around 23 nm- 31 nm. Sample B is TiO_2 with a specified particle size of 7 nm. The agglomeration to bigger clusters in the range of 100 nm is visible whereas the single particles are hardly distinguishable. Sample C shows TiO_2 with 0.5 weight % copper impregnation and sample D TiO_2 with 0.1 weight % palladium impregnation. The increase in resolution due to higher conductivity allows the use of the in-lens detector. This gives the advantage of material distinction. In both samples the topmost particles are brighter due to shorter distance to the detector. On the particles itself no inhomogeneity can be seen, which is a hint for a very fine distribution of the metals.

To determine the absolute metal distribution on the TiO_2 particles SEM-EDX measurements are performed on the copper impregnated particles. The solution is dripped on the substrate without spin coating and different sample areas are detected. The result in Figure 4.2 shows agglomerations with either very high or very low copper content. The signal from the non agglomerated surface shows very low signal due to its small thickness.

Another important parameter for metal catalyst is the oxidation state. The metal co-catalysts act as electron scavengers for the promotion of multi-electron transfer to the reactant. Therefore a high oxidation state is desired. XPS and Auger electron spectroscopy (AES) measurements by Florian Staier show a Cu_2O composition which corresponds to a Cu(1) oxidation state (Figure 4.3). Similar measurements determined the oxidation state of the palladium co-catalysts to Pd(0).

The results are very interesting because a majority of metal co-catalyst is agglomerated and the distribution on the nanoparticles could be rather low. The EDX measurements is difficult on the thin film part because of the lack of material.

4.1.2 Microscopy of prepared porous thin films

The preparation method of nanoporous TiO_2 films is designed to reduce the amount of particle agglomerations and create a homogeneous closed layer. The quality reference in surface homogeneity is the preparation method described in [36]. Figure 4.4 shows the surface prepared with Dyesol paste [60] compared to spin coated TiO_2 surfaces with the method elaborated in this work. All film samples are prepared from a 100 mg nanoparticle in 10 mL aqueous suspension which is spin coated 10 times with a spinning speed of 1000 rpm for 2 minutes per cycle. The result turns out as desired. The thin film shows no agglomerations or gaps.

The film thickness is measured by atomic force microscopy. The porous film is scratched with a cotton stick. This results in a fringed edge. Therefore pictures with a large scan area are taken and the height is averaged at the plateaus. Figure 4.5 shows an atomic force micrograph of TiO_2 on germanium internal reflection element which can be transferred directly to the flow through cell. All film heights measured are in the range of 320 nm - 370 nm with a medium roughness of 50 nm. This means there are roughly 10-15 stacked particles from top to bottom which makes penetration of adsorbates through the whole film very easy.

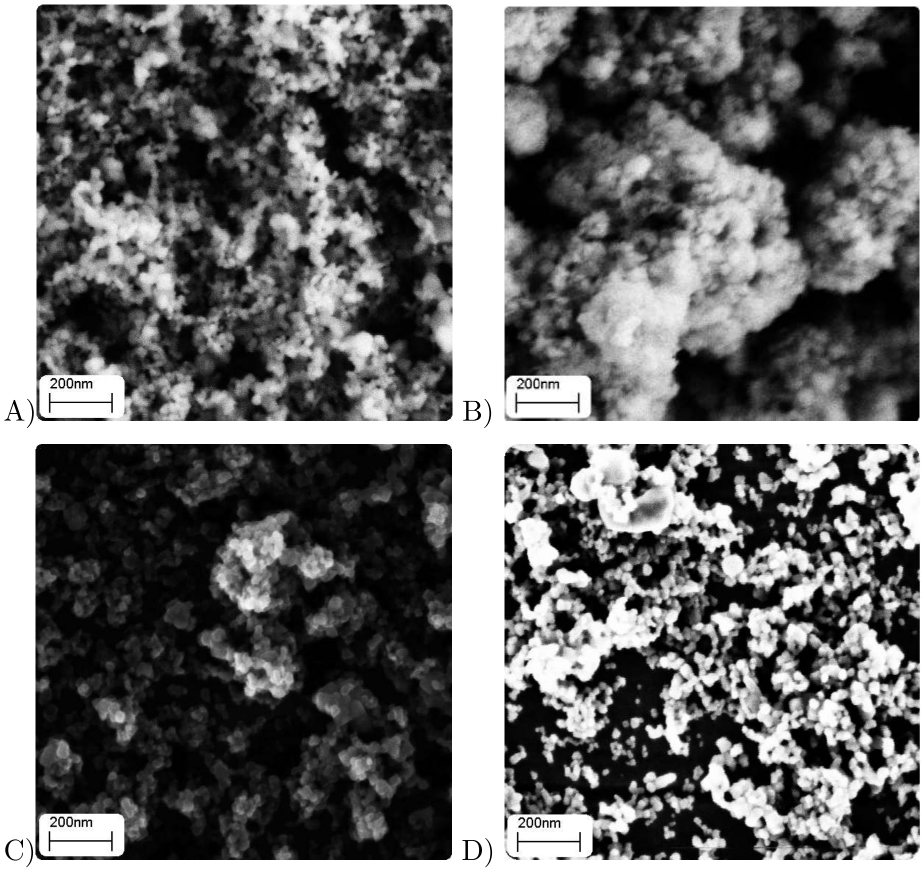

Figure 4.1: Scanning electron micrographs of A) TiO_2 P25, B) TiO_2 B1, C) TiO_2 with copper impregnation, D) TiO_2 P25 with palladium impregnation. Sample A and B are taken with 3 keV acceleration voltage and SE2 detector. Sample C and D with 7 keV acceleration voltage and in-lens detector. The particle size of samples A, C, D is 25 ± 5 nm as expected. The particle size of sample B is below the resolution limit but specified to 7 nm [56]. The enhanced resolution of micrographs C and D indicates a homogenous metal distribution over the TiO_2 nanoparticles.

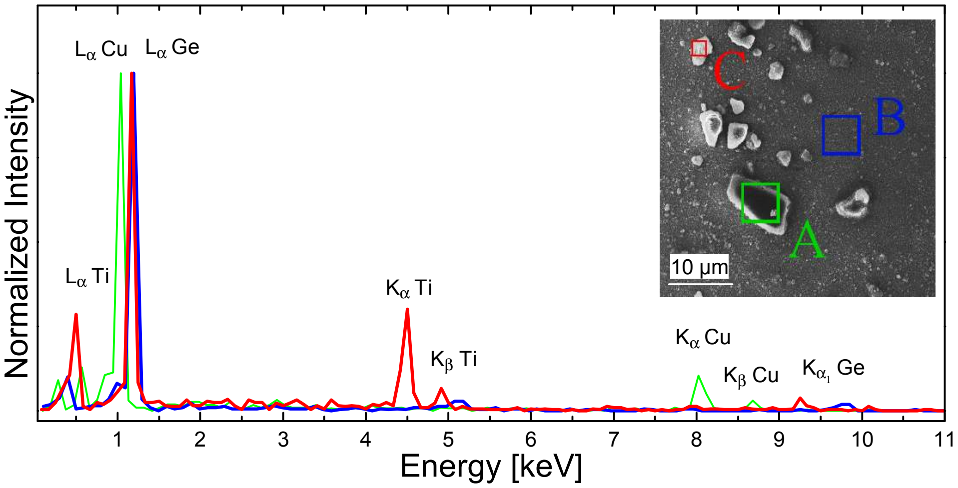

Figure 4.2: EDX signal of different surface areas of Copper impregnated TiO_2 nanoparticles. The Intensity is normalized to the maximum peak intensity.

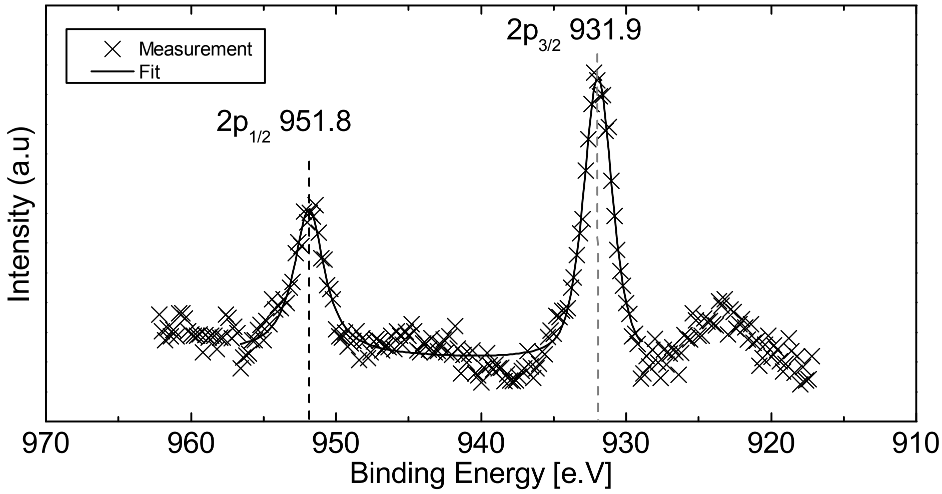

Figure 4.3: XPS of copper co-catalyst on TiO_2. The observed Cu $2p_{3/2}$ and $2p_{1/2}$ binding energy is closest to Cu_2O binding energy which corresponds to a Cu(1) oxidation state [62].

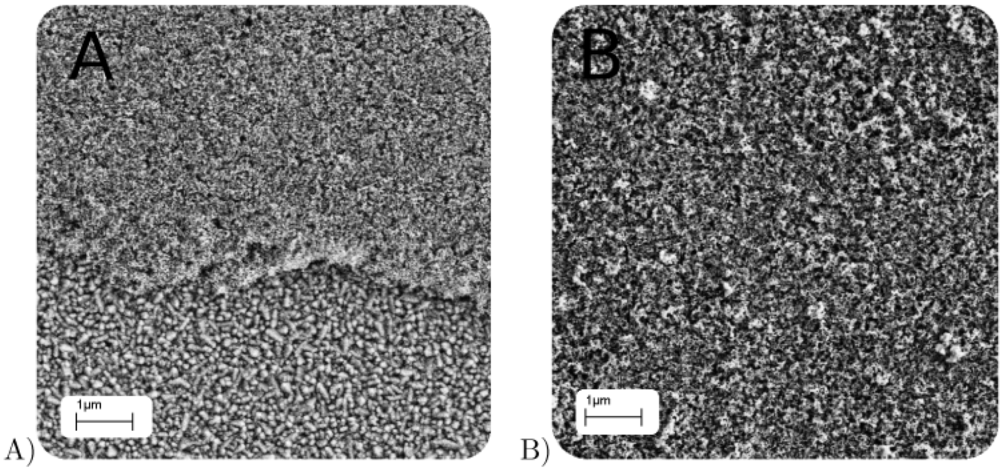

Figure 4.4: Scanning electron micrographs of A) Dyesol TiO_2 (top) on TiO_2 blocking layer (bottom) as prepared for DSSCs and B) spin coated TiO_2 on germanium substrate. The Secondary Electron detector and acceleration energy of 3 keV are used for the micrographs.

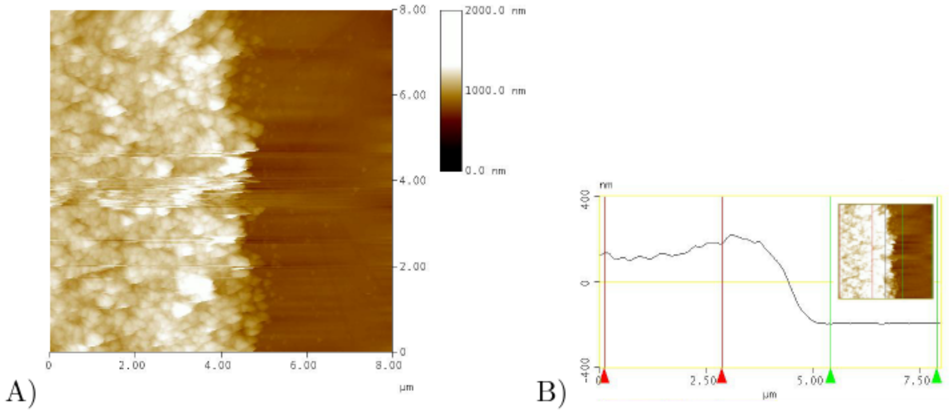

Figure 4.5: A) Atomic force micrograph of spin coated TiO_2 P25 on a germanium substrate. The porous film is partly removed to check the film height. B) The average height difference between the two plateaus is 330 nm with 50 nm mean roughness of the porous film.

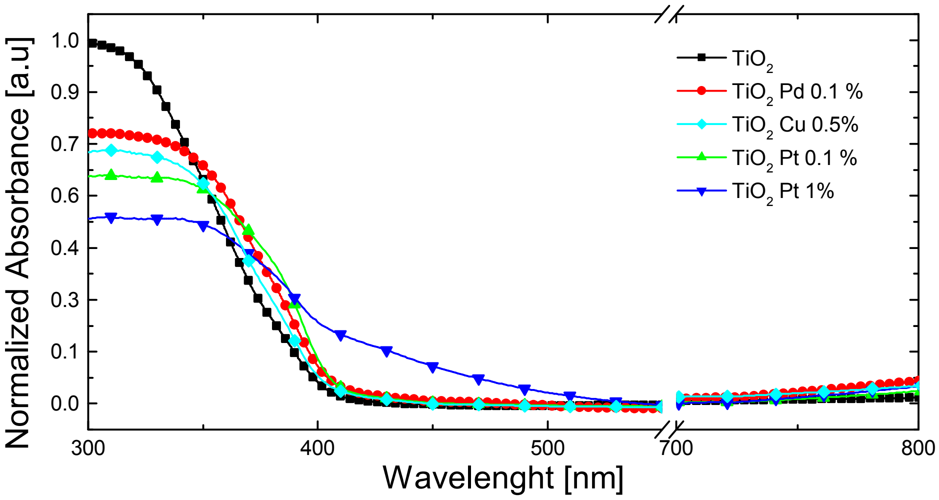

Figure 4.6: Photoabsorption of TiO_2 P25 nanoparticles and metal impregnated TiO_2 P25 nanoparticles.

4.1.3 Photoabsorption of TiO_2 with metal impregnation and dyes

The absorption of photons in the UV and visible range of the TiO_2 with metal impregnation or with dye sensitization is measured by diffuse reflection photometry. The setup is shown in Figure 3.6. The principles and setup is described in Section 3.2.3. The samples are prepared on a quartz glass substrate. Five times a 100 µl 10:1 mg/ml aqueous nanoparticle suspension is dripped on the substrate and dried. The resulting spectra are shown in Figure 4.6. The photoabsorption of the TiO_2 P25 and TiO_2 P25 metal impregnated samples show a strong increase below 400 nm. This corresponds to the excitation of valence band electrons into the conduction band of the nanoparticles. Metal impregnated TiO_2 shows a lower absorbance in the UV. TiO_2 with 1 weight % Pt additionally shows a small absorbance between 400 nm and 500 nm.

The addition of metal co-catalyst has a significant influence on the photoabsorption and higher metal loading could lead to the desired absorption towards the visible light spectrum. To shift the absorption maxima even more towards the visible range dye sensitization is performed. The mechanisms of dye anchoring process is discussed in the following section.

4.2 Quantitative dye adsorption, Photoabsorption and Photocurrent

The injection of electrons from the dyes to the TiO_2 relies on the anchoring coordination of the dye to the TiO_2. The total amount of dye adsorbed and the spectral range of dye excitation contribute to the resulting photocurrent. The understanding of these properties is used to determine an optimized performance in electron-hole splitting.

Starting from a quantitative analysis of the total amount of dye adsorbed on the TiO_2, the spectral photoabsorption is measured with photometry. The measurements are correlated with provided data of photocurrents.

Quantitative dye adsorption measurements are performed with transmission photometry. A concentration dependent calibration curve is measured for each dye solution. The calibration is performed with single wavelength transmission measurement. The wavelength is set to the absorption maximum of the respective dye in solution. The values are shown in Figure 4.8 and 4.9. The dye´s body determines the color of the dye in solution. The perylene dyes with diphenylamine are blue and absorb very strong at 590 nm and weak at 450 nm. The perylene dyes with triphenylamine are violet and absorb at 530 nm. The carbazole/rhodanine dyes show a very narrow absorption at 436 nm.

The total amount of dyes adsorbed on TiO_2 nanoparticles is determined indirect by measuring the difference of invested dye and the unadsorbed dye for a fixed suspension concentration. Therefore 100 mg TiO_2 nanoparticles are mixed with 10 ml of 0.5 mmol/L dye solution in tetrahydrofuran (THF). The suspension is sonicated for 5 min and stored for 16 h. The samples are then centrifuged at 4600 rpm for one hour. The supernatant dye concentration is measured and the difference to the loading solution shows the amount of adsorbed dye. The supernatant is removed and refilled with pure solvent. The sonication, centrifugation and substitution is repeated until the dye concentration in the supernatant does not change in the order of the estimated calibration error. The process is schematically shown in Figure 4.7.

The quantity of adsorbed dye is calculated as follows: The initial quantity of dye molecules in solution is N_0 and the quantity of dye molecules in the supernatant N_i after centrifugation is measured via absorbance photometry. Their difference is the total amount of dye still adsorbed on the nanoparticles. This value is divided by the surface area A invested in the suspension to show the quantity of dye molecules per square meter D :.

$$D_{\mathrm{Dye}} = \frac{(N_0 - N_1 - N_2 - N_3)}{A} \tag{4.1}$$

For $m_0 = 100\,\mathrm{mg}$ nanoparticles with $55\,\mathrm{m}^2/\mathrm{g}$ the surface area is $5.5\,\mathrm{m}^2$. The concentration c_i measured by photometry is calculated to an absolute value N_i by multiplying with the supernatant volume V_i: $N_i = c_i \cdot V_i$, where i is the number of the whole cycle.

From the density D of the adsorbed dye molecules one can calculate the area one dye molecule occupies $A_{\text{Dye}} = 1/D_{\text{Dye}}$.

The results are summarized in Table: 4.1 and show an impressive relation. The average surface occupancy A_{Dye} for dyes with anhydride anchoring group is twice as high as for single acid anchoring groups (carboxylic or hydroxamic acid). The anhydride anchoring dyes occupy3.8 $\cdot$ 10^{-18} m^2per dye molecule whereas the carboxylic and hydroxamic anchoring groups occupy 1.9 $\cdot$ 10^{-18} m^2per dye molecule. The other functional groups do not correlate with the coverage thus are assumed to make no contribution to the coverage of the surface.

This result is very important for the consideration of the binding coordination since the formation of two acid groups from the anhydride ring opening is suggested. If both acid groups bind to the surface the doubled surface uptake could be a reasonable explanation.

Another important observation is the concentration c_1 - c_3 of unadsorbed dye. The result shows much higher concentrations of unadsorbed dyes for the carboxylic anchoring group after the second washing processes. An exception is the dye SF1 with anhydride anchoring group. These dyes either form a multilayer which are washed off or have less strong bond formation than the rest of the dyes.

Another interesting observation is the drastic color change upon dye binding for the dyes with anhydride anchoring group. This shift is quantified with Photometry. The UV/VIS photometry spectra consist of a transmission spectra of a THF dye solution with the solvent as a reference and a diffuse reflectance spectra of the corresponding dye adsorbed on TiO_2 P25 with a white polystyrene block as a reference. As stated above the body of the dye determines its color in THF solution. But upon adsorption the anchoring group again shows a direct correlation to the shift in adsorption frequency. The dyes with anhydride anchoring group show an average frequency shift of $\varnothing\Delta\lambda_{\text{anhydride}} = -80\,\text{nm}$, $\varnothing\Delta\lambda_{\text{hydroxamic}} = -30\,\text{nm}$ and $\varnothing\Delta\lambda_{\text{carboxylic}} = -20\,\text{nm}$. The corresponding spectra are shown in Figure 4.8 and 4.9.

The efficiency of the electron transfer of excited dyes to the TiO_2 is reported from photocurrent measurements. The data is kindly provided by Florian Staier. A substrate with a sputtered gold layer is covered with TiO_2 P25 and immersed into dye solution. After rinsing, the sample is put in an electrolyte solution and connected to the anode via an ampermeter. The sample is irradiated with the visible part of a 75 W Xe-lamp with a 435 nm cut off filter.

The highest peak current is observed for the SF3 dye with hydroxamic acid anchor followed by SF15 dye with carboxylic acid anchor and SF17 with anhydride anchor. There is no direct correlation between peak intensity and functional group. Overall the most dyes with anhydride anchoring group are towards the end of the table and

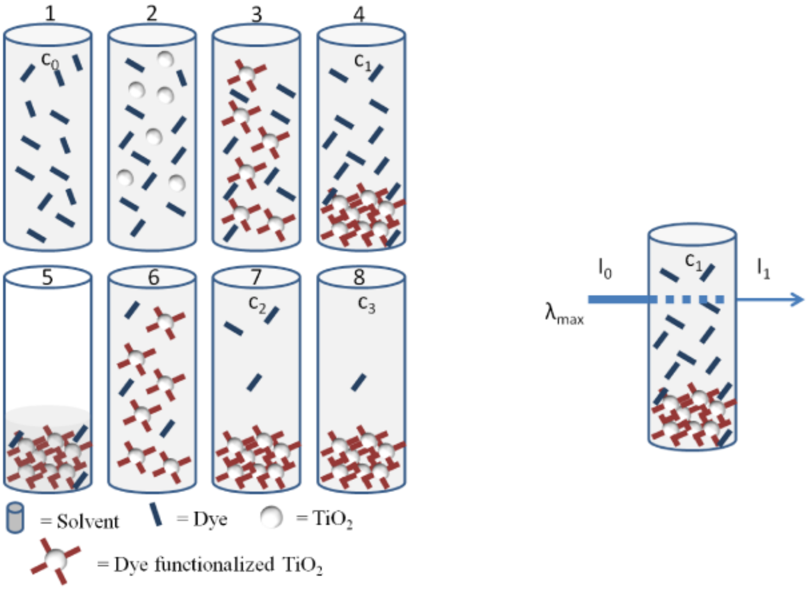

Figure 4.7: Scheme of quantitative analysis of dye adsorption on TiO_2 nanoparticles. Step 1 contains preparation of dye loading solution of 0.5 mmol/L in tetrahydrofuran. Step 2 and 3 is mixing the solution with 100 mg TiO_2 nanoparticles which subsequently adsorb the dye. Measuring the amount of unadsorbed dye (c_1) with photometry in step 4 followed by removing and refreshing the supernatant (step 5 and 6). The last two steps are repeated and the dye concentration in the supernatant is measured again (c_2, c_3 in step 7 & 8).

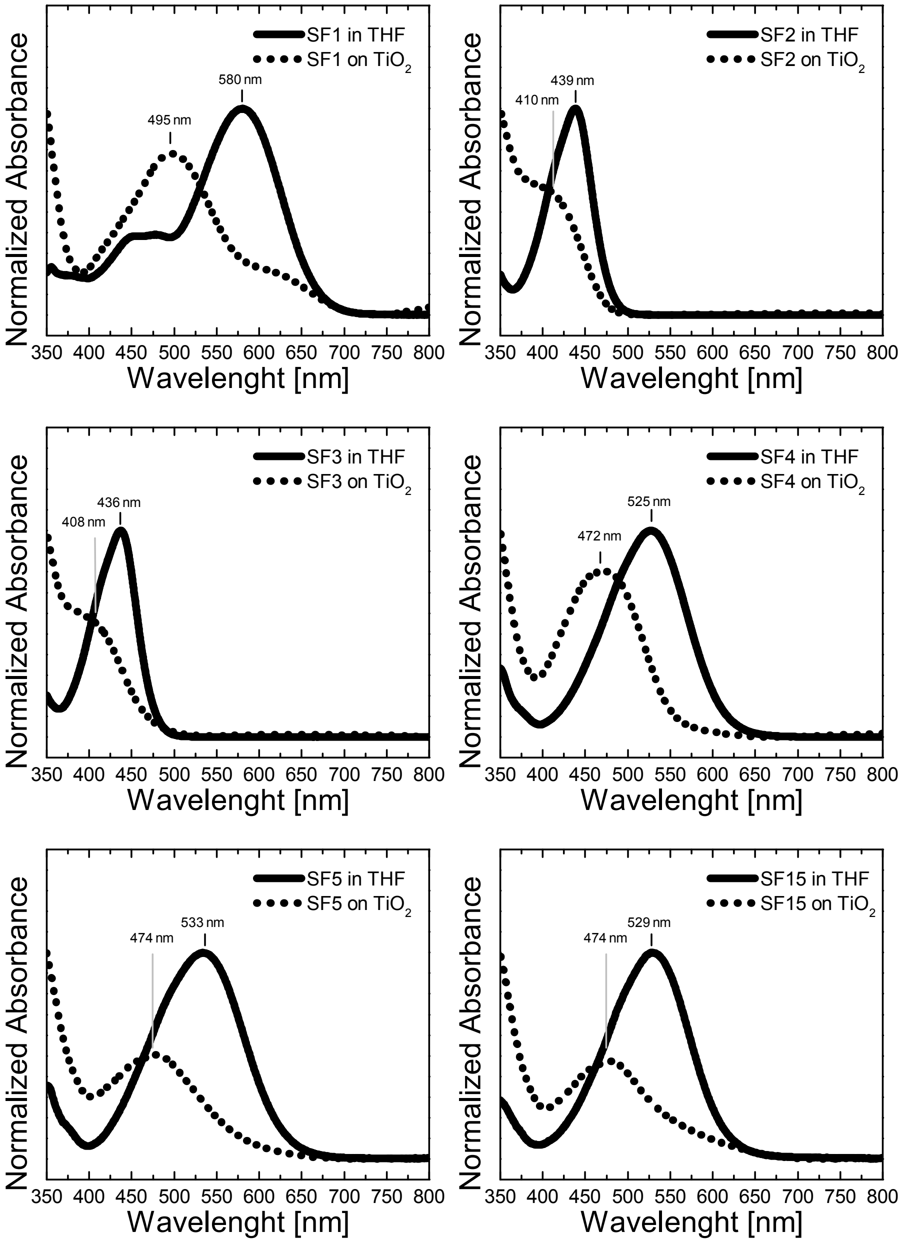

Figure 4.8: UV/VIS Photometry of dye SF1-SF5 and SF15 solution in THF (full line) and diffuse reflectance of a particle film (dotted line). The spectra are normalized to their maximum intensity between 350 cm^{-1} and 800 cm^{-1}.

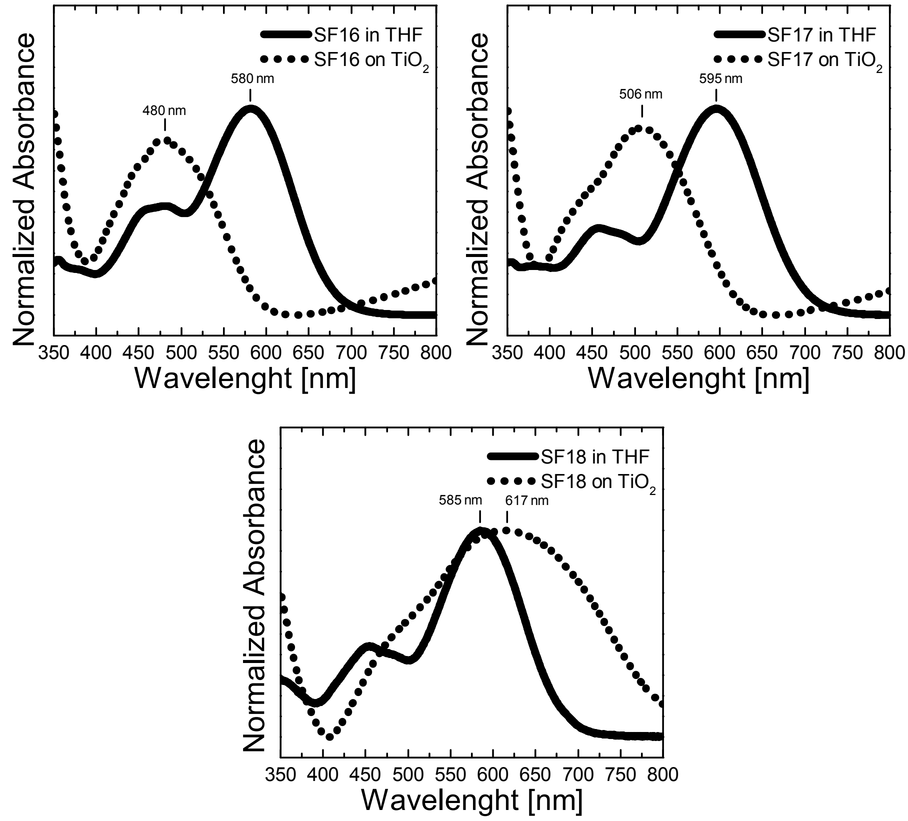

Figure 4.9: UV/VIS Photometry of dye SF16-SF18 solution in THF (full line) and diffuse reflectance of a particle film (dotted line). The spectra are normalized to their maximum intensitybetween 350 cm^{-1} and 800 cm^{-1}.

Table 4.1: Quantitative dye adsorption on TiO_2 P25.

Dye	**c1 [mmol/L]**	**c2 [mmol/L]**	**c3 [mmol/L]**	**Density of adsorbed dye [1/m^2]**	**Dye molecule surface uptake [m^2]**
SF1[a]	0.284	0.030	0.025	$3.30 \cdot 10^{17}$	$3.03 \cdot 10^{-18}$
SF2[c]	0.001	0.002	-	$5.47 \cdot 10^{17}$	$1.82 \cdot 10^{-18}$
SF3[h]	0.030	0.006	-	$5.11 \cdot 10^{17}$	$1.95 \cdot 10^{-18}$
SF4[a]	0.268	0.014	0.006	$2.64 \cdot 10^{17}$	$3.78 \cdot 10^{-18}$
SF5[a]	0.305	0.010	0.002	$2.31 \cdot 10^{17}$	$4.32 \cdot 10^{-18}$
SF15[c]	0.001	0.037	-	$5.43 \cdot 10^{17}$	$1.84 \cdot 10^{-18}$
SF16[a]	0.229	0.001	0.001	$3.10 \cdot 10^{17}$	$3.23 \cdot 10^{-18}$
SF17[a]	0.313	0.011	0.007	$2.14 \cdot 10^{17}$	$4.67 \cdot 10^{-18}$
SF18[c]	0.013	0.023	0.025	$5.11 \cdot 10^{17}$	$1.96 \cdot 10^{-18}$
Average anhydride				$2.7 \cdot 10^{17}$	$3.8 \cdot 10^{-18}$
Average carboxylic & hydroxamic				$5.28 \cdot 10^{17}$	$1.9 \cdot 10^{-18}$

Legend: a; anhydride anchoring group; c, carboxylic anchoring group; h, hydroxamic anchoring group

Table 4.2: Peak current of visible light irradiated dye sensitized TiO_2. The data is kindly provided by Florian Staier.

Dye	Peak current [µA]	Anchor	Body	Donor
SF3	7.08	Hydroxam	Rhodanine	Carbazole
SF15	6.90	Carboxyl	Perylene	Triphenylamine
SF17	6.51	Anhydrid	Perylene	Diphenylamine
SF2	4.94	Carboxyl	Rhodanine	Diphenylamine
SF1	3.04	Anhydrid	Perylene	Diphenylamine
SF16	1.81	Anhydrid	Perylene	Diphenylamine
SF4	1.40	Anhydrid	Perylene	Diphenylamine
SF5	0.35	Anhydrid	Perylene	Triphenylamine
SF18	0.22	Carboxyl	Perylene	Diphenylamine

again the average peak intensity is higher for the single acid anchoring groups.The results of the peak intensity is summarized in Table: 4.2.

The quantitative dye adsorption, photoabsorption and photocurrents show significant trends for the understanding of the impact of functional groups. Dyes with anhydride group are strongly bound but have a lower coverage than the single acid anchoring groups and therefore lower photoconversion rates. All dyes have to be tested towards their stability when facing the reactants. To reveal the binding mechanism of the dyes and test their stability during H_2O and CO_2 presence during the irradiation of visible light in-situ IR spectroscopy is performed.

4.3 Anchoring mechanism of dyes adsorbed on TiO_2

The understanding of anchoring mechanisms and kinetics play a crucial role in catalyst preparation and electron transfer efficiency. The ATR IR spectroscopy exhibits various advantages for solid liquid interface analysis. The comparison of IR bands of free dye with in-situ binding dye to TiO_2 is used to track the structural modification upon the molecular binding.

From the whole set of dyes two pairs are selected because they feature the same structure with exception of the anchoring moiety. This helps to assign IR bands of the dyes and shows the difference in the adsorption kinetics solely with one parameter changed. SF2 is compared with SF3 and SF5 with SF15. The band assignment of the free dyes given is followed by the results of the in-situ adsorption measurements.

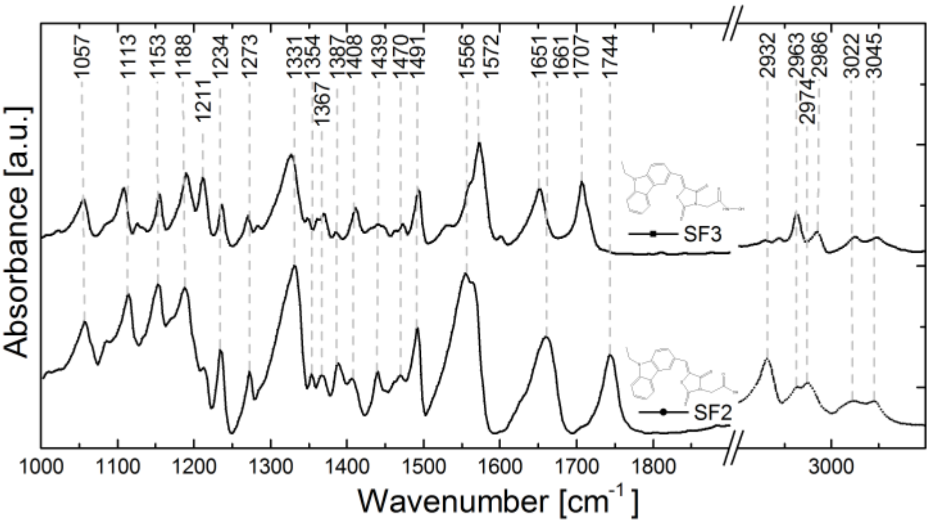

Figure 4.10: ATR IR spectra of the free dye SF2 (carboxylic anchor) and SF3 (hydroxamic anchor) powder. The spectra are kindly provided by Anna Keese.

4.3.1 IR band assignment of free dyes

For the in-situ adsorption measurements an IR band assignment of the pure dye powder is performed. These ATR spectra are kindly provided by Anna Keese [33].

Figure 4.10 shows the ATR IR spectra of SF2 and SF3 which only differ in the anchoring moiety. The dyes with carboxylic acid anchor posesses a distinguishable band at 1744 cm^{-1} (SF2), 1742 (SF15), 1738 (SF18, not shown) assigned to the ν(C=O) of this moiety. The hydroxamic acid anchor also inhibits a ν(C=O) but in the vicinity of a nitrogen atom. This vibration is assigned to the band at 1651 cm^{-1} [63]. These are the most important bands for SF2 and SF3. The spectra are very similar in between 1330 cm^{-1} and 1500 cm^{-1}. The tentative band assignment is summarized in Table 4.3.

The IR spectra of the anhydride anchoring group shown in Figure 4.4 features two bands at 1718 cm^{-1} and 1757 cm^{-1} which are attributed to ν_{as}(C=O) and ν_{s}(C=O) respectively. Another difference of SF5 and SF15 is the imide functionality to which the carboxylic anchor is attached. The bands at 1653 cm^{-1} and 1690 cm^{-1} are attributed to this moiety. The other part of the spectrum is again very similar. Very prominent are the perylene vibrations ν(C=C-C) at 1566 cm^{-1} and 1591 cm^{-1}as well as 1452 cm^{-1} and 1497 cm^{-1}. A tentative summary of the IR bands can be found in Table 4.4.

The band assignment for the anchoring groups is possible despite the complexity of the molecules. The comparison of dyes which differ in only one functionality is a huge advantage.

Table 4.3: Tentative band assignment of dye SF2 and SF3 powder.

Band assignment	**Wavenumber [cm^{-1}]**	
	SF2	**SF3**
ν_s (C–H) [64]	3045	3045
ν_s (C–H) [64]	3022	3022
ν_s (C–H) [64]		2986
ν_s (C–H) [64]	2974	
ν_{as} (CH_3) [64]	2963	2963
ν_{as} (CH_3) [64]	2932	
ν_{as} (COOH) [65]	1744	
ν_{as} (C=O) lactam [66]		1707
ν (C=O) lactam [65]	1661	
ν (NC=O) amide I [66]		1651
ν_{as} (C–N) [66]		1572
ν (C–C) aryl [66]	1556	1556
ν (C–C) aryl [66]	1491	1491
δ_s (CH_2) [66]	1470	1470
δ_s (CH_3) [66]	1439	1439
δ_{ip} (C-O-H) [65]	1408	1408
δ_s (CH_3)[66]	1387	1387
δ (C–H) [65]	1367	1367
δ (C–H) [65]	1354	
δ (C–H) [65]	1331	1331
ν(C-N) + ν(C-C) + δ(N-H) Amid III [64]	1273	1273
ν (C–O) acid [64]	1234	1234
N.N.		1211
N.N.	1188	1188
N.N.	1153	1153
N.N.	1113	1113
ν (C=S) [64]	1057	1057

Legend: ν, stretching; δ, bending; s, symmetric; as, asymmetric; ip, in plane; gem, geminal (two identical functional groups bound to the same carbon atom); st, strong band; w, weak band.

Table 4.4: Tentative IR band assignment of dye SF5 and SF15 powder. The assignment is extended from previous work [33].

Band assignment	**Wavenumber [cm^{-1}]**	
	SF5	**SF15**
ν_{s} (C=C–H) [67]	3040	3040
ν_{as} (O–$\mathrm{CH_2}$) [68]	2922	2922
ν_{s} ($\mathrm{CH_3}$) [68]	2866	2866
ν_{s} (O–$\mathrm{CH_2}$) [68]	2818	2818
ν_{s} (C=O) anhydride [67]	1757	–
ν (C=O) acid [67]	–	1742
ν_{as} (C=O) anhydride [67]	1718	–
ν_{s} (C=O) imide [67]	–	1690
ν_{as} (C=O) imide [67]	–	1653
ν (C=C–C) perylene [69]	1591	1591
ν (C=C–C) perylene [69]	1566	1566
ν (C=C–C) perylene [69]	1497	1497
ν (C=C–C) perylene and δ_{as} ($\mathrm{CH_3}$), δ_{s} (O–$\mathrm{CH_3}$), δ_{s} ($\mathrm{CH_2}$), δ_{s} (O–$\mathrm{CH_2}$) [69]	1452	1452
ν (C=C–C) perylene and δ_{s} ($\mathrm{CH_3}$) trimethyl, δ_{s} (O–$\mathrm{CH_3}$), δ_{s} (O–$\mathrm{CH_3}$), ν (C–N) [70]	1404	–
ν (C=C–C) perylene [69]	–	1391
ν (C=C–C) perylene and ν (C–N) [69]	1371	1371 *st*
ν (C=C–C) perylene [69]	1339 *st*	–
ν (C=C–C) perylene and δ_{s} ($\mathrm{CH_3}$) *gem*-trimethyl [69][70]	–	1317
δ_{ip} (C=C–C–H) [67]	1281	1281
δ_{ip} (C–H) [67][68]	1231	1231
δ_{ip} (C=C–C–H) [67]	1192	1192
δ_{ip} (C=C–C–H) [69]	1161	1161
δ_{ip} (C=C–C–H) [67]	1128	1128
δ_{ip} (C=C–C–H) [67]	1099	1099
δ_{ip} (C=C–C–H) [67]	1061	1061
ν_{as} (C–O–C) anhydride [70]	1020 *w*	1020

Legend: ν, stretching; δ, bending; s, symmetric; as, asymmetric; ip, in plane; gem, geminal (two identical functional groups bound to the same carbon atom); st, strong band; w, weak band.

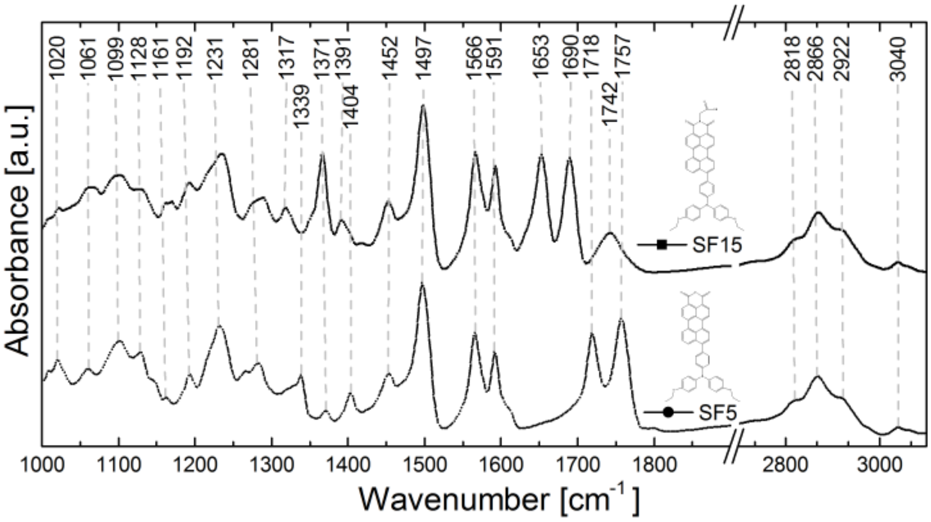

Figure 4.11: ATR IR spectra of the free dye SF5 (anhydride anchor) and SF15 (carboxylic anchor) powder taken from [33].

4.3.2 Dyes with carboxylic acid group on TiO_2 P25

A comparison of ATR IR spectra of free and bound dye SF15 to TiO_2 P25 (Figure 4.12) shows a lack of ν(C=O) stretching vibration at 1742 cm^{-1} for the adsorbed dye. This loss of carbonyl functionality of the acid group indicates a binding via this group. A monodentate ester type binding can be ruled out since there are no new bands in the specific spectral region (1720-1750 cm^{-1}) [71]. Thus carboxylate stretching modes $\nu_s(CO_2^-)$ and $\nu_{as}(CO_2^-)$ must be formed. The spectral region is expected to be around 1400 cm^{-1} and 1600 cm^{-1} respectively [72]. There are broad bands at 1642 cm^{-1} and 1611 cm^{-1} and also a small peak at 1402 cm^{-1}. Raman studies on a similar system also found increased bands at 1404 cm^{-1} and 1635 cm^{-1} [36].

Furthermore Figure 4.12 shows negative bands at 2840 cm^{-1} and 2965 cm^{-1} indicating a displacement of solvent by the dye molecules. A closer look on the carboxylate formation is possible with the in-situ adsorption measurements.

The adsorption process is monitored by in-situ ATR IR spectroscopy (Figure 4.13). The IR spectra are accumulated over 400 scans in 60 s with a resolution of 2 cm^{-1}. All solvents are heated to 35 °C for before purging into the flow through cell for a constant adsorption temperature and to reduce bubble formation. The porous TiO_2 P25 film is purged with tetrahydrofuran followed by 0.5 mmol/L dye solution and again pure tetrahydrofuran for one hour each cycle.

The in-situ adsorption IR measurement shows an increase of dye adsorbed up to a nearly constant maximum. Without TiO_2 no dye bands are visible due to the low concentration. This means the signal is solely from adsorbed dye. Purging with the

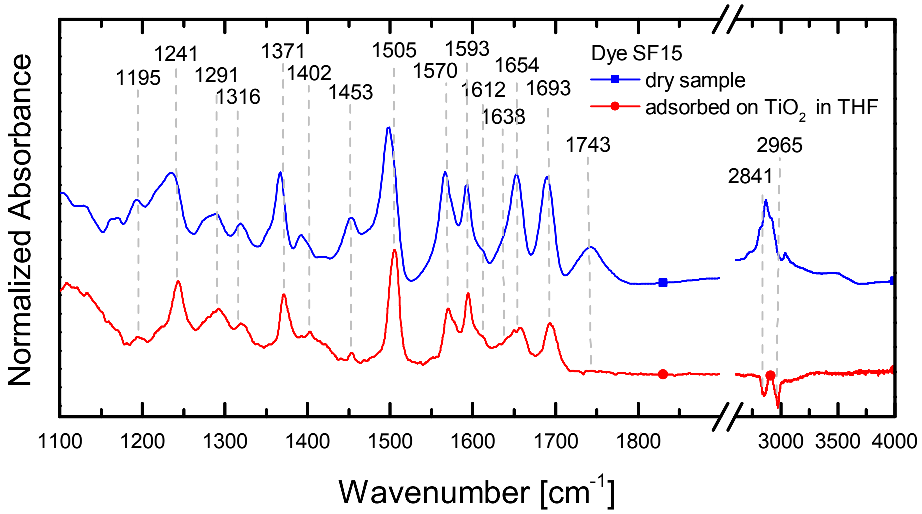

Figure 4.12: ATR IR spectra of free dye SF 15 (blue, cricle) compared to SF 15 adsorbed on TiO_2 P25 (red, square). The adsorption was performed in the flow through cell. A SF 15 solution (0.5 mmol/L in tetrahydrofuran) is adsorbed for 60 min and subsequently purged with tetrahydrofuran for 60 min (TiO_2 P25 with tetrahydrofuran used as reference). The spectral intensities are normalized to the peak at 1507 cm^{-1} and 1499 cm^{-1} respectively. The spectral positions are marked for the adsorbed dye.

solvent removes the dye partially. The negative bands at 1080 cm^{-1}, 2840 cm^{-1} and 2065 cm^{-1} show a displacement of solvent when the dye is introduced. When the excess dye is purged again, the solvent readsorbs partially. Due to the overlapping bands a fit of the marked bands in Figure 4.12 is performed for each spectra. The fit parameters are discussed in Section 3.6.

The integrated peak area of the carboxylate stretching modes $\nu_s(CO_2^-)$ at 1404 cm^{-1}, $\nu_{as}(CO_2^-)$ at 1611 cm^{-1} , the carbonyl functionality $\nu(C{=}O)$ at 1742 cm^{-1} and the complete peak area of the SF15 dye are shown in Figure 4.14. The peak areas of each band are normalized to highlight the different binding kinetics during dye adsorption and after purging with the solvent. The $\nu_{as}(CO_2^-)$ vibration is more stable compared to the whole dye indicating a chemisorbed bond formation. The $\nu_s(CO_2^-)$ is also slightly stronger. The carbonyl vibration of the free dye at 1742 cm^{-1} is so small that it is not visible in the adsorption process, The very low amount is completely washed away during purging process indicating an almost complete removal of unbound dye.

The temporal evolution of the carboxylate stretching modes shows a high stability compared to the carbonyl functionality which completely vanishes after purging. The lack of ester type vibrations leads to the conclusion that the carboxylic anchoring groups either bind via bidentate chelating or bidentate bridging coordination. As previously stated is the chelating and bridging coordination empirically distinguished by the difference of the frequencies of the adsorbed species compared to their salts (bridging coordination when$\triangle\nu_{ads} \leq \triangle\nu_{salt}$ and chelating when $\triangle\nu_{ads} \ll \triangle\nu_{salt}$) [34]. The salts of the dyes are not available, but the bridging coordination is known to be more stable than the chelating [73].

4.3.3 Dyes with anhydride group on TiO_2 P25

As the quantitative dye adsorption measurements (Section 4.2) suggests the adsorption of dye SF5 by an opening of the anhydride group. A possible reaction pathway is a ring opening and formation of two carboxylic acid groups when encountering surface bound hydroxyl groups. Again, the focus of the in-situ ATR IR adsorption measurements is on formation of carboxylic acid and their binding to the TiO_2 surface. The first step is to compare the free dye IR spectra with the spectra of adsorbed dye on TiO_2 P25. The band assignment of the free dye is shown in Table: 4.4. Figure 4.15 shows two ATR IR spectra of free Dye SF5 and SF5 bound to TiO_2 in an in-situ adsorption experiment. Compared to the free dye SF5 the bands of the adsorbed dye SF5 anhydride anchoring moiety (1726 cm^{-1} and 1761 cm^{-1}) are diminished. The in-situ dye adsorption is used to show the temporal evolution of the anhydride group and the bands where formed carboxylates are expected.

Figure 4.16 show the adsorption of the dye SF5 and washing process for selected temporal stages. When the dye solution reaches the porous thin TiO_2 P25 film ($t = 0$ min) the dye starts adsorbing. Note that without TiO_2 film, the concentration of dye molecules is too low to contribute to a signal. Two stages of adsorption can be

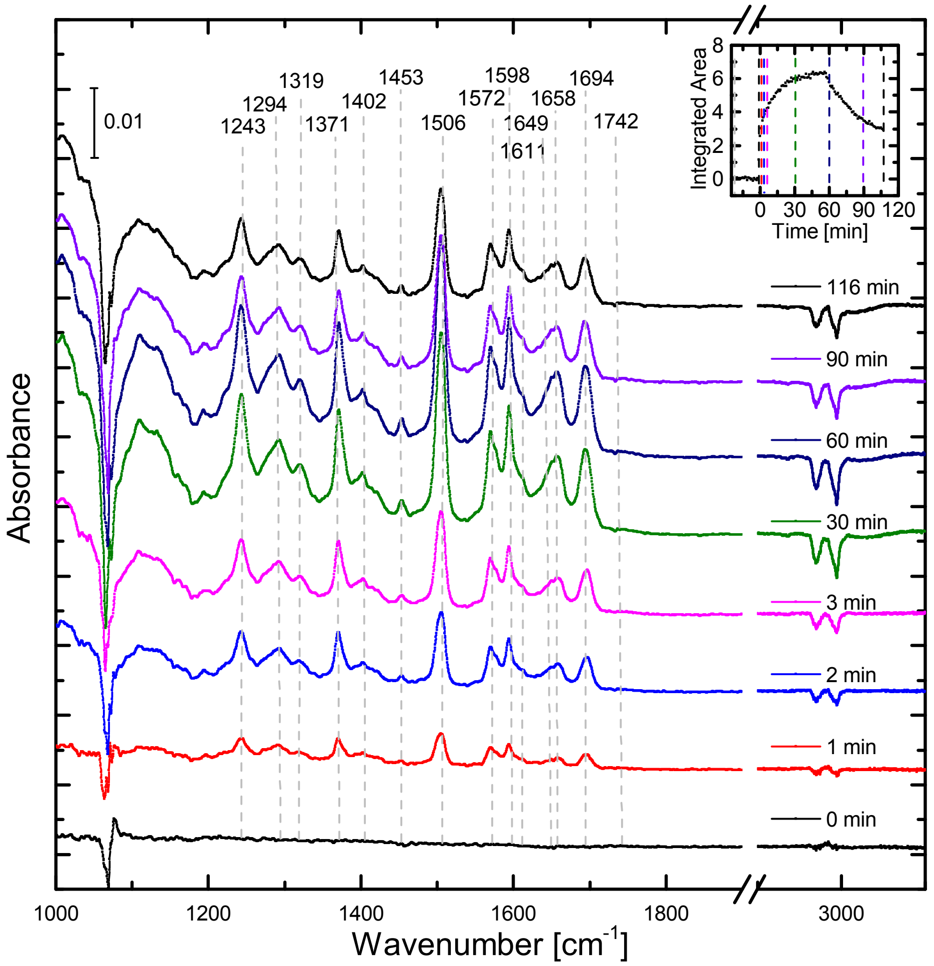

Figure 4.13: ATR IR spectra taken during adsorption of SF15 on TiO_2 P25 porous thin film and followed by purging with tetrahydrofuran solvent. Tetrahydrofuran is purged for 60 min followed by 0.5 mmol/L SF15 in tetrahydrofuran for 60 min ($T = 0$ min) and purging with pure solvent again for 60 min. IR Spectra are accumulated over 60 s. A selection of spectra is shown. TiO_2 P25 with tetrahydrofuran is used as reference. The inset graphic shows the total integrated dye band intensity with the dotted lines representing the extracted IR spectra.

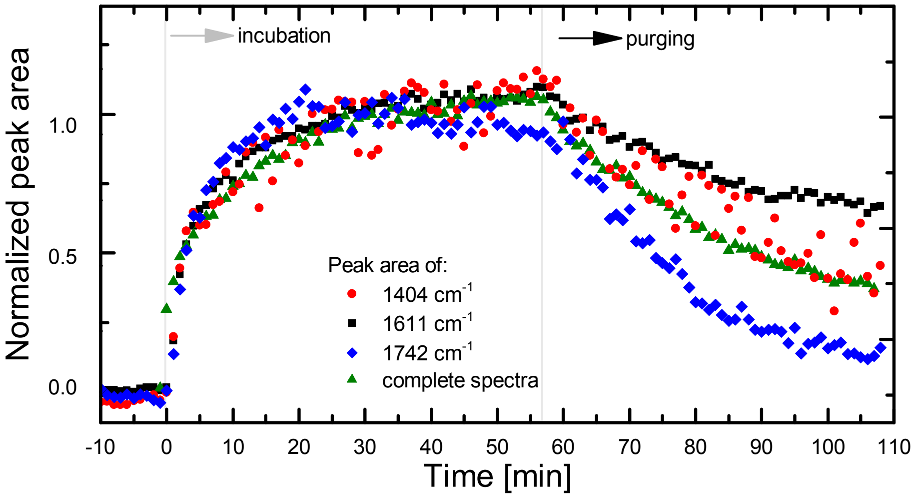

Figure 4.14: Temporal evolution of characteristic IR bands of SF15 adsorption from Figure 4.13. The maximum peak area of each band is normalized to 1 to show the different adsorption kinetics. The integrated peak area of the carboxylate stretching modes $\nu_\mathrm{s}(\mathrm{CO}_2^-)$ at 1404 cm^{-1}, $\nu_\mathrm{as}(\mathrm{CO}_2^-)$ at 1611 cm^{-1} , the carbonyl functionality $\nu(\mathrm{C{=}O})$ at 1742 cm^{-1} and the complete dye spectra area are shown. The adsorption starts at T = 0 min and ends at T = 57 min.

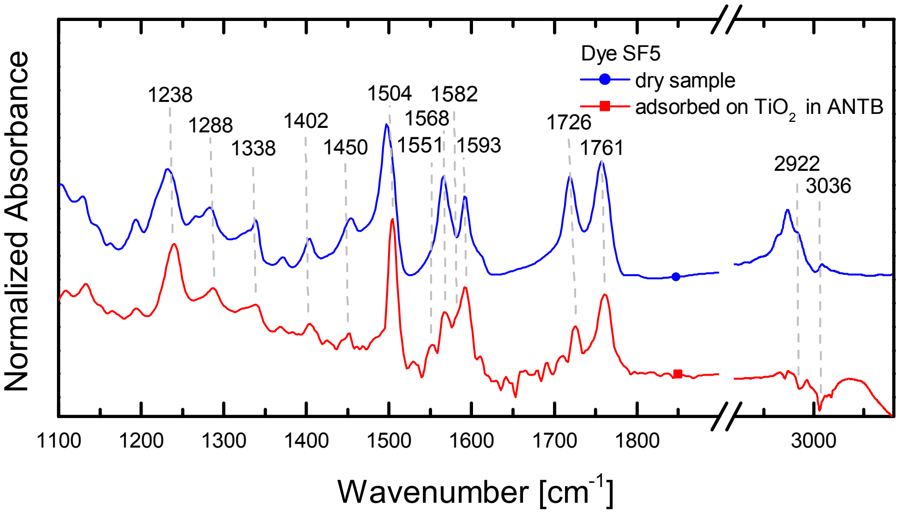

Figure 4.15: ATR IR spectra of free dye SF5 (blue, circle) compared to SF5 adsorbed on $\mathrm{TiO_2}$ P25 (red, square). The adsorption was performed in the flow through cell. A SF5 solution (0.5 mmol/L in toluene) is adsorbed for 100 min and subsequently purged with toluene for 100 min ($\mathrm{TiO_2}$ P25 with toluene used as reference). The spectral intensities are normalized to the peak at 1504 cm^{-1} and 1496 cm^{-1} respectively.The spectral positions are marked for the adsorbed dye.

observed. A quick rise of the dye IR bands during the first 5-6 minutes and a very slow rise until the washing process ($t = 106\,\text{min}$). The washing process to remove excessive dye shows a fast decrease in 5-6 minutes for all bands. The decrease of dye bands approach a constant intensity at roughly half of the maximum intensity.

The evolution of the most interesting bands are shown in Figure 4.17. The peak fit was performed by setting the maxima to the peaks of the adsorbed species and setting an upper limit for the FWHM which is necessary for a converging fit. The fit procedure is described in Section 3.6. The following bands are plotted: the IR bands $1761\,\text{cm}^{-1}$ and $1726\,\text{cm}^{-1}$which are assigned to the anhydride moiety, and the weak band at $1371\,\text{cm}^{-1}$ which is in the carboxylate region and which shows a strong increase compared to the free dye. The latter band intensity does not decrease upon washing with the solvent. In the same spectral region Völker [36] with in-situ ATR IR and Raman spectroscopy and Keese [33] with SFG and Raman spectroscopy observed similar bands after anhydride adsorption on TiO_2. The band is assigned to the carboxylate $\nu_s(CO_2^-)$. The asymmetric vibration of the carboxylate $\nu_{as}(CO_2^-)$ is overlapping the $\nu(C{=}C{-}C)$ stretching vibrations of the perylene body. By subtracting this band integral ($1568\,\text{cm}^{-1}$) and divide it by the relative band integral from the free dye, a excess of the $\nu_s(CO_2^-)$ can be seen. The signal of the anhydride moiety instantly reaches a maximum, which means the surface is predominantly covered by closed anhydride. Abut the dye overall signal still rises as well as the formed carboxylates. This can be explained by the suggested binding mechanism where the OH-groups of the surface only attack the dyes which are very close to the surface. After the anhydride opening the carboxylate formation begins.

The anchoring kinetic of the anhydride shows several very informative facts. Not all anhydride rings open directly upon adsorption, and the formation of carboxylates is very slow compared to the adsorption of SF15. This suggests a binding mechanism where the OH-groups of the surface only attack the dyes which are very close to the surface, which is followed by a carboxylate formation. The once adsorbed the dyes are bound very good and the binding process is almost irreversible.

The stability shown here and and the quantitative dye adsorption measurements lead to the conclusion that once the anhydride is opened both carboxylic acid groups bind to the surface. Again the coordination is not directly accessible and need further investigation.

4.3.4 Dyes with hydroxamic group on TiO_2 P25

The hydroxamic anchor is similar to the carboxylic anchor. The difference is a inserted nitrogen group which leads to higher resistance towards acids and aqueous solutions. The calculated amid IR absorption bands of adsorbed hydroxam are at $1665\,\text{cm}^{-1}$ and $1437\,\text{cm}^{-1}$ [10].

IR bands and assignment of free carbazole dye with hydroxamic anchor (SF3) is shown in Section 4.3.1. Figure 4.18 shows ATR IR spectra of the free dye and the

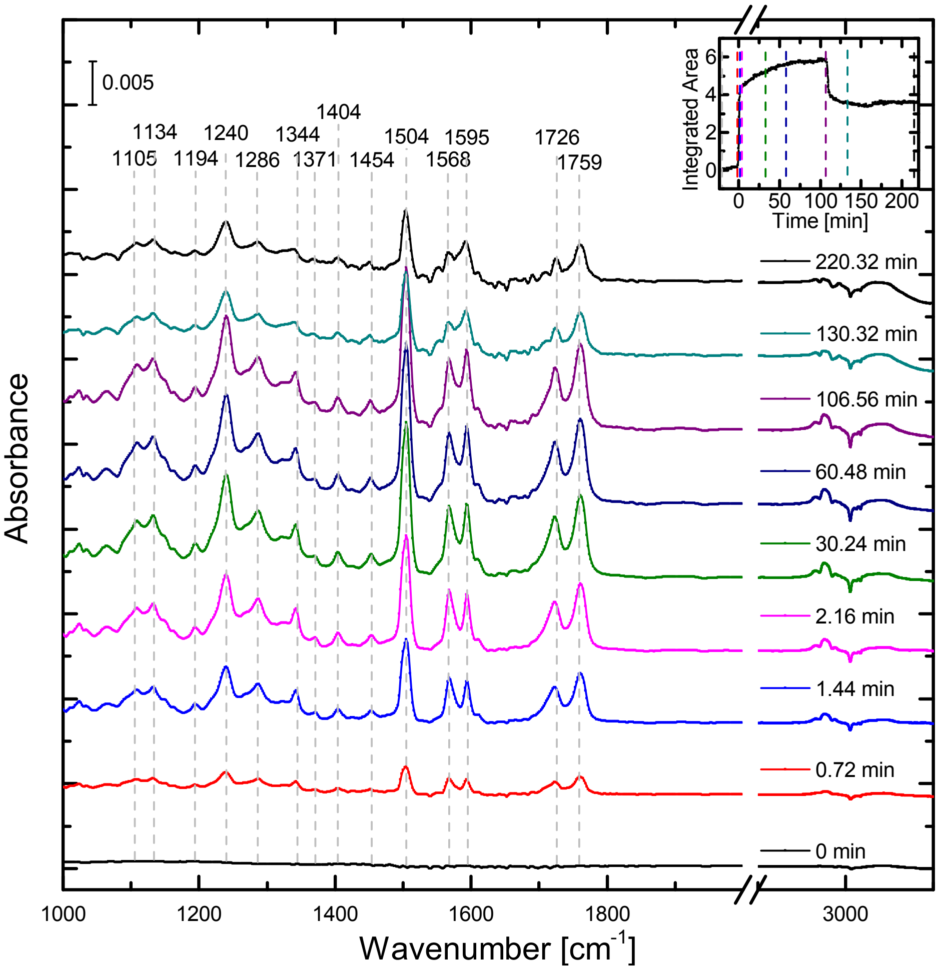

Figure 4.16: ATR IR spectra taken during adsorption of SF5 on TiO_2 P25 porous thin film and followed by purging with toluene solvent. Toluene is purged for 100 min followed by 0.5 mmol/L SF5 in toluene for 106 min and purging with pure solvent again for 100 min. 200 IR Spectra are accumulated for 45 s. The inset graphic shows the total integrated dye band intensity with the dotted lines representing the extracted IR spectra.

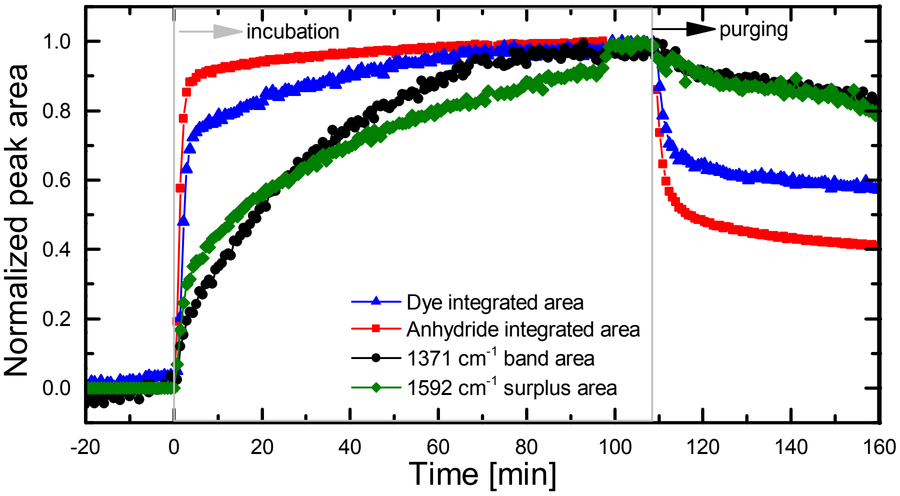

Figure 4.17: Temporal evolution of characteristic IR band areas of SF5 adsorption shown in Figure 4.16 normalized to 1. A comparison of the integrated areas of the dye spectra (blue), anhydride moiety (red), $\nu_a(CO_2^-)$ band at 1371 cm^{-1}(black) and the underlying $\nu_{as}(CO_2^-)$ at 1592 cm^{-1}(green) shows the slow reaction of the anhydride moiety to adsorbed carboxylate during the dye adsorption and its stability during the washing process.

dye adsorbed on thin film TiO_2 P25. The spectra are normalized to their overall integrated area to highlight the band positions. The adsorbed dye spectra (1 min immersed) shows an broadened hydroxam amide I (NC=O) band at 1651 cm^{-1} and an enhanced band at 1473 cm^{-1}. The bands at 1055 cm^{-1}, 1211 cm^{-1}, 1370 cm^{-1} and 1663 cm^{-1} are diminished.

After 60 minutes of dye adsorption and 100 min of purging with the solvent the residue of adsorbed dye changed. The hydroxam band at 1663 cm^{-1} is slightly diminished.

Due to the complexity of the molecule an identification of newly formed bands is difficult and is further analyzed by in-situ ATR spectroscopy.

The in-situ ATR IR measurements of dye SF3 adsorbed on TiO_2 P25 is shown in Figure 4.16. The dye IR bands shows a very slow adsorption in the first minutes but then starts rising quickly. All bands seem to increase and decrease at similar rate. But a fit of the bands (see Section 3.6) reveals more information.

The total peak area of the dye is compared with the peak area of the adsorbed hydroxamic acid at 1651 cm^{-1} in Figure 4.20. The hydroxamic acid (C=O) and reaches its maximum first, while the amount of dye adsorbing to the surface still rises.But there is no band which accounts for a chemical transformation. This could simply explained by multilayer formation. This multilayer is washed away upon the purging process which explains the decrease of overall dye signal but a strong binding

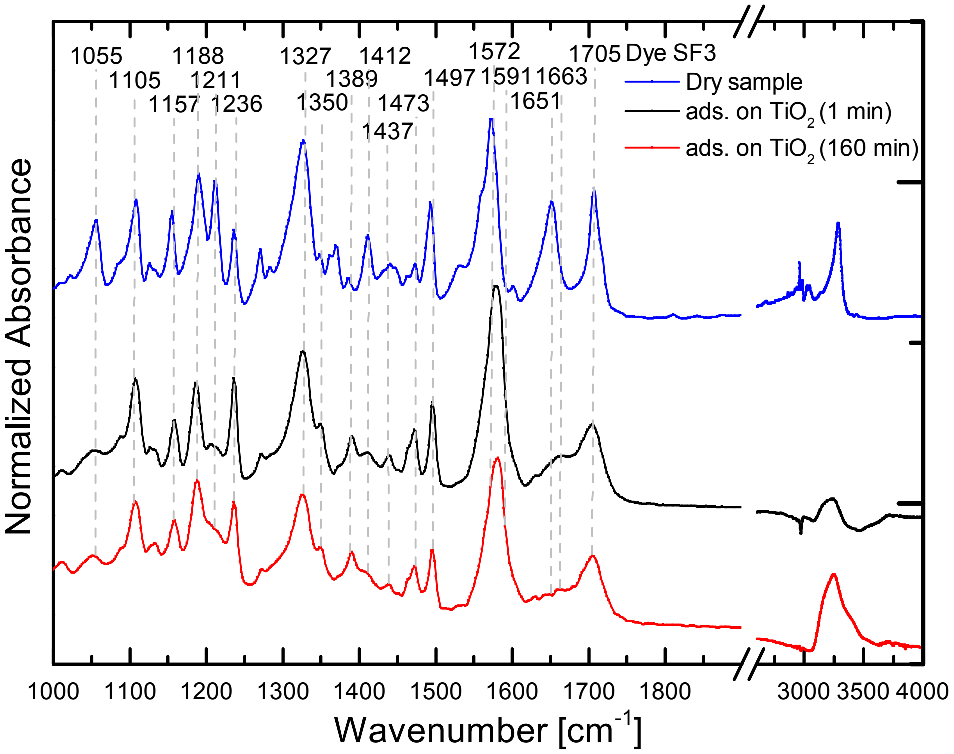

Figure 4.18: ATR IR spectra of free dye SF3 (blue) compared to SF3 adsorbed on TiO_2 P25 (red and black). The adsorption was performed in the flow through cell. A SF3 solution (0.5 mmol/L in ANTB) is purged for 100 min and subsequently washed with ANTB for 60 min (TiO_2 P25 with ANTB used as reference). The spectral intensities are normalized to the total peak area for band position analysis. The adsorbed dye spectra shows an broadened hydroxam amide I (NC=O) band at 1651 cm^{-1}.

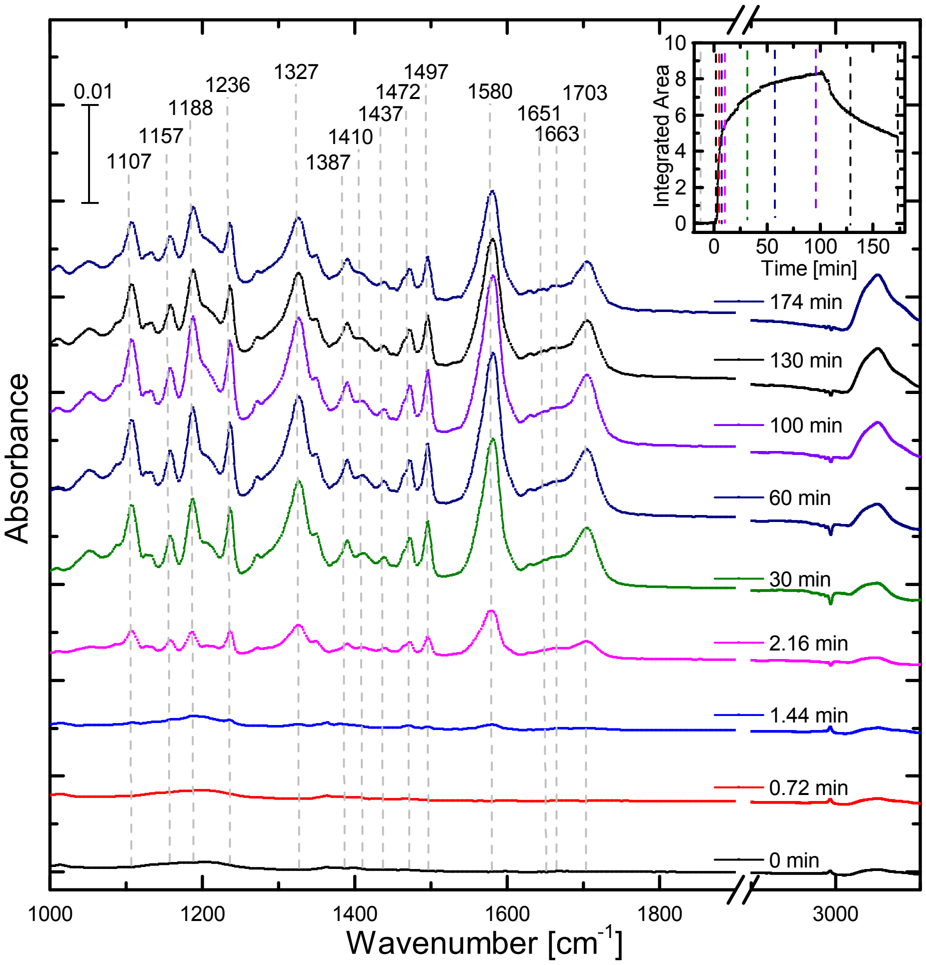

Figure 4.19: ATR IR spectra taken during adsorption of SF3 on TiO_2 P25 porous thin film and followed by purging with ANTB solvent. ANTB is purged for 100 min followed by 0.5 mmol/L SF3 in ANTB for 100 min and pure solvent for 60 min. 200 IR spectra are accumulated for 45 s. The inset graphic shows the total integrated dye band intensity with the dotted lines representing the extracted IR spectra.

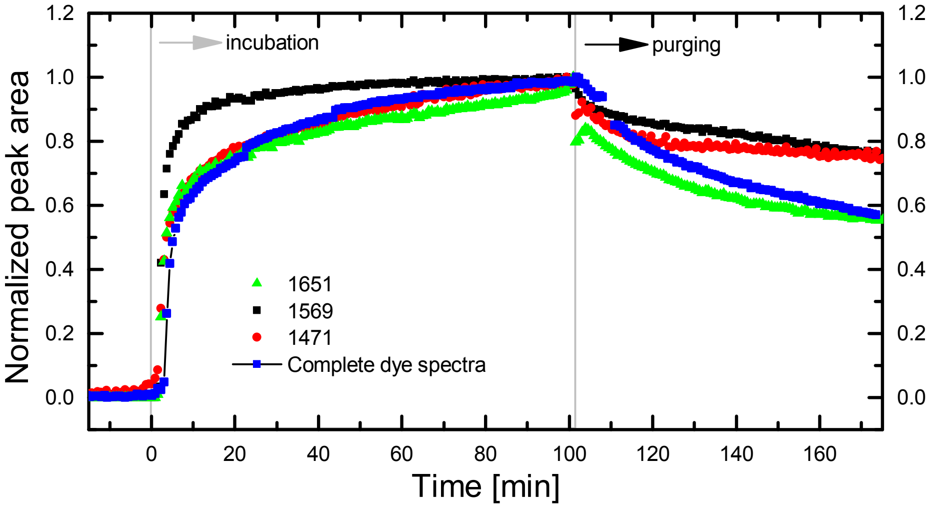

Figure 4.20: Temporal evolution of characteristic IR band areas of SF3 adsorption shown in Figure 4.19. The maximum intensity of each band is normalized to 1. A comparison of the integrated areas of the complete dye spectra and adsorbed hydroxam moiety shows a significant kinetic difference for the ν(C=O) at 1651 cm^{-1} of the hydroxamic anchoring group compared to the complete dye spectra area.

of the ν(C=O) from the hydroxamic anchor.

The hydroxamic acid anchoring group has a lower reaction speed than the carboxylic anchoring group but is more stable. The anhydride anchoring group undergoes a splitting when attached to the surface followed by the formation of two bidentate carboxylates most likely in bridging coordination. The binding coordination for the carboxylate is via one bidentate carboxylate this explains the twice as high surface coverage for the dyes with carboxylic acid. Since the surface coverage for the hydroxamic acid is similar to the carboxylic acid a bidentate bridging coordination is suggested.

4.4 CO_2 co-adsorption from aqueous solution on dye sensitized TiO_2 and photoabsorption

The mechanistic analysis of CO_2 adsorption and photochemical reactions on the photocatalyst is performed by in-situ ATR IR spectroscopy in an ATR flow through cell with quartz glass window for irradiation. CO_2 is adsorbed from an saturated aqueous solution and a Xe-lamp with IR and UV or VIS filter is used to irradiate the photocatalyst. The focus is on CO_2 and carbonate adsorption coordination, their kinetics with or without irradiation and the phyotocatalyst stability. The influence of dye sensitization and metal co-catalysts are introduced subsequently.

The experiments start with catalyst preparation on the reflection element and the encapsulation in the flow through cell. The cell is inserted in the IR ATR reflection stage. The spectrometer is closed and evacuated. The peristaltic pump is used to generate a flow of 0.02 L/h MilliQ water (pH 6, 35 °C) over the photocatalyst. A frit is used to saturate MilliQ water in a separate beaker with CO_2 at 35 °C (pH 4-5). The flow is switched to CO_2 saturated water back and forth while the photocatalyst is irradiated with the Xe-lamp with bandpass filters. IR spectra are accumulated depending on signal strength every 30-60 s.

In the following section a tentative band assignment of adsorbed CO_2 on TiO_2 P25 in contrast to a blank reflection element is used as a guideline for the CO_2 adsorption on modified and irradiated photocatalysts.

4.4.1 IR band assignment

For the interpretation of the in-situ ATR IR measurements an overview over the most prominent bands of water and CO_2 adsorption on a blank IRE and TiO_2 coated IRE are discussed in advance. Figure 4.21 shows CO_2 adsorbed from aqueous solution on TiO_2 and a blank IRE. Water has two well known strong adsorption bands at $\delta_{\mathrm{OH}} = 1642\,\mathrm{cm^{-1}}$and ν_{OH} between $3000\,\mathrm{cm^{-1}}$ - $3650\,\mathrm{cm^{-1}}$ [74]. The band at $2343\,\mathrm{cm^{-1}}$corresponds to CO_2 molecules dissolved in the aqueous solution and are present with and without catalyst [75]. In the blank IRE measurement no other bands are visible, although carbonate and bicarbonate should be present. The reason is a low concentration as shown in Section 2.5.1. With TiO_2 on the IRE two strong bands at $1320\,\mathrm{cm^{-1}}$ and $1585\,\mathrm{cm^{-1}}$appear indicating a bidentate carbonate configuration. Two smaller bands at $1050\,\mathrm{cm^{-1}}$ and $1480\,\mathrm{cm^{-1}}$indicate a monodentate configuration as well [47]. A broad negative band between $3000\,\mathrm{cm^{-1}}$ and $3600\,\mathrm{cm^{-1}}$ shows a replacement of surface hydroxyls and adsorbed water. The tentative band assignment is summarized in Table 4.5.

4.4.2 In-situ CO_2 adsorption on TiO_2 and irradiation

The first in-situ CO_2 adsorption experiments are performed on TiO_2 P25 without dyes attached. The sample preparation (Section 3.5) shows an average porous film thickness of 350 nm as characterized in Section 4.1. Figure 4.22 shows the in-situ ATR IR spectra of CO_2 in aqueous solution. The flow through cell (Figure 3.4) is purged with water for 20 min followed by CO_2 saturated water (T = 0 min) for 20 min and switch back to pure water purging. All reservoirs are kept at 35 °C and 400 IR scans are accumulated every 60 s with a resolution of $2\,\mathrm{cm^{-1}}$.

During the first 20 min of water purging two bands at $1642\,\mathrm{cm^{-1}}$ and $3600\,\mathrm{cm^{-1}}$ are constantly rising. The band at $1642\,\mathrm{cm^{-1}}$ is similar to the bulk water band but the $3600\,\mathrm{cm^{-1}}$ band is near the Ti-OH band. At T = 0 the CO_2 saturated water reaches the flow through cell. The cell is completely purged within 2 s. A sharp peak of

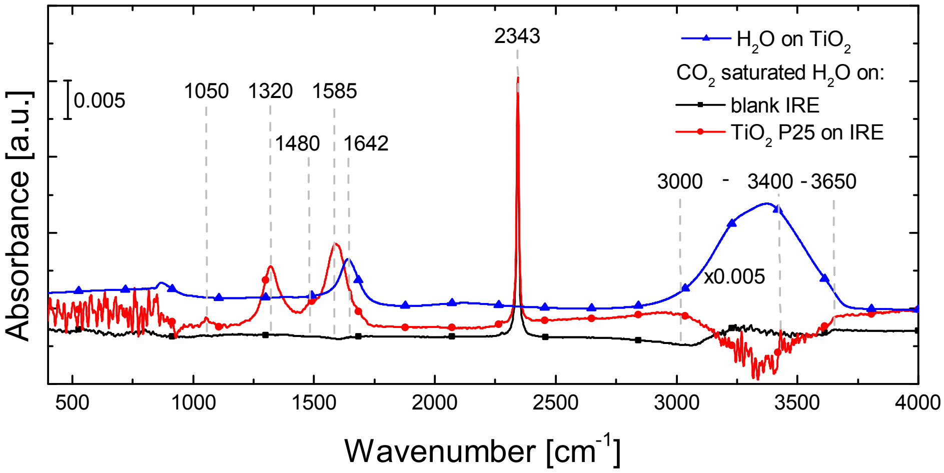

Figure 4.21: The blue (triangle) curve shows a ATR IR spectra of water on TiO_2 with blank TiO_2 as a reference. In red (circle) CO_2 saturated water adsorbed on TiO_2 with TiO_2 and water as reference compared to black (square) with CO_2 saturated water on germanium internal reflection element (IRE) and water as a reference. The curves summarize all occurring bands during CO_2 adorption experiments.

Table 4.5: Tentative band assignment of CO_2 in aqueous solution adsorbed on TiO_2. A configuration scheme is shown in Figure 2.8.

Band assignment	**Wavenumber [cm^{-1}]**	
	blank IRE	**TiO_2 P25**
ν (C–O)	-	1050 w
Bidentate $\nu_a(CO_IO_I)$	-	1320
Monodentate $\nu_s(CO_{II}O_{II})$	-	1480
Bidentate $\nu(CO_{II})$	-	1585
$\delta_{as,s}(H_2O)$	-	1642
CO_2 molecular dissolved	2343	2343
$\nu_{as,s}(H_2O)$	-	3400-3600

Legend: ν, stretching; δ, bending; s, symmetric; as, asymmetric;

the dissolved CO_2 at 2342 cm^{-1} and two broad carbonate bands at 1590 cm^{-1} and 1320 cm^{-1} rise whereas the bands at 1642 cm^{-1}, 3600 cm^{-1} and 3300 cm^{-1}decrease. As shown in Section 4.4.1 these carbonate bands only appear with TiO_2 on the reflection element so they must be adsorbed on the TiO_2 particle surface. The intensity increases and reaches a saturation value. At $T = 20$ min the CO_2 saturated water is replaced by pure water again. The dissolved CO_2 vanishes completely whereas the carbonate bands decrease slowly to a nearly constant value. This is a clear sign for physisorbed dissolved CO_2 and chemisorbed carbonates. The broad bulk water peak at 3300 cm^{-1} stays constant below the initial intensity indicating an exchange process of water near the TiO_2 surface with the carbonates.

Figure 4.23 shows the ATR IR spectra during irradiation of the chemisorbed carbonates. During a constant flow of H_2O the surface is irradiated with a 75W Xe-lamp and the respective Schott glass filters and IR filter. The visible light filter is only transmits $\lambda_{GG435} > 435$ nm whereas the UV filter is a bandpass filter and transmits 230 nm $< \lambda_{DUG11x} <$400 nm. The irradiation intensity on the catalyst flow through cell is 232 mW/(cm^2) without filter, 141 mW/(cm^2) for visible light and 23 mW/(cm^2) for UV light with 20 % error margin [76]. The temperature measurement at the flow through cell shows an increase of 4 °C for visible light and 0.5 °C for UV light irradiation after 20 min. During visible light irradiation a broad band around 1026 cm^{-1}, and two bands at 1635 cm^{-1} and 3600 cm^{-1} rise slowly. The band at 1635 cm^{-1} and 3600 cm^{-1}are attributed to adsorbed H_2O. The increase in temperature leads to a higher surface coverage of adsorbed water. The wavenumber is sightly off the bulk water wavenumber 1642 cm^{-1}. Since the broad band at 1026 cm^{-1} rises slowly it is also attributed to a temperature effect. In contrast a sudden rise of a broad band at 880 cm^{-1} tailoring up to 2000 cm^{-1} can be seen during UV irradiation in Figure 4.23 B). Furthermore, during UV light irradiation a negative band at 1658 cm^{-1}can be seen. The broad absorption is attributed to electronic excitations from shallow traps in the TiO_2 to the continuum of states in the conduction band and intraconduction band [77][78]. The absorbance loss at 1658 cm^{-1} is attributed to a desorption of strongly hydrogen-bonded interfacial water [79]. The carbonates bound to the surface are stable on the TiO_2 surface upon either visible and UV light irradiation in the respective time and detection limits.

The effect of temperature increase due to visible light irradiation is compared with temperature the effect of temperature increase by heating up the solvent. Figure 4.24 shows the water temperature difference spectra of room temperature with water at 50 °C. The spectra of irradiated and thermally warmed water adsorbed on TiO_2 are identical. A possible explanation for the band shift from 1642 cm^{-1} to 1635 cm^{-1} and 3200 cm^{-1} to 3600 cm^{-1} is a rearrangement of adsorbed water on TiO_2. The band at 860 cm^{-1} and band bending between 1800 cm^{-1} and 2800 cm^{-1} follow excactly the single channel signal, which is an artifact arising from the MCT detector [76].

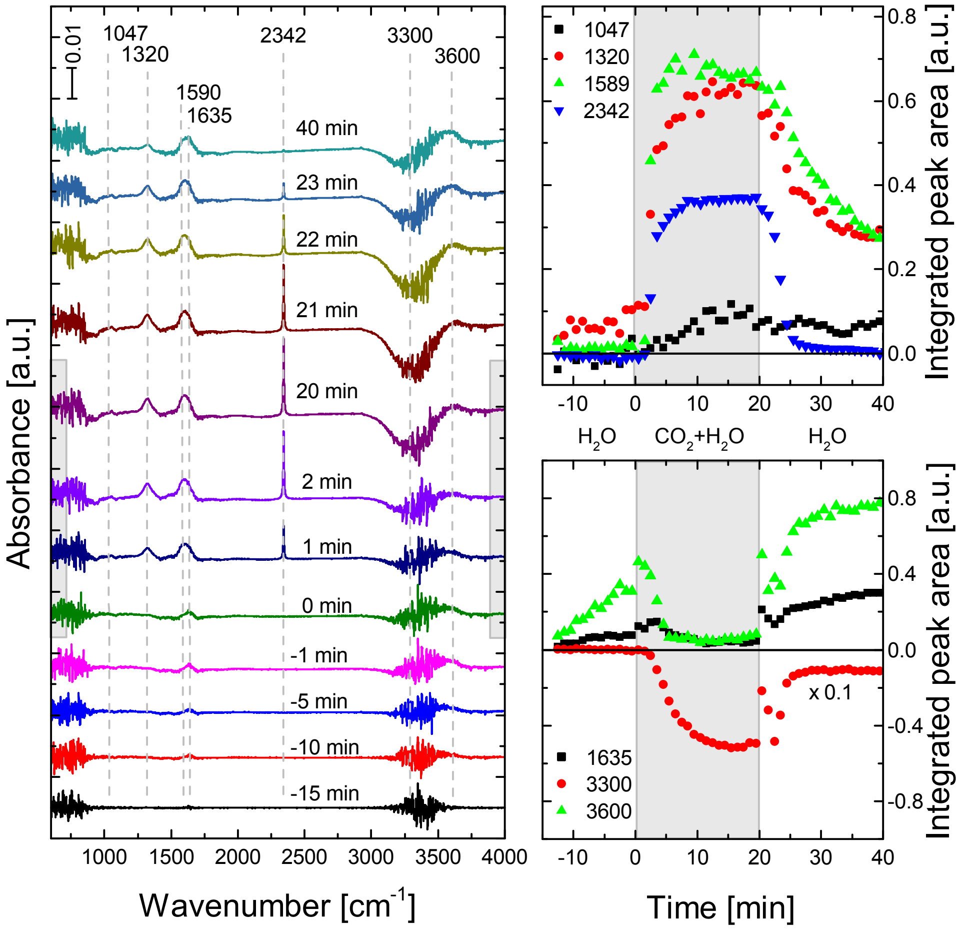

Figure 4.22: Left: ATR IR spectra of CO_2 adsorbed on TiO_2 from saturated aqueous solution for 20 min. Purging with H_2O before and after the adsorption process. Right: Integrated area of peak fit of the prominent bands. Highlighted in gray is the exposure to CO_2 saturated water.

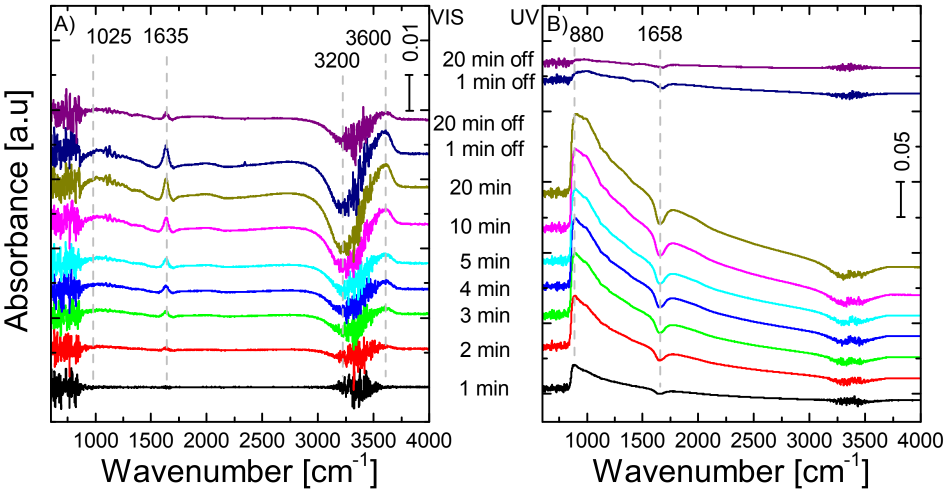

Figure 4.23: ATR IR spectra of A) visible and B) UV light irradiation of CO_2 adsorbed from aqueous solution on TiO_2 P25 during constant water flow. The spectra of adsorbed carbonates is used as background.

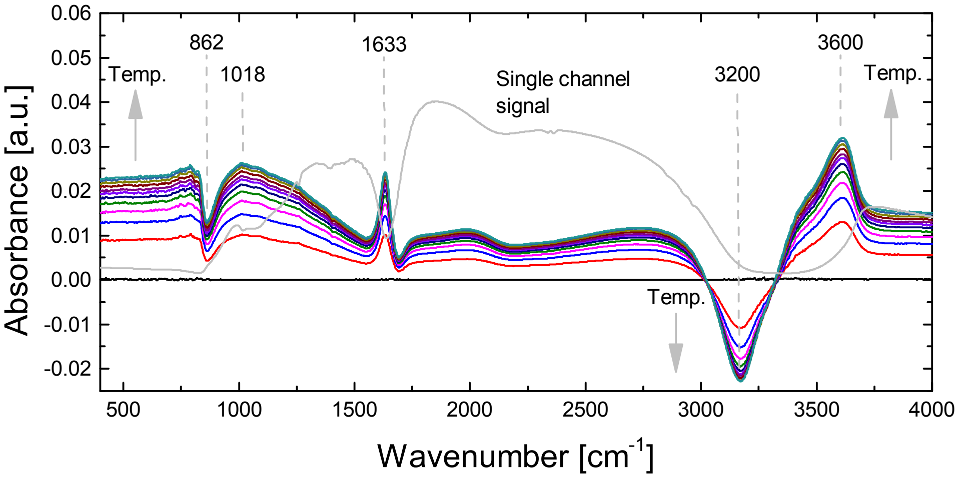

Figure 4.24: ATR IR spectra of H_2O temperature ramp. The arrows point in the direction of increased water temperature. Baseline spectra is taken after 3 min of water flow at room temperature. Subsequently the water temperatur is set to 50 °C and spectra are taken every 3 min. The spectra are kindly provided by Ahmed Bouhekka [80]. In gray and without scale the total IR intensity with water on TiO_2 in ATR setup is shown (single channel signal).

4.4.3 In-situ CO_2 adsorption on dye sensitized TiO_2

Building upon the carbonates and irradiation effects on pure TiO_2 samples of in-situ dye adsorption were used to investigate the additional adsorption of CO_2. Therefore the exact same experiment parameters as for the pure TiO_2 are applied to the dye sensitized TiO_2. The solvent from the in-situ dye adsorption experiment is pushed out by nitrogen gas till the sample is dry. Figure 4.25 shows purging water for 20 min followed by 20 min CO_2 saturated water (T = 0 min) and again purging water (T= 20 min) for 20 min. All solvents are temperature controlled at 35 °C. Every 60 s 400 scans are accumulated.

The background spectra is set at T = -20 min. During the first 20 min of water purging the bulk water bands at 1635 cm^{-1} and 3600 cm^{-1}rise steadily as seen with pure TiO_2 as well. During the whole experiment a negative band at 1075 cm^{-1}shows a desorption of organic solvent from the dye sensitization. At T = 0 min the CO_2 saturated water reaches the flow through cell. Again a quick rise of the sharp peak of dissolved CO_2 at 2342 cm^{-1} and broad carbonate bands at 1690 cm^{-1} and 1320 cm^{-1} rise. The intensities of the carbonate bands (integrated peak area) are lower compared to the pure TiO_2 adsorption experiment from Section 4.4.2 and differ in relative intensity. The preadsorbed dye influences the possible adsorption sites for the carbonates. The intesity of the carbonate bands shift towards the monodentate configuration into the broad shoulder at 1480 cm^{-1}. This trend is observed for all dye sensitized TiO_2 samples and a summary of carbonate integrated peak areas are presented in Table: 4.6. This is a qualitative trend which has uncertainties e.g. from the preparation method (amount of spin coated material) and could be quatitatively determined by ex-situ measurements. During the second water purging phase the band of dissolved CO_2 returns to zero whereas the carbonate band at 1590 cm^{-1} is very stable. The band at 1320 cm^{-1} diminishes but reaches a constant value roughly half of the maximum value. Very interesting is the fact that there are no negative dye bands, weather H_2O or CO_2 saturated water is introduced. This leads to the conclusion that the carbonates can not displace the bound dye molecules.

After the carbonate adsorption and 20 min of pure water purging, the visible light irradiation under a constant water flow is started. Figure 4.26 shows the in-situ ATR IR spectra during 20 min visible light irradiation followed by 10 min without irradiation. During the irradiation a broad band with a maximum at 980 cm^{-1} with decreasing tail up to 1700 cm^{-1} and water bands at 1635 cm^{-1} and 3600 cm^{-1} rise slowly, whereas a negative band at 3200 cm^{-1}appears. This trend partially reverses when the visible light irradiation is turned off. The temperature of the flow through cell rises by 4 °C during irradiation. The features are similar to the experiment without dye (Figure 4.23), only the maximum of the broad absorption is at a lower wavenumber (980 cm^{-1} compared to 1025 cm^{-1}without dye). The carbonate bands are very stable and do not decrease upon visible light irradiation. Also no negative dye bands are seen upon irradiation.

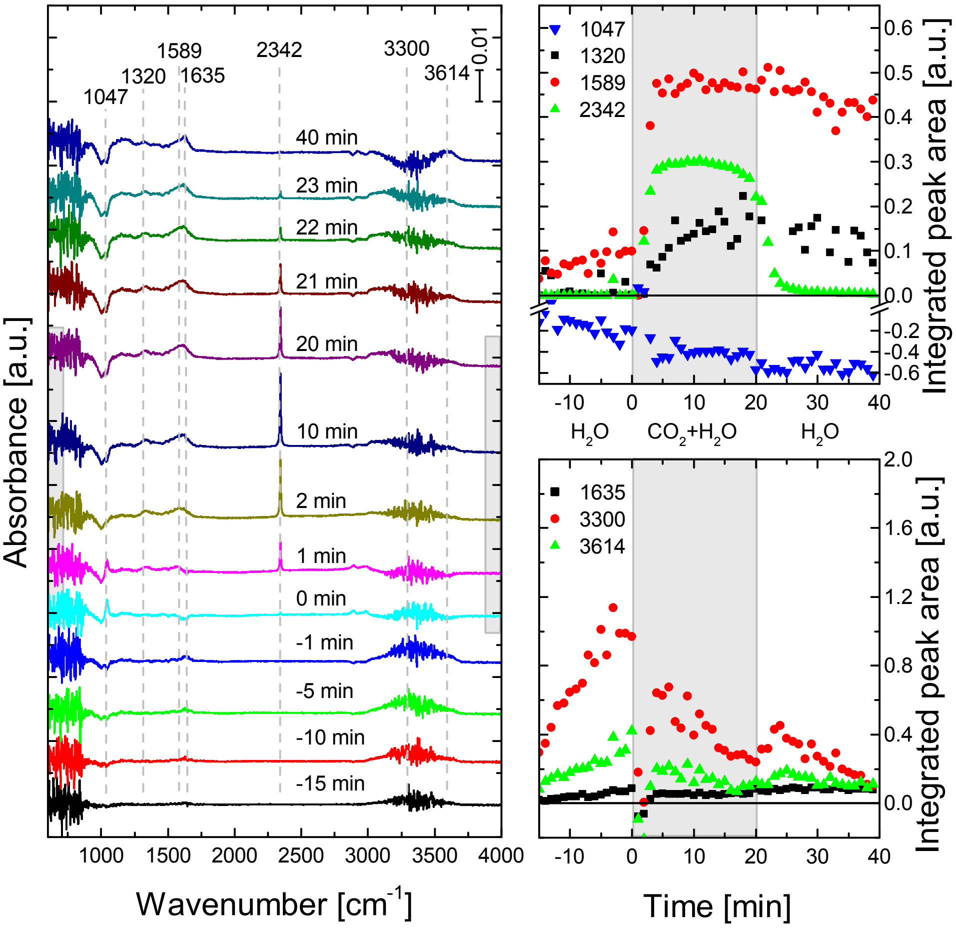

Figure 4.25: ATR IR spectra of CO_2 adsorbed on $TiO_2$with SF15 dye from saturated aqueous solution for 20 min. Purging with H_2O before and after the adsorption process. Highlighted in gray is the exposure to CO_2saturated water.

Table 4.6: Integrated peak areas of carbonate bands during CO_2 adsorption on TiO_2 P25 and dyes sensitized TiO_2 P25

Sample	Integrated peak area [a.u.]	
	1320 cm-1	1580 cm-1
TiO_2 P25	0.61	0.68
TiO_2 P25 SF1	0.11	0.23
TiO_2 P25 SF2	0.38	0.59
TiO_2 P25 SF15	0.18	0.24

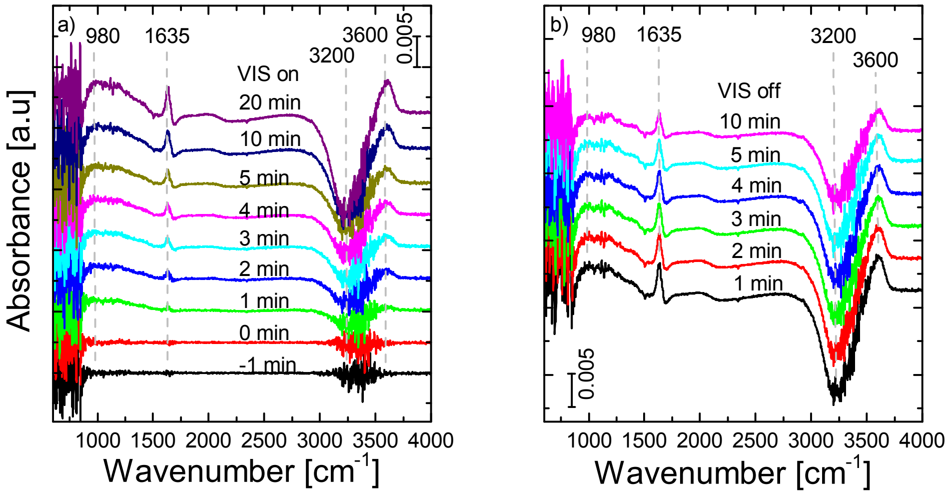

Figure 4.26: ATR IR spectra of visible light irradiation of CO_2 adsorbed from aqueous solution on TiO_2 P25 with SF15 dye. The residual carbonate spectra from Figure 4.25 is used as background spectra.

It is clearly shown that the irradiation of dye sensitized TiO_2 does not promote a further reaction of the carbonate bands but the stability of the dyes under reaction conditions is given.

4.4.4 In-situ CO_2 adsorption on dye sensitized TiO_2 with metal co-catalyst

To increase the amount of catalyst and carbonates on the internal reflection element a 2-5 µm thick film was used. The suspension is prepared as shown in Section 4.2 by mixing and washing. 500 µL of the suspension is put on the IRE and dried at 80°C for 1 h. This is a fast and convenient way of sample preparation but results in a porous structure where diffusion effects of the solvents and reactants can not be neglected.

Figure 4.27 shows the CO_2 sorption from aqueous solution on the catalyst. The cell is purged for 20 min with pure H_2O followed by 20 min of CO_2 saturated water (starting at $T = 0$ min) and purging with pure water for 20 min. The introduction of metal co-catalysts shows no impact on the carbonate coordination. Similar to the adsorption on TiO_2 P25 the dissolved CO_2 peak at 2343 cm^{-1} and two carbonate bands at 1320 cm^{-1} and 1590 cm^{-1}rise. Compared to the thin film adsorption experiments the dissolved CO_2 band rises slower due to the diffusion through the porous film. The rise of the carbonate bands is observed ahead of the dissolved CO_2. Only a very low CO_2 concentration is needed to cover the surface with carbonates.

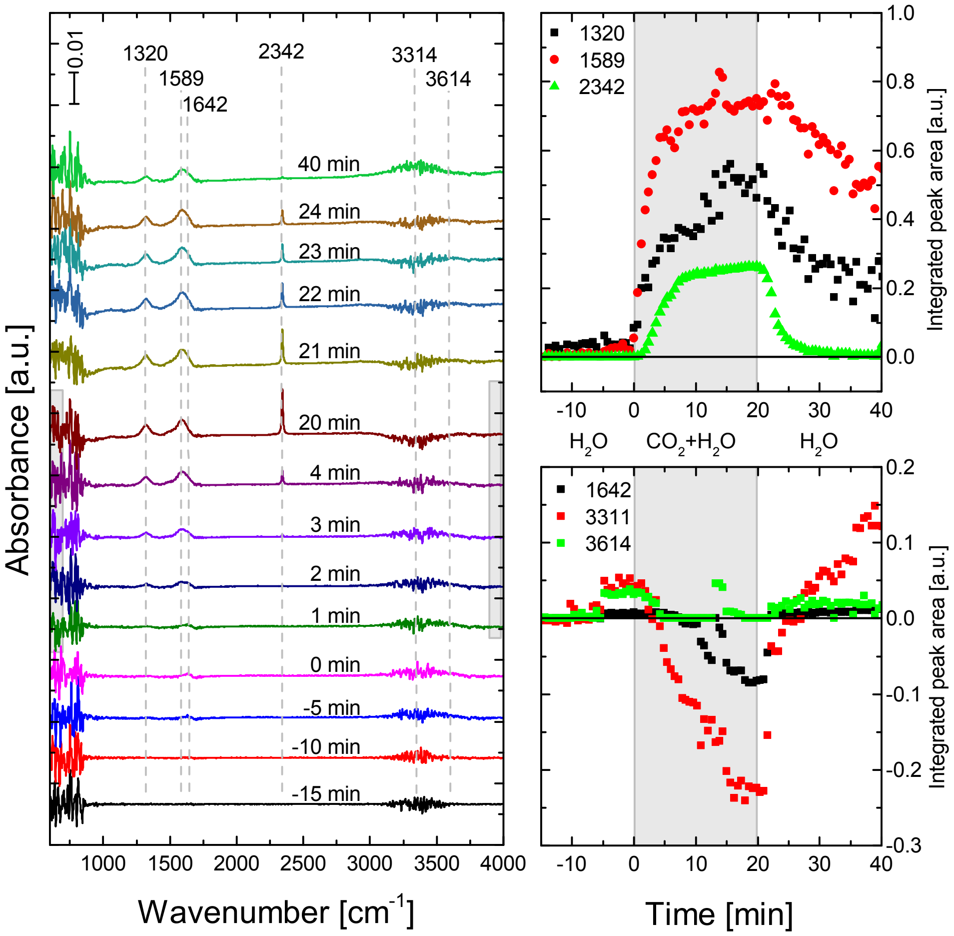

Figure 4.27: ATR IR spectra of CO_2 adsorbed on TiO_2 with 0.5 wt % Cu metal co-catalyst and dye from saturated aqueous solution for 20 min. Purging with H_2O before and after the adsorption process. Highlighted in gray is the exposure to CO_2saturated water.

For the irradiation experiment two changes are made. The outlet and inlet are connected to form a closed loop with a small reservoir. This is to enhance the amount of reactants and products on the catalyst surface and a longer surface contact time. Additionally samples from the loop can be taken and measured by gas chromatography. Figure 4.28 shows the in-situ ATR IR spectra and the temporal evolution of the integral of the most important bands. As background the previously CO_2 adsorbed sample from Figure 4.27 was used. The inlet and outlet are connected at $T = -3$ min, the irradiation with visible light during was done for 40 min and the sample was left for 20 min without irradiation. The band of dissolved CO_2 at 2342 cm^{-1} quickly decreases when connected to the closed loop and reservoir due to degassing into the reservoir. While the concentration of dissolved CO_2 decreases the sample is irradiated. This leads to a broad band with a maximum at 1047 cm^{-1} with a decreasing tail to 1630 cm^{-1}. To show the reversibility of this broad feature a new background was set at $T = 40$ min and shown are spectra after 55 min and 60 min. During the illumination the carbonate band at 1590 cm^{-1} diminishes to the initial intensity. The band at 1320 cm^{-1} is hidden in the broad band feature and can not be tracked further. The band at 1047 cm^{-1}does not decrease after the visible light irradiation is turned off. Further experiments with a temperature correction measurement could help to analyse this band in more detail.

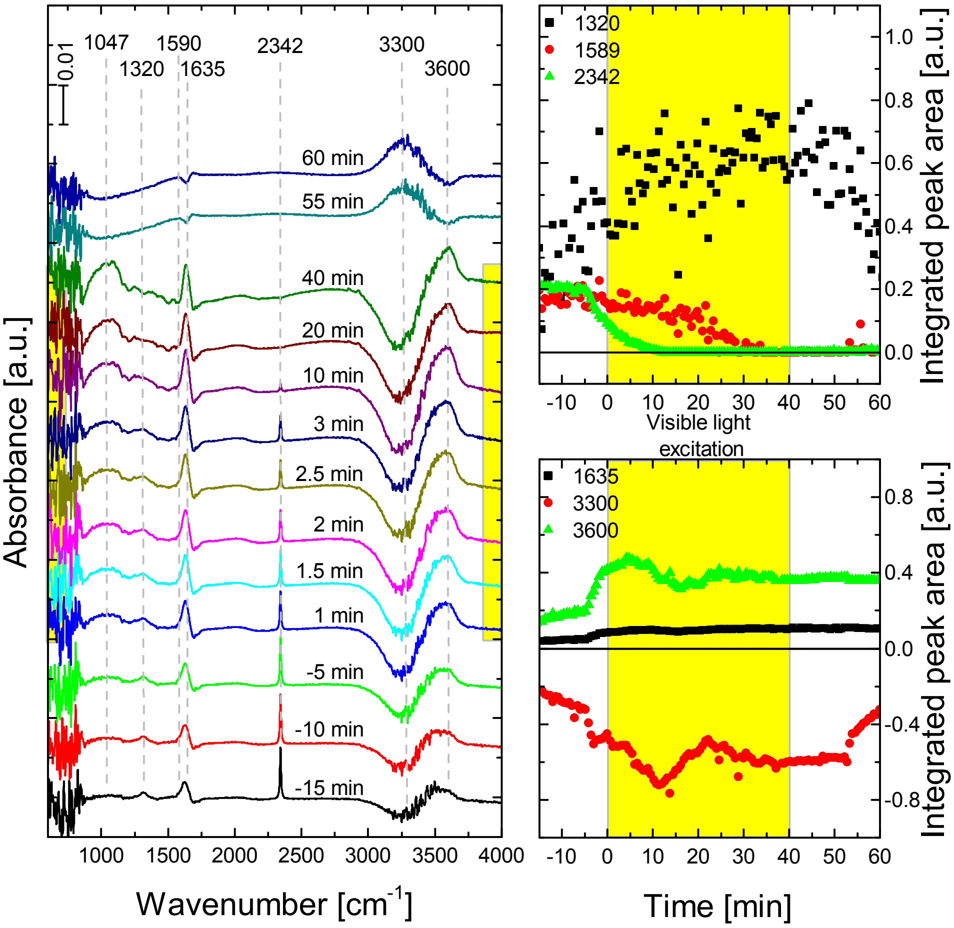

Figure 4.28: ATR IR spectra of visible light irradiation of CO_2 adsorbed from aqueous solution on TiO_2 P25 with 0.5 wt % Cu metal co-catalyst and dye. As background the previously CO_2 adsorbed sample from Figure 4.27 was used.

4.5 Gas chromatography

At first the chromatograph has to be calibrated for the expected intermediates and products. Two test gases (CO, CO_2, CH_4; and H_2 in inert gas) and a serial dilution for the hydrocarbons (aldehyde, formate, methanol in H_2O Figure 4.30) are used for the calibration. The standard sample volume is set to 500µL for gases and 1 mL for liquids. The chromatograph singnal is proportional to the quantity of the analyte but with the defined standard injection volume the concentration of the analyte is calculated. Figure 4.29 shows a quality check with the testgas for CO, CO_2, CH_4 (1000 ppm ± 23 ppm each). The peak areas are integrated and evaluated by the previously created calibration curve. The result shows 950 ppm for each analyte which is close to the real testgas concentration. If the deviation is constantly more then 10 % septum and syringes have to be checked for leakage and clogging. Sideport needles showed an significant improvement upon clogging issues.

The analysis of liquids and gases before and after irradiation of catalysts is performed with gas chromatography. One method is a combination with the in-situ irradiation ATR IR spectroscopy. CO_2 is pumped from the reservoir over the catalyst surface and samples are taken *"on the fly"*. Ususally a closed loop is arranged where the reactants are pumped multiple times over the catalyst surface to maximize the probability for the reduction. As already shown with in-situ ATR IR spectroscopy no surface reactions occur which is confirmed by gas chromatoraphy. Since the amount of catalyst is very small, another probing method is used.

The method is the mixture of *catalyst suspension* and reactants in an airtight vial with septum. Samples from the gasphase are taken in repeated intervals before and during irradiation, but similarly no hydrocarbons are detected. Several further experiments are performed. The addition of a sacrificial electron donor for faster dye regeneration, irradiation with a more powerful 1000 W Xenon lamp and irradiation of TiO_2 with metal cocatalyst with UV irradiation is extensively tested and an exerpt is shown in Table 4.7.

The collaboration partner for turnover measurments SCHMIDT-MENDE group performed further suspension type GC experiments. They worked with ethanol for the resuspension of agglomerated particles and used a ethanol water ratio of 1:1 for the irradiation experiments. They could detect an oxidized form of ethanol (acetaldehyde), which was difficult to separate from methanol retention time.

This leads to the conclusion that the indipendent research on the photosystem and the catalyst should be carried on. If a suitable catalyst material is found these two functions should be reunited. The best way for the catalyst research is the electrochemistry which was not sucessfully implemented in this project.

The chromatography provides a fast detection of analytes down to the ppm range. However the extension to a GC with mass spectroscopy is desired for isotope labeld experiments and for the analysis of unexpected intermediates.

Table 4.7: Excerpt of the investigated catalysts by gas chromatography. All samples are set up with with CO_2 saturated water if not otherwise stated.

Sample	**Irradiation & Results**	
TiO_2 Pt SF5	18 h in ATR flow through cell 75W VIS	decrease in CO_2, no HC
TiO_2 Pt SF16 + KI	18 h in ATR flow through cell 75W VIS	decrease in CO_2, no HC
TiO_2 P25 SF2 + KI	18 h in ATR flow through cell 75W VIS	no HC
TiO_2 P25 SF2 + sodium citrate	12 h ATR flow through cell 75W VIS	no HC
TiO_2 Pd, TiO_2 Pd SF2, TiO_2 Pd SF5; 50 mg in 3 ml susp. + KI	18 h in stirred vial 75W	no HC
TiO_2 Cu SF16 + $FeCl_2$50 mg in 10 mL; 150 mg $NaCO_{13}$	1000W 3 d stirred vial, tested at BASF GC-MS	no HC, traces of dye preparation solvent

Legend: HC, hydrocarbons

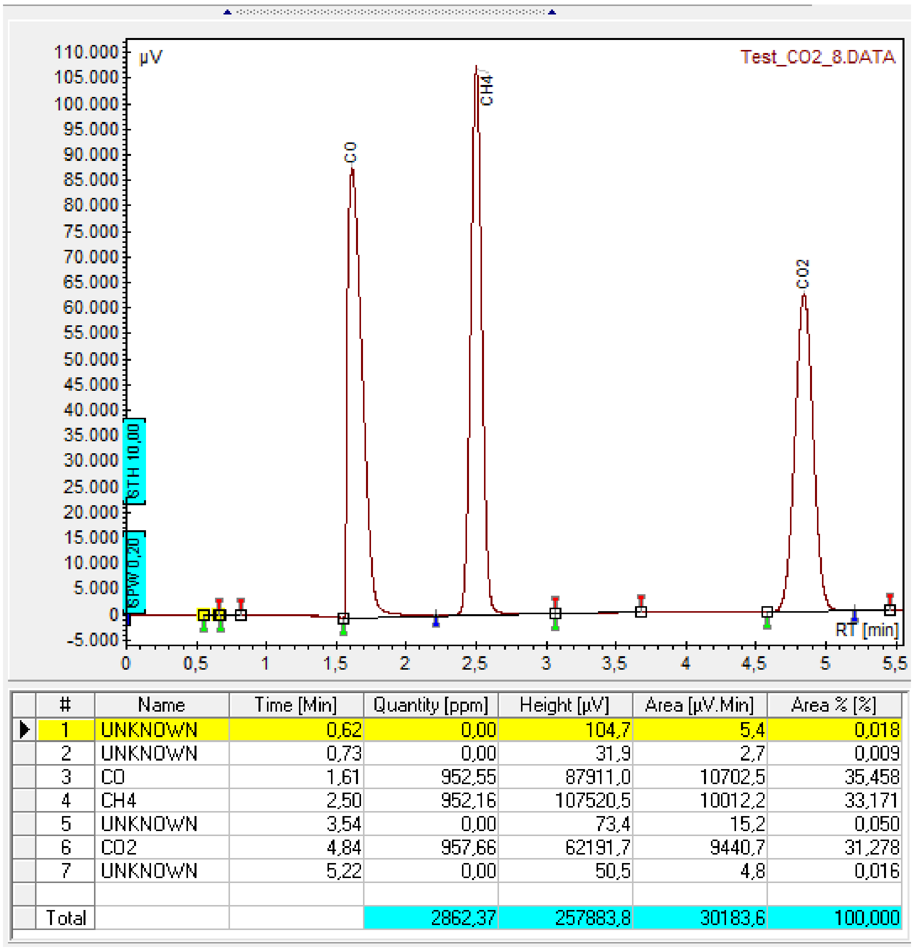

#	Name	Time [Min]	Quantity [ppm]	Height [µV]	Area [µV.Min]	Area % [%]
1	UNKNOWN	0,62	0,00	104,7	5,4	0,018
2	UNKNOWN	0,73	0,00	31,9	2,7	0,009
3	CO	1,61	952,55	87911,0	10702,5	35,458
4	CH4	2,50	952,16	107520,5	10012,2	33,171
5	UNKNOWN	3,54	0,00	73,4	15,2	0,050
6	CO2	4,84	957,66	62191,7	9440,7	31,278
7	UNKNOWN	5,22	0,00	50,5	4,8	0,016
Total			2862,37	257883,8	30183,6	100,000

Figure 4.29: Quality check with the testgas CO, CO_2, CH_4, 1000 ppm each in Ar is repeated at regular intervals.

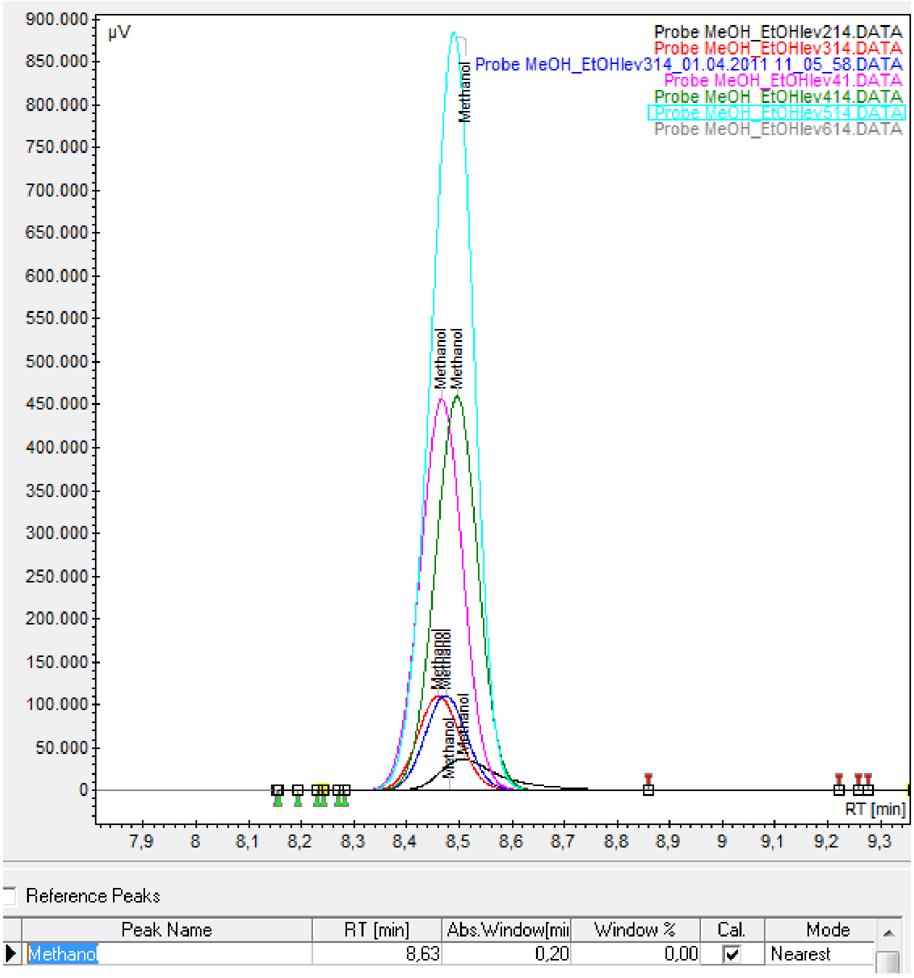

☐ Reference Peaks

	Peak Name	RT [min]	Abs.Window[mi	Window %	Cal.	Mode
▶	Methanol	8,63	0,20	0,00	☑	Nearest

Figure 4.30: Dilution series of methanol for the calibration curve. From top to bottom 10 000 ppm in H_2O diluted by a factor of 10. The retention time maximum varies in th range of 8.4 s - 8.65 s which is due manual handling of the injection.

5 Summary

Mechanistic studies of a new type of dye sensitized TiO_2 photocatalyst was investigated by IR spectroscopy, photometry and gas chromatography. A routine for nanoporous thin films with a medium thickness of 350 nm is developed to study the coordination and adsorption kinetics of organic dyes with three different anchoring groups. The thin films are very stable and minimize diffusion effects of adsorbent through the film. The dye binding configuration on TiO_2 is correlated with visible light absorption, total amount of dye adsorbed and generated photocurrents under visible light irradiation.

The stability of the organic dyes on the TiO_2 in real reaction conditions and the coordination of CO_2 from aqueous solution on the photocatalyst is measured with a new ATR IR flow through cell with a window for in-situ irradiation measurements.

5.1 Dye adsorption

The investigation of the binding mode of three anchoring groups by in-situ ATR IR spectroscopy leads to the following conclusions: The dyes with carboxylic acid anchor binds via bidentate configuration. A bridging coordination is reported to be the morst stable coordination. The dyes with hydroxamic acid anchoring group bind also in bidentate configuration and with a reported calculated bridging coordination [10]. The anhydride anchoring group undergoes a chemical cleavage when attached to the surface and adsorbs in a bidentate coordination but with two carboxylate groups. The underlying IR measurements are correlated with SFG, and Raman spectroscopy measurements within the projects collaborations. Further methods show the consequences of the binding configuration. The anhydride anchoring dyes occupy more surface area ($3.8 \cdot 10^{-18}$ m^2per dye molecule) than carboxylic and hydroxamic anchoring groups ($1.9 \cdot 10^{-18}$ m^2per dye molecule) by a factor of two corresponding to the amount of carboxylates formed. This leads to a high stability of the bound dye and quick removal of excessive dye.

The photometry of dyes shows absorption bands in the visible range depending on their donor and acceptor structure. The perylene/diphenylamine absorb at 450 nm & 590 nm (blue), perylene/triphenylamine at 530 nm (purple) and the rhodanine/carbazole at 438 nm (yellow). The dyes with anhydride anchoring group change their colors upon adsorption or due to the change of the aromatic system. An average frequency shift of $\emptyset\Delta\lambda_{\text{anhydride}} = -80\,\text{nm}$, $\emptyset\Delta\lambda_{\text{hydroxamic}} = -30\,\text{nm}$ and

$\phi\Delta\lambda_{\mathrm{carboxylic}} = -20\,\mathrm{nm}$ is observed. The shift to lower wavenumbers attributed to a shortening of the effective conjugation length upon adsorption. The main adsorption bands corresponds to the electronic transitions from HOMO to the LUMO. Since the HOMO is mainly located on the diphenylamine, triphenylamine and carbazole donor and the LUMO mainly on the perylene, and rhodanine acceptor core excitation of this transition leads to an intramolecular charge transfer from the donor to the acceptor pushing the excited electron from the dyes towards the TiO_2.

The photocurrents show the highest electron transfer potential for carbazole/rhodanine dye with hydroxamic anchor followed by the perylene/triphenylamine dye with carboxylic anchor. Third highest photocurrent shows the perylene/diphenylamine with anhydride anchoring group. Having all anchoring groups and all donor and acceptor combinations in the top three none of the combinations can be expelled before the stability tests in real reaction conditions.

5.2 CO_2 co-adsorption

Organic dyes are prone to degradation due to UV light and oxidative species. Anchoring groups vary in stability under acidic conditions [9]. Therefore in-situ ATR IR measurements of CO_2 saturated water on TiO_2 and dye sensitized TiO_2 are important to separate degradation and desorption. Additionally the coordination of formed carbonates can be identified.

Generally no used dye instantly desorbs upon contact with water or CO_2 saturated water. The usual exposure during in-situ IR spectroscopy is 1 h-12 h but the band bending due to thermal shifts superimpose rapidly. Ex-situ experiments for longer exposure to water and CO_2 did not show a significant color change without irradiation (qualitatively observed).

The sorption experiments of CO_2 on various combination of TiO_2 metal co-catalyst and dyes always resulted in the same carbonate bands with different intensities. Most challenging is the prevention of degassing in the flow through cell which results in bubble formation on the surface and heavily distorted IR spectra. Since CO_2 has a lower solubility at higher water temperatures the solvents are temperated at 35 °C during the experiments.

The in-situ ATR IR spectra of CO_2 saturated water show the evolution of three prominent bands. The dissolved CO_2 at 2342 $\mathrm{cm^{-1}}$ and two carbonate bands at 1320 $\mathrm{cm^{-1}}$ and 1590 $\mathrm{cm^{-1}}$ with a shoulder at 1480 $\mathrm{cm^{-1}}$. The bands are assigned to bidentate carbonate (1320 $\mathrm{cm^{-1}}$ and 1590 $\mathrm{cm^{-1}}$) and monodentate carbonate (1480 $\mathrm{cm^{-1}}$). A trend can be seen when comparing pure TiO_2 carbonate intensity with dye sensitized TiO_2. As expected the amount of free adsorption sites is reduced bye the dye and therefore the carbonate band integral is diminished. The relative intensity of the carbonate bands shift towards the monodentate configuration.

The coordination of CO_2 on five TiO_2 samples with metal co-catalysts (intended as electron scavengers and dissociation sites for multi-electron reduction) shows no significant difference to pure TiO_2.

5.3 Irradiation experiments

Two types of irradiation experiments are set up to show surface processes (in-situ irradiation ATR IR experiments) and reactant to product measurements in vials with septum for gas chromatography measurements. A combination of the two detecting devices gives mechanistic, kinetic and quantitative results at the same time.

The influence of visible and UV light on the catalyst and adsorbed species is studied with in-situ ATR IR spectroscopy. The irradiation of pure TiO_2 with UV light in aqueous environment is known from literature [78] for a wide pH range and differs greatly from visible light irradiation of TiO_2 even with dye sensitization. The UV light lead to a population of shallow trapped states for electrons beneath the conduction band of the TiO_2 These electrons can be further excited into the conduction band by the IR probing beam. This broad absorption beginning at $880\,\text{cm}^{-1}$ with a decreasing tail towards $2000\,\text{cm}^{-1}$ with a dip at 1658 nm. This dip is attributed to hydodgenbonded water at the TiO_2 interface, and is indicating TiO_2 hydrophobicity. This process is also returning immediately to its initial state when the UV light is turned off.

The visible light irradiation of pure TiO_2 and dye sensitized TiO_2 with or without adsorbed carbonates shows two features. A broad band with maximum at $1000\,\text{cm}^{-1}$ with decreasing tail to $1650\,\text{cm}^{-1}$ and a OH- peak shift from 1642cm^{-1} to $1635\,\text{cm}^{-1}$ and $3300\,\text{cm}^{-1}$ to $3600\,\text{cm}^{-1}$. The fact that there is no difference with or without the dye sensitization shows that electrons injected from the dye to the TiO_2 do not populate shallow electron states. The occurring band deformations rather result from temperature changes on the photocatalyst interface. The visible light induces a flow through cell temperature rise about 4 °C compared to 0.5 °C for UV irradiation.

The adsorbed carbonates do not react upon visible irradiation on dye sensitized TiO_2 and do not take part in the reduction process. Gas chromatography is used to confirm the lack of intermediate products in the gas or liquid phase during the IR irradiation experiments and in seperate batch reactor experiments.

5.4 Prospects

The development of new photocatalysts for CO_2 reduction is strongly dependent on the insight of the reaction pathway. In-situ ATR IR spectroscopy is a viable tool for the tracing of surface reactions as shown on the dye and carbonate chemisorption in this work. The irradiation experiments of catalyst surfaces in aqueous solution with visible light has many challenges. To suppress the influence of temperature change a temperature controlled flow through cell would be desirable. For the turnover measurements gas chromatography with mass spectroscopy is necessary to separate products and contaminates by isotopic labeling of the invested reactants .

Further work addressing the dissociative adsorption of CO_2 on the co-catalysts is needed. However, the obtained results show a successful dye binding analysis, with high photocurrents and stability towards all used reactants.

List of Figures

List of Tables

Bibliography

[1] Naomi Oreskes. The scientific consensus on climate change. *Science*, 306(5702):1686–1686, 2004.

[2] Rajendra K Pachauri and Andy Reisinger. Climate change 2007: Synthesis report. contribution of working groups i, ii and iii to the fourth assessment report of the intergovernmental panel on climate change. *Intergovernmental Panel on Climate Change*, 1, 2007.

[3] Quirin Schiermeier. Renewable power: Germany's energy gamble. *Nature*, 496(7444):156–158, 2013.

[4] Somnath C Roy, Oomman K Varghese, Maggie Paulose, and Craig A Grimes. Toward solar fuels: photocatalytic conversion of carbon dioxide to hydrocarbons. *Acs Nano*, 4(3):1259–1278, 2010.

[5] A Fujishima and K Honda. Photolysis-decomposition of water at the surface of an irradiated semiconductor. *Nature*, 238(5385):37–38, 1972.

[6] Amy L Linsebigler, Guangquan Lu, and John T Yates Jr. Photocatalysis on tio2 surfaces: principles, mechanisms, and selected results. *Chemical Reviews*, 95(3):735–758, 1995.

[7] Tooru Inoue, Akira Fujishima, Satoshi Konishi, and Kenichi Honda. Photoelectrocatalytic reduction of carbon dioxide in aqueous suspensions of semiconductor powders. *Nature*, 277:637–638, 1979.

[8] O.K. Varghese, M. Paulose, T.J. LaTempa, and C.A. Grimes. High-rate solar photocatalytic conversion of CO2 and water vapor to hydrocarbon fuels. *Nano Lett*, 9(2):731–737, 2009.

[9] William R McNamara, Rebecca L Milot, Hee-eun Song, Robert C Snoeberger III, Victor S Batista, Charles A Schmuttenmaer, Gary W Brudvig, and Robert H Crabtree. Water-stable, hydroxamate anchors for functionalization of tio2 surfaces with ultrafast interfacial electron transfer. *Energy & Environmental Science*, 3(7):917–923, 2010.

[10] Jing Yang, Phil J Bremer, Iain L Lamont, and A James McQuillan. Infrared spectroscopic studies of siderophore-related hydroxamic acid ligands adsorbed on titanium dioxide. *Langmuir*, 22(24):10109–10117, 2006.

[11] O Ozcan, F Yukruk, EU Akkaya, and D Uner. Dye sensitized co2 reduction over pure and platinized tio2. *Topics in Catalysis*, 44(4):523–528, 2007.

[12] T. Nguyen, L.M. Peter, and H.X. Wang. Characterization of Electron Trapping in Dye-Sensitized Solar Cells by Near-IR Transmittance Measurements. *Journal of Physical Chemistry C*, 113(19):8532–8536, 2009.

[13] B O'Regan and M Grätzel. Low cost and highly efficient solar cells based on the sensitization of colloidal titanium dioxide. *Nature*, 335:7377, 1991.

[14] Anders Hagfeldt, Gerrit Boschloo, Licheng Sun, Lars Kloo, and Henrik Pettersson. Dye-sensitized solar cells. *Chemical Reviews*, 110(11):6595–6663, 2010.

[15] T.L. Thompson and J.T. Yates. TiO 2-based photocatalysis: surface defects, oxygen and charge transfer. *Topics in Catalysis*, 35(3):197–210, 2005.

[16] https://www.aerosil.com/product/aerosil/en/effects/photocatalyst/pages/default.aspx, 2012/05/10.

[17] Shipra Mital Gupta and Manoj Tripathi. A review of tio2 nanoparticles. *Chinese Science Bulletin*, 56(16):1639–1657, 2011.

[18] Ulrike Diebold. The surface science of titanium dioxide. *Surface science reports*, 48(5):53–229, 2003.

[19] Matthias Batzill. Fundamental aspects of surface engineering of transition metal oxide photocatalysts. *Energy & Environmental Science*, 4(9):3275–3286, 2011.

[20] Xiaobo Chen and Samuel S Mao. Titanium dioxide nanomaterials: synthesis, properties, modifications, and applications. *Chemical reviews*, 107(7):2891–2959, 2007.

[21] Paul Fenter and Neil C Sturchio. Mineral–water interfacial structures revealed by synchrotron x-ray scattering. *Progress in Surface Science*, 77(5):171–258, 2004.

[22] Koichi Momma and Fujio Izumi. Vesta: a three-dimensional visualization system for electronic and structural analysis. *Journal of Applied Crystallography*, 41(3):653–658, 2008.

[23] B Voelker, F Wölzl, T Burgi, and D Lingenfelser. Dye bonding to tio2: An in situ atr-ir study, simulations and correlation with dsc cell characteristics. *Langmuir: the ACS journal of surfaces and colloids*, 2012.

[24] Julian Burschka, Norman Pellet, Soo-Jin Moon, Robin Humphry-Baker, Peng Gao, Mohammad K Nazeeruddin, and Michael Grätzel. Sequential deposition as a route to high-performance perovskite-sensitized solar cells. *Nature*, 2013.

[25] Lukas Schmidt-Mende, Udo Bach, Robin Humphry-Baker, Tamotsu Horiuchi, Hidetoshi Miura, Seigo Ito, Satoshi Uchida, and Michael Grätzel. Organic dye for highly efficient solid-state dye-sensitized solar cells. *Advanced Materials*, 17(7):813–815, 2005.

[26] Shu Wang, Yuliang Li, Chimin Du, Zhiqiang Shi, Shengxiong Xiao, Daoben Zhu, Enqin Gao, and Shengmin Cai. Dye sensitization of nanocrystalline tio_2 by perylene derivatives. *Synthetic metals*, 128(3):299–304, 2002.

[27] Chen Li and Henrike Wonneberger. Perylene imides for organic photovoltaics: yesterday, today, and tomorrow. *Advanced Materials*, 24(5):613–636, 2012.

[28] Kaname Suto, Akinori Konno, Yoshimasa Kawata, Shigeru Tasaka, and Atsushi Sugita. Adsorption dynamics of the n719 dye on nanoporous titanium oxides studied by resonance raman scattering and fourier transform infrared spectroscopy. *Chemical Physics Letters*, 536:45–49, 2012.

[29] Shun Yu, Sareh Ahmadi, Marcelo Zuleta, Haining Tian, Karina Schulte, Annette Pietzsch, Franz Hennies, Jonas Weissenrieder, Xichuan Yang, and Mats Göthelid. Adsorption geometry, molecular interaction, and charge transfer of triphenylamine-based dye on rutile tio2 (110). *Journal of Chemical Physics*, 133(22):4704, 2010.

[30] Lars Ojamäe, Christian Aulin, Henrik Pedersen, and Per-Olov Käll. Ir and quantum-chemical studies of carboxylic acid and glycine adsorption on rutile tio$_2$ nanoparticles. *Journal of colloid and interface science*, 296(1):71–78, 2006.

[31] SP Bates, G Kresse, and MJ Gillan. The adsorption and dissociation of roh molecules on tio$_2$(110). *Surface science*, 409(2):336–349, 1998.

[32] Elena Galoppini. Linkers for anchoring sensitizers to semiconductor nanoparticles. *Coordination chemistry reviews*, 248(13):1283–1297, 2004.

[33] Anna Keese. Investigation of dye-functionalized tio2 nanoparticles using vibrational sum-frequency-generation spectroscopy. 2012.

[34] GB Deacon and RJ Phillips. Relationships between the carbon-oxygen stretching frequencies of carboxylato complexes and the type of carboxylate coordination. *Coordination Chemistry Reviews*, 33(3):227–250, 1980.

[35] Kee Eun Lee, Mario A Gomez, Samir Elouatik, and George P Demopoulos. Further understanding of the adsorption mechanism of n719 sensitizer on anatase tio2 films for dssc applications using vibrational spectroscopy and confocal raman imaging. *Langmuir*, 26(12):9575–9583, 2010.

[36] Barbara Völker. Spektroskopische charakterisierung von farbstoffsensibilisierten solarzellen spectroscopical characterisation of dye sensitized solar cells.

[37] Tomas Edvinsson, Chen Li, Neil Pschirer, Jan Schöneboom, Felix Eickemeyer, Rüdiger Sens, Gerrit Boschloo, Andreas Herrmann, Klaus Müllen, and Anders Hagfeldt. Intramolecular charge-transfer tuning of perylenes: spectroscopic features and performance in dye-sensitized solar cells. *The Journal of Physical Chemistry C*, 111(42):15137–15140, 2007.

[38] NT Do and M Baerns. Effect of support material on the adsorption structures of furan and maleic anhydride on the surface of v2o5/p2o5 catalysts. ii: Results of in situ infrared spectroscopic studies. *Applied catalysis*, 45(1):9–26, 1988.

[39] JN Wilson, DJ Titheridge, L Kieu, and H Idriss. Reactions of maleic anhydride over< equation>< font face='verdana'> tio$_2$(001) single crystal surfaces.

Journal of Vacuum Science & Technology A: Vacuum, Surfaces, and Films, 18(4):1887–1892, 2000.

[40] P Bossier, M Hofte, and W Verstraete. Ecological significance of siderophores in soil. *Advances in microbial ecology*, 10, 1988.

[41] John P Folkers, Christopher B Gorman, Paul E Laibinis, Stefan Buchholz, George M Whitesides, and Ralph G Nuzzo. Self-assembled monolayers of long-chain hydroxamic acids on the native oxide of metals. *Langmuir*, 11(3):813–824, 1995.

[42] Britt A Holmén, M Isabel Tejedor-Tejedor, and William H Casey. Hydroxamate complexes in solution and at the goethite-water interface: A cylindrical internal reflection fourier transform infrared spectroscopy study. *Langmuir*, 13(8):2197–2206, 1997.

[43] Timothy P Brewster, Steven J Konezny, Stafford W Sheehan, Lauren A Martini, Charles A Schmuttenmaer, Victor S Batista, and Robert H Crabtree. Hydroxamate anchors for improved photoconversion in dye-sensitized solar cells. *Inorganic chemistry*, 2013.

[44] Heike Glade. Transport und reaktion von kohlendioxid in entspannungsverdampfern zur meerwasserentsalzung. *Fortschritt Berichte-VDI Reihe III Verfahrenstechnik*, 2001.

[45] Norman Neill Greenwood, Alan Earnshaw, and Alan Earnshaw. *Chemistry of the Elements*, volume 1. Pergamon press Oxford etc., 1984.

[46] Jonas Baltrusaitis, Jennifer Schuttlefield, Elizabeth Zeitler, and Vicki H Grassian. Carbon dioxide adsorption on oxide nanoparticle surfaces. *Chemical Engineering Journal*, 170(2):471–481, 2011.

[47] L-F Liao, C-F Lien, D-L Shieh, M-T Chen, and J-L Lin. Ftir study of adsorption and photoassisted oxygen isotopic exchange of carbon monoxide, carbon dioxide, carbonate, and formate on tio2. *The Journal of Physical Chemistry B*, 106(43):11240–11245, 2002.

[48] DJC Yates. Infrared studies of the surface hydroxyl groups on titanium dioxide, and of the chemisorption of carbon monoxide and carbon dioxide. *The Journal of Physical Chemistry*, 65(5):746–753, 1961.

[49] I. Dolamic and T. Burgi. Photoassisted decomposition of malonic acid on TiO2 studied by in situ attenuated total reflection infrared spectroscopy. *J. Phys. Chem. B*, 110(30):14898–14904, 2006.

[50] Etsuko Fujita. Photochemical carbon dioxide reduction with metal complexes. *Coordination chemistry reviews*, 185:373–384, 1999.

[51] Wolfgang Demtröder. *Atome, Moleküle und Festkörper*, volume 3. Springer DE, 2005.

[52] NJ Harrick. Surface chemistry from spectral analysis of totally internally reflected radiation*. *The Journal of Physical Chemistry*, 64(9):1110–1114, 1960.

[53] J Rs DeVore. Refractive indices of rutile and sphalerite. *JOSA*, 41(6):416–417, 1951.

[54] Olympusmicro. http://www.olympusmicro.com/primer/java/tirf/evaintensity/, November 2013.

[55] Beata Zielińska, Joanna Grzechulska, Barbara Grzmil, and Antoni W Morawski. Photocatalytic degradation of reactive black 5: A comparison between tio2-tytanpol a11 and tio2-degussa p25 photocatalysts. *Applied Catalysis B: Environmental*, 35(1):L1–L7, 2001.

[56] Email communitction with Alexandra Seeber, BASF SE, 2009/05/11.

[57] Email communitction with Liu Young, BASF SE, 2012/02/10.

[58] http://www.millipore.com/lab_water/clw4/type1, 2012/05/10.

[59] Michael Bass. *Handbook of optics*. McGraw-Hill, 1995.

[60] http://www.dyesol.com/page/Products, 2012/05/10.

[61] M Bradley. Curve fitting in raman and ir spectroscopy: basic theory of line shapes and applications. *Thermo Fisher Scientific, Madison, USA, Application Note*, 50733, 2007.

[62] John P Tobin, W Hirschwald, and J Cunningham. Xps and xaes studies of transient enhancement of cu< sup> 1</sup> at cuo surfaces during vacuum outgassing. *Applications of surface science*, 16(3):441–452, 1983.

[63] C Robert III et al. Hydroxamate anchors for water-stable attachment to tio2 nanoparticles. *Energy & Environmental Science*, 2(11):1173–1175, 2009.

[64] Heinz GO Becker. ua: Organikum, organisch-chemisches grundpraktikum, 22. auflage, 2004.

[65] Juan Pei, Shengjie Peng, Jifu Shi, Yanliang Liang, Zhanliang Tao, Jing Liang, and Jun Chen. Triphenylamine-based organic dye containing the diphenylvinyl and rhodanine-3-acetic acid moieties for efficient dye-sensitized solar cells. *Journal of Power Sources*, 187(2):620–626, 2009.

[66] Philippe Bühlmann, C Affolter, and Martin Badertscher. *Spektroskopische Daten zur Strukturaufklärung organischer Verbindungen*. Springer DE, 2001.

[67] Eric Johnson and Ricardo Aroca. Spectroscopic properties and packing of langmuir-blodgett monolayers of perylenetetracarboxylic anhydrides. *Langmuir*, 11(5):1693–1700, 1995.

[68] Andrzej Łapiński, Andrzej Graja, Iwona Olejniczak, Andrzej Bogucki, Maria Połomska, Jérôme Baffreau, Lara Perrin, Stéphanie Leroy-Lhez, and Piétrick Hudhomme. Vibrational and electronic properties of perylenediimide linked

to fullerene and tetrathiafulvalene. *Molecular Crystals and Liquid Crystals*, 447(1):87–405, 2006.

[69] S Rodriguez-Llorente, R Aroca, and J Duff. Vibrational spectra and thin solid films of a bi (propylperylenediimide). *J. Mater. Chem.*, 8(10):2175–2179, 1998.

[70] M Friedrich, G Gavrila, C Himcinschi, TU Kampen, A Yu Kobitski, H Mendez, G Salvan, I Cerrillo, J Mendez, N Nicoara, et al. Optical properties and molecular orientation in organic thin films. *Journal of Physics: Condensed Matter*, 15(38):S2699, 2003.

[71] John Coates. Interpretation of infrared spectra, a practical approach. *Encyclopedia of analytical chemistry*, 2000.

[72] Kim S Finnie, John R Bartlett, and James L Woolfrey. Vibrational spectroscopic study of the coordination of (2, 2'-bipyridyl-4, 4'-dicarboxylic acid) ruthenium (ii) complexes to the surface of nanocrystalline titania. *Langmuir*, 14(10):2744–2749, 1998.

[73] A Vittadini, A Selloni, FP Rotzinger, and M Grätzel. Formic acid adsorption on dry and hydrated tio2 anatase (101) surfaces by dft calculations. *The Journal of Physical Chemistry B*, 104(6):1300–1306, 2000.

[74] Jean-Joseph Max and Camille Chapados. Isotope effects in liquid water by infrared spectroscopy. iii. ho and do spectra from 6000 to 0 cm. *The Journal of chemical physics*, 131:184505, 2009.

[75] Llewellyn H Jones and Eugene McLaren. Infrared absorption spectra of so2 and co2 in aqueous solution. *The Journal of Chemical Physics*, 28(5):995–995, 1958.

[76] Buergi T Kriesche, T. Electronic structure of irradiated Tio2. 2014.

[77] Akira Yamakata, Taka aki Ishibashi, and Hiroshi Onishi. Time-resolved infrared absorption spectroscopy of photogenerated electrons in platinized tio2 particles. *Chemical Physics Letters*, 333(3–4):271–277, 2001.

[78] David M Savory, David S Warren, and A James McQuillan. Shallow electron trap, interfacial water, and outer-sphere adsorbed oxalate ir absorptions correlate during uv irradiation of photocatalytic tio2 films in aqueous solution. *The Journal of Physical Chemistry C*, 115(4):902–907, 2010.

[79] George C Pimentel and Aubrey Lester McClellan. The hydrogen bond. 1960.

[80] A Bouhekka. Adsorption of bsa protein on silicon, germanium and titanium dioxide investigated by in situ atr spectroscopy.

Danksagung

Ich möchte mich bei meinem Doktorvater Thomas Bürgi bedanken, für die Möglichkeiten und Freiräume die er bereitgestellt hat, die diese Arbeit einzigartig macht. Deine angenehme, ruhige Art hat mich immer motiviert neue Fragen zu stellen.

Frau Annemarie Pucci und ihren Mitarbeitern möchte ich danken für die Diskussionen, die aus den Vorträgen in ihrem Arbeitskreis entstanden sind. Die konstruktive Kritik und Verbesserungen gingen in diese Arbeit mit ein.

Ich möchte mich von ganzem Herzen bei meinen Eltern und meiner Schwester bedanken, die immer an meinen Weg glauben und mich liebevoll unterstützt haben.

Meiner Freundin Lissa möchte ich für den Halt bedanken den sie mir gegeben hat. Dein Arbeitseinsatz und Willenskraft ist immer mein Vorbild. Du hast mein Leben mit Liebe erfüllt!

Meinen Arbeitskollegen und Freunden Thomas und Nikolaus möchte ich danken für die Hilfe im Labor und wissenschaftlichen Diskussionen, die häufig Ausgangspunkt für lange Abende waren. Mit viel Erfahrung und Begeisterungsfähigkeit war jeder Tag spannend.

Den Freunden aus dem PCI und KIP Maria H., Maria A., Stella, Isabel, Anna, Diana, Piluca, Steffen, Jörg, Abdel, Daniel R. und Marius für die tolle Zeit, den wahnsinnig schönen Erfahrungen und Feiern. Mit Euch befreundet zu sein ist für mich etwas ganz Besonderes.

Vielen Dank an die Arbeitsgruppe in Genf, insbesondere Alastair, Stefan, Igor und Ahmed. Es war eine tolle Zeit hier in Heidelberg und ich freue mich euch auf der ganzen Welt besuchen kommen zu können!

Meinen Projektpartnern Anna, Florian und Michael aus dem PCI danke ich für die vielen Informationen die wir zusammengetragen haben und diese Arbeit komplett gemacht haben. Der wissenschaftliche Austausch war sehr produktiv und hat immer Spaß gemacht.

Zuletzt möchte ich mich bei der Feinmechanischen Werkstatt im PCI, allen voran Klaus Schmitt für die Umsetzung aller Ideen in technisch bester Ausführung und dem gesamten angestellten Personal bedanken.